

# Compensation of Time Delays Caused by Digital Control

## Implementation of Predictive Control

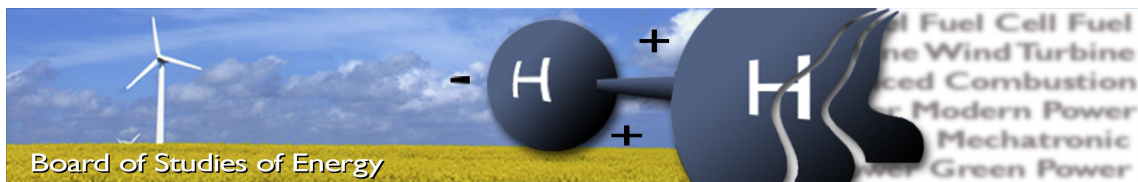


AALBORG UNIVERSITY

STUDENT REPORT

2<sup>nd</sup> Semester  
Power Electronics and Drives  
29<sup>th</sup> of May 2017





**Title:** Compensation of Time Delays Caused by Digital Control  
**Subtitle:** Implementation of Predictive Control  
**Semester:** 2<sup>nd</sup> semester Power Electronics and Drives  
**Semester theme:** Control of Converter-Fed AC Drives  
**Project period:** 03.02.2017 - 29.05.2017  
**Supervisor:** Dong Wang  
**Co-supervisor:** Kaiyuan Lu  
**Project group:** PED2-851  
**ECTS:** 15

---

Charlie Sørensen

---

Mads Kjeldal Graungaard

---

Copies: -  
 Pages of project: 68  
 Pages of appendices: 29  
 Total PDF count: 114

#### ABSTRACT:

Field oriented control is the main control strategy used in the industry, but it suffers from being destabilised due to time delays introduced by digital control. This system destabilisation is especially pronounced for high-speed drives or low switching frequency applications. This project addresses how time delay caused by digital control affects conventional field oriented control and will investigate different control strategies to compensate this. A laboratory setup including a drive machine, load machine and inverter, controlled by dSPACE, will be build. A model of the system together with a thorough description of PI-parameter tuning will be given, and field oriented control will be experimentally tested and compared to simulation results. This will also include the destabilising effects on field oriented control caused by digital control. A Smith predictor using a model based predictor will be described and its ability to compensate time delays will be shown both in simulation and in the laboratory. Different approaches to eliminate the need for machine parameters will be developed and their performance tested. The analysis and work done in this project will show that using a Smith predictor, the stability and bandwidth of the converter-fed AC drive can be significantly increased compared to conventional field oriented control.

By signing this document, each member of the group confirms that all group members have participated in the project work, and thereby all members are collectively liable for the contents of the report. Furthermore, all group members confirm that the report does not include plagiarism.



# Preface

---

The following project is the work of a 2<sup>nd</sup> semester group on the master program of Power Electronics and Drives at the Department of Energy Technology, Aalborg University. It is written by two students in the spring semester of 2017. The semester theme is *Control of Converter-fed AC Drives*. This has lead the authors to focus their work on time delay compensation in the field of synchronous machine control.

The prerequisites for reading this project is a basic understanding of synchronous machines, along with the basics of engineering mathematics, electrical engineering and classical control theory. As for the content, the authors have made an effort to make it easy for the readers to familiarise themselves with the structure. This is done through leitmotifs in the form of short introductions and conclusions that will clarify what is examined in the forthcoming chapter and highlight the key points.

In the beginning of the project, a list of acronyms and a nomenclature list including symbols, descriptions and units are included. Throughout the project, citations are given with the IEEE transactions style. This means, that a citation will appear in square brackets and a number will refer the reader to the correct citation in the bibliography found as a last chapter in the project. Cross references to figures and tables are numbered after chapters, e.g. figure 1.1, for the first figure in chapter one. Equations are numbered after section in a similar manner.

The appendices are found as an ending to the project. They are included as a supplement to give the interested reader an insight into the physical setup, machine parameter determination, and details about derivations. Furthermore gains of all PI-controllers used are included in the appendix.

This project has been highly dependent on several software packages for different applications. The most important are mentioned hereafter. MATLAB for numerical calculations and MATLAB Simulink is used to make simulation models used to simulate relevant responses and system behaviour. Maple is used for analytical derivations and calculations.

The authors would like to extend thanks to some of the people who have aided in the process of this project. Assistant Professor Dong Wang and Associate Professor Kaiyuan Lu have been the supervisor and co-supervisor on this student project and they have been an excellent inspiration for the prospects of the work. Furthermore, they have aided in the understanding of the basic concepts, which has been greatly sped up the process, and provided selected and relevant literature to support the project. Associate Professor Tamas Kerekes has been a great help in the process of debugging the laboratory setup and has helped the project group gather necessary components.



# Acronyms

---

<b>μC</b>	Microcontroller
<b>ADC</b>	Analog to Digital Converter
<b>DAC</b>	Digital to Analog Converter
<b>DO</b>	Disturbance Observer
<b>DSP</b>	Digital Signal Processor
<b>DTC</b>	Direct Torque Control
<b>FOC</b>	Field Oriented Control
<b>LHP</b>	Left Half Plane
<b>LP</b>	Linear Predictor
<b>LPF</b>	Low Pass Filter
<b>MBP</b>	Model Based Predictor
<b>MLP</b>	Modified Linear Predictor
<b>MPC</b>	Model Predictive Control
<b>MSP</b>	Modified Smith Predictor
<b>OP</b>	Ohm's Predictor
<b>PI</b>	Proportional Integral
<b>PM</b>	Permanent Magnet
<b>PMSM</b>	Permanent Magnet Synchronous Machine
<b>PWM</b>	Pulse Width Modulation
<b>SP</b>	Smith Predictor
<b>SPMSM</b>	Surface Mounted PMSM
<b>SPWM</b>	Sinusoidal Pulse Width Modulation
<b>SVM</b>	Space Vector Modulation
<b>THD</b>	Total Harmonic Distortion
<b>VSI</b>	Voltage Source Inverter
<b>ZOH</b>	Zero Order Hold



# Nomenclature

---

Sign	Description	Unit
$\lambda_{mpm}$	Maximum PM flux linkage	[Wb.t]
$\omega_e$	Electrical angular velocity	[rad/s]
$\omega_m$	Mechanical angular velocity	[rad/s]
$\theta_e$	Electrical angle	[rad]
$f_{sw}$	Switching frequency	[Hz]
$f_s$	Sampling frequency	[Hz]
$k_T$	Torque constant	[Nm/A]
$m_f$	Frequency-modulation ratio	[–]
$n_n$	Rated speed	[RPM]
$p$	Number of pole pairs	[–]
$B_m$	Viscous damping	[N · s/rad]
$I_n$	Rated current	[A]
$J_0$	Coulomb friction	[Nm]
$J$	Moment of inertia	[kg · m <sup>2</sup> ]
$L_d$	Direct axis inductance	[H]
$L_q$	Quadrature axis inductance	[H]
$P_n$	Rated power	[W]
$R_s$	Stator phase resistance	[Ω]
$T_n$	Rated torque	[Nm]
$T_s$	Sampling period	[s]
$T_{sw}$	Switching period	[s]



# Contents

---

<b>1</b>	<b>Introduction to Time Delay</b>	<b>1</b>
1.1	Present Strategies for Time Delay Compensation . . . . .	2
1.2	Formulation of the Problem . . . . .	3
1.3	Project Outline . . . . .	4
<b>2</b>	<b>Description of the Laboratory Setup</b>	<b>5</b>
2.1	Permanent Magnet Synchronous Machine (PMSM) . . . . .	7
<b>3</b>	<b>Field Oriented Control of a PMSM</b>	<b>11</b>
3.1	Controller Design Without Time Delay . . . . .	13
3.2	Controller Design Including Time Delay . . . . .	16
3.2.1	Continuous Time Controllers . . . . .	20
3.2.2	Discrete Time Controllers . . . . .	24
3.3	Stability Analysis . . . . .	26
3.4	Simulation of FOC . . . . .	29
3.5	Laboratory Experiment of FOC . . . . .	32
3.6	Discussion of Controllers . . . . .	35
<b>4</b>	<b>Time Delay Compensation</b>	<b>37</b>
4.1	The Smith Predictor . . . . .	37
4.2	Implementation and Simulation of Smith Predictor . . . . .	39
4.3	Experimental Results of Smith Predictor . . . . .	42
4.4	Parameter Sensitivity Analysis of the Smith Predictor . . . . .	51
4.5	Parameter Independent Predictors . . . . .	54
4.5.1	Model Based Predictor with Estimated Inductance . . . . .	54
4.5.2	Linear Predictor . . . . .	57
4.5.3	Investigation of Model Linearity . . . . .	59
<b>5</b>	<b>Conclusion</b>	<b>65</b>
5.1	Future Work . . . . .	67

## Appendix

<b>A</b>	<b>Laboratory Setup</b>	<b>71</b>
A.1	Voltage Source Inverter . . . . .	71
A.1.1	Modulation Scheme . . . . .	74
A.2	dSPACE . . . . .	78
<b>B</b>	<b>System Parameter Identification</b>	<b>83</b>
B.1	Permanent Magnet Flux Linkage . . . . .	83
B.2	Mechanical Parameters . . . . .	84
B.3	Experimental Determination of Time Delay . . . . .	87

<b>C Stability Analysis</b>	<b>89</b>
C.1 Routh-Hurwitz' Stability Criterion . . . . .	89
C.2 Jury's Stability Criterion . . . . .	92
<b>D Modified Linear Predictor</b>	<b>95</b>
<b>E PI Parameters</b>	<b>97</b>
<b>Bibliography</b>	<b>99</b>

# 1

# Introduction to Time Delay

Electrical machines are among the most used components in modern appliances and industrial applications found in an uncountable number of applications [1]. Its popularity has since its invention in the late nineteenth century, increased extensively and today, electrical machines are involved in almost all electricity production including hydroelectric turbines, wind power generators, nuclear power plants and traditional coal or oil fired power plants and are involved in more than 60% of the worlds electricity consumption [2]. This implies, that efficient design, control and understanding of electrical machines are among the most important topics in the field of electrical engineering.

Among the many electrical machines available, the synchronous machine and especially the Permanent Magnet Synchronous Machine (PMSM) has become increasingly popular the last decades. This is due to its high torque density and high efficiency [3, 4]. Applications for PMSMs span from low power-high performance servo drives to high power machine used in the wind industry [5]. Also, an increasing interest in PMSMs used for super high-speed drives with rotor speeds above 100,000 RPM has emerged [6].

For control of PMSMs, vector control including Field Oriented Control (FOC) and Direct Torque Control (DTC) are the main control methods used in the industry [3, 4, 7]. Due to the flexibility and excellent performance of digital control systems, this is the preferred choice when controlling electrical machines nowadays [8]. In high performance drive systems, Computer Numerically Controlled machines, robotics and other fields, accurate control is paramount for the machine to behave as desired. Even though conventional FOC in many cases has proved itself as a robust control method, it suffers as most other control methods from variation in plant parameters, which degrades the response, external disturbances and the unavoidable time delay of digital control system [8–10]. Time delays caused by the digital implementation of modern controllers introduces phase lag, which tend to destabilise the system and result in a sluggish dynamic response with significant overshoot [11, 12].

Normally the influence of time delays can be decreased significantly by increasing the switching frequency of the Voltage Source Inverter (VSI) supplying the electrical machine. With an increased focus in high-speed drives, and due to the fact that VSIs have a limited maximum switching frequency, time delay starts to influence the dynamics of the system considerably [10]. This means that, when the ratio between the sampling/switching frequency and the VSI output frequency (here called frequency-modulation ratio or  $m_f$ ) is low, time delay will have significantly negative effect on the control system. For a traction drive switching at approximately 1 kHz, this ratio can even be below 10. With a time delay of  $1.5T_s$ , this results in a phase shift of above  $20^\circ$  electrical of the output voltage

[10]. As described in [10], even with new IGBT technology capable of switching up to 20 kHz or more, a high-frequency direct-drive gas turbine needs a fundamental output frequency of a few kilohertz. With the technology available, it is not possible to increase the switching frequency and thus a low frequency-modulation ratio will be present. For a super high speed drive using a PMSM, the disadvantage of voltage distortion due to low  $m_f$  is mentioned in [13]. Here the authors propose a quasi-current source inverter in order to supply the machine with satisfactory current waveforms.

In [14], a VSI switching at 20 kHz is used to drive a super-high speed PMSM at 125,000 RPM, which in this application needs an inverter output frequency of 2 kHz. Here a frequency-modulation ratio of minimum 10 was used, and no compensation of time delays was considered. The machine phase currents were rather distorted, probably due to time delay problems caused by the low  $m_f$ .

Even though fast transistor technology is considered, some drives applications will need such a high input frequency, that the frequency-modulation ratio will still be below 10 as described in [10, 14]. For applications where a reduction of switching losses are important, a low switching frequency is desired, which could lead to a frequency-modulation ratio in a low range. In both cases the effects of time delay have to be compensated or mitigated in order to achieve a robust and stable control system of the drive.

## 1.1 Present Strategies for Time Delay Compensation

To compensate time delay effects in feedback processes, various predictors that address this problem are proposed. One of these methods is deadbeat control [15–17]. The principle behind deadbeat control is to predict a voltage from a discrete model of the plant, which will make the machine current reach its reference value in one sampling period. The predicted voltage is then translated into a switching configuration through Space Vector Modulation (SVM) and directly outputted to the machine terminals [17]. Deadbeat control is quite sensitive to circuit parameters, which over time might change value due to temperature rise and saturation effects. Therefore accurate machine parameters are essential in deadbeat control. Furthermore no integral term is included in this strategy, allowing a steady state error in the system when model mismatch exists between model and plant. Deadbeat control is however extremely fast since the reference is directly set as the output [15].

Another approach to compensate time delay is Model Predictive Control (MPC) [18]. Here a cost function is used to evaluate the error between the given reference current and the predicted current for the next sampling interval. A discrete model of the plant can be used to predict the currents in case of time delay and minimisation of this cost function will hence compensate those. This type of control often need large computational power and a precise system model [17, 19].

The Smith Predictor (SP) is another approach to mitigate problems governed by time delays [20]. The basic idea behind the SP is to feed back a simulated model of the plant including delay to cancel the physical plant. Then it adds the simulated plant without delay to the controller such that the delay is removed from the control loop [21]. In this way, assuming that the model of the system and delay are precise, this scheme in an ideal case, is able to remove the time delay from the control loop [22].

The predictive control methods described, are all shown to solve the problem in the

specific cases where they are implemented, but the research field does not contain an ultimate time delay compensator usable for any application. In [22], a SP shows good dynamic behaviour and in [15], deadbeat control is shown to maintain good output currents even with serious distortion levels on the voltages. In [23], MPC is shown to lower the Total Harmonic Distortion (THD) of the output current of an inverter with a sampling frequency of 6 kHz connected to a RL load. However, the SP is one of the most well and mature methods among these and is shown as a good choice in many applications [24, 25].

One disadvantage with the SP is its sensitivity towards model mismatch including parameter variation and time delay estimation of the plant [26]. Therefore many Modified Smith Predictors (MSPs) have been proposed [22, 24, 27]. In [26], an approximation of the unrealisable time delay  $e^{sT_d}$  is placed in the outer feedback loop of the conventional SP, which is shown to improve regulator response. In [25], an automatic tuning method for the Proportional Integral Derivative controllers in the Smith predictor is described and in [11], the authors suggest that feedback of extra dynamic elements should be included from either the process/plant or model output to improve time delay mismatch problems.

As described above, the SP and MSPs still need improvements. Since the method predicts the next output based on a given model, it requires relatively large computational resources. This might not be a problem if the response is slow, but in a fast system this could cause problems. This might explain, why in literature many implementations of the SP has been given for systems with relatively large time constants [22, 25, 28], and fewer implementations in electrical systems with fast responses. Another reason for this could be the large sensitivity towards model mismatch. In drives applications, the model dynamics are highly dependent on load conditions [29], where the resistance is temperature dependent and the inductance changes with saturation level, making it difficult to accurately know these parameters.

The SP is however a very mature predictor and with the recent focus on developing MSPs, this technique seems promising also in electrical drives applications.

## 1.2 Formulation of the Problem

From the description of stability issues and controller problems caused by time delays, together with the investigation of present strategies for time delay compensation, the problem statement is formulated as follows

*How can a predictive controller that successfully compensates time delays in low frequency-modulation ratio applications be designed, implemented and tested for a PMSM?*

To answer the above, a set of sub-questions is set up to more precisely formulate what should be included in order to solve this problem.

- How can FOC be implemented to control a PMSM?
- How does time delay influence the performance of FOC?
- How can a SP be designed to mitigate time delay problems?

- How can the predictor be made machine parameters independent or less sensitive to parameters variations?

These questions will form the basis of the project structure and highlight what theory and analysis tools that need to be understood in order to successfully answer the problem statement.

### 1.3 Project Outline

The objective of this project is to investigate controller problems and system destabilization when time delay or frequency-modulation ratio reaches values where conventional FOC using standard Proportional Integral (PI) controllers are not able to ensure system stability anymore. To mitigate this problem and improve system stability, a predictive controller capable of compensating the destabilising effects will be tested, and its performance compared to conventional FOC.

To accommodate this, an understanding of testing equipment, together with important theory and in depth analysis of the problem have to be established. The laboratory setup is introduced in chapter 2. An overall setup description is given along with theory, operation, and modelling of a PMSM.

In chapter 3, a detailed description of conventional FOC and how to properly tune PI controllers using classical control theory is given. In section 3.3, stability analysis using the proposed controller is done to investigate the destabilising effects of time delay.

In section 3.4, simulated results of FOC is presented and in section 3.5 these simulations are verified by experimental tests. Here the destabilising effects of increasing time delay is also reported, both experimentally and in simulation.

To be able to compensate time delay, chapter 4 introduces necessary theory of the SP together with simulated and experimental verification of the time delay compensation. Due to machine parameter dependency in the SP, a parameter sensitivity analysis is performed to investigate controller performance to parameter variations. This leads to section 4.5, where the inconvenience of a parameter dependent models is addressed. Here a Linear Predictor (LP) together with the Smith Predictor is investigated and its performance is tested and compared to FOC and SP using a Model Based Predictor (MBP). Modifications of the LP is investigated together with the underlying linearity. Furthermore, predictions based on inductance estimation is performed to achieve a model less sensitive to parameter variations. This increases the robustness of the controller and it is tested and compared to conventional FOC and SP. In the end, the findings and improvements of the work done is presented in chapter 5.

Appendices are included to give insight in some of the work done which do not explicitly need to be included in the main project. In appendix A, the physical laboratory setup is described including a description of the data acquisition done in the laboratory. Furthermore an in-depth description of the VSI including switching scheme is given. In appendix B, a description on how necessary machine parameters are found experimentally is given. In appendix C, an in depth analytical derivation of the stability analysis presented in section 3.3 is given. Appendix D describes the modifications to the LP. At last, appendix E gives an overview of what PI parameters that have been used on figures of simulated and experimentally tests and results throughout the project.

# 2

# Description of the Laboratory Setup

This chapter is dedicated to describe the system available in the laboratory. Firstly an explanation of the overall setup is given, then the PMSM is further described. The inverter including switching scheme is described in appendix A.1 and the dSPACE system together with data acquisition in appendix A.2.

In figure 2.1 an overall schematic of the setup in the laboratory is shown. It is seen, that the PMSM driven by a Danfoss VSI is connected to another PMSM. The Danfoss VSI is controlled by a dSPACE system connected to a PC running Simulink and dSPACE Control Desk. The load machine is connected to a resistive load via a variable-tap transformer, to be able to load the setup. The transformer is used to achieve desired torque even at low speeds. The dSPACE system is controlling the output voltage of the Danfoss VSI based on voltage and current measurements from several LEM transducers. Pictures of the physical setup together with a discussion and description of the measurement equipment can be found in appendix A.

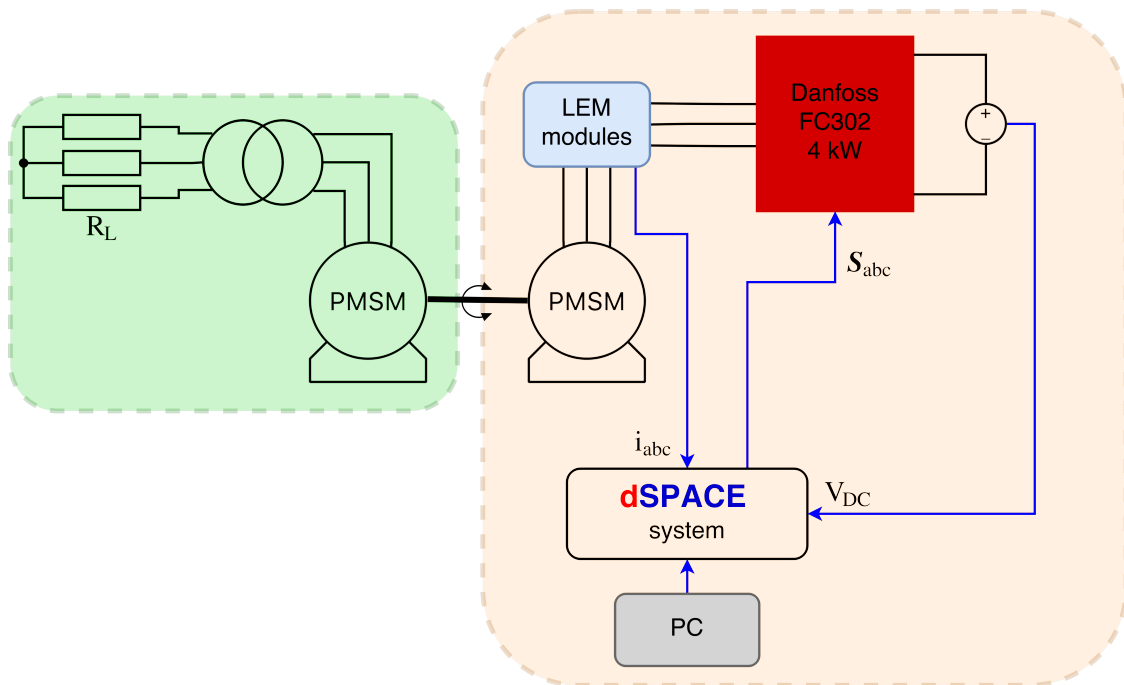


Figure 2.1: Schematic of the test setup. The green area is the load part of the setup, where the PMSM is acting as a generator. The orange box is the motor part with associated Danfoss VSI and dSPACE controller. Blue lines indicates I/O signals.

The two PMSMs in figure 2.1 are both manufactured by Siemens and have similar machine parameters. Since the aim of the project is to control the motor, a detailed description will only be given for this. In table 2.1 the rated values of the motor is visualised. It has surface mounted Permanent Magnets (PMs) and thus have equal direct and quadrature inductances. Measured values of the inductances, the stator phase resistance and the peak value of the PM flux linkage is presented in table 2.2. The values for the stator phase resistance and the inductances were performed in a previous project, whereas the PM flux linkage was found experimentally in a open-circuit test where the motor was operated as a generator. The determination of the PM flux linkage is described in appendix B.1.

<b>Siemens 1 FT6081-8H71 Brushless-Servomotor</b>	
Parameter	Value
$n_n$	4500 RPM
$p$	4
$T_n$	5.80 Nm
$I_n$	7.40 A

Table 2.1: Rated machine parameters for the PMSM

<b>Electrical Parameters of Siemens PMSM</b>	
Parameter	Laboratory value
$R_s$	0.68 $\Omega$
$L_d$	5.5 mH
$L_q$	5.5 mH
$\lambda_{mpm}$	0.1151 Wb.t

Table 2.2: Measured machine parameters for the PMSM.

The combined moment of inertia  $J$  is the sum of the inertia in the system. Since the motor PMSM is connected to a load PMSM via a coupling the total moment of inertia is given as

$$J = J_{PMSM} + J_{Load-PMSM} + J_{Coupling}.$$

The combined moment of inertia of the setup was found experimentally as described in appendix B.2. The value was found to be  $14.82 \cdot 10^{-3}$  kg·m<sup>2</sup>. Additionally the viscous friction coefficient and the Coulomb friction were determined to be  $B_m = 1.596 \cdot 10^{-3}$  Nm·s/rad and  $J_0 = 5.02 \cdot 10^{-3}$  Nm respectively.

<b>Danfoss FC302 VSI 15 kW</b>	
Parameter	Value
$V_{in}$	380-500 V
$V_{out}$	0-500 V
$I_{in}$	9.0 A
$I_{out}$	10 A
$t_{dead}$	2.5 $\mu$ s
$f_{out}$	0-1000 Hz

Table 2.3: Rated inverter parameters.

As seen in figure 2.1, the setup is driven by a Danfoss FC302 which has the rated values as shown in table 2.3. Relevant theory of the VSI, together with a description of the selected

modulation scheme is presented in appendix A.1. The total equivalent resistance of setup including the average IGBT on-resistance, the resistance of connected wires and phase resistance of the PMSM is measured to be  $1.1253 \Omega$  at a switching frequency of 5 kHz. This value will be used when designing controllers for the machine, since this is the actual resistance seen from the controller side. The switching frequency of the drive is changeable and will together with the motor speed be adjusted to change the modulation-frequency ratio.

## 2.1 Permanent Magnet Synchronous Machine (PMSM)

This section has the purpose of introducing the modelling of the PMSMs shown in the setup in figure 2.1. This is done in order to describe the problem mathematically and later be able to use classical control theory to design PI controllers for FOC. Through this, the advantages of introducing a rotating reference frame is described and how the machine can be modelled in this frame is shown.

In stator variables the relation between the terminal voltages and the phase currents are

$$\mathbf{v}_{abcs} = R_s \mathbf{i}_{abcs} + \frac{d}{dt} \boldsymbol{\lambda}_{abcs},$$

where

$$\boldsymbol{\lambda}_{abcs} = \mathbf{L}_s \mathbf{i}_{abcs} + \boldsymbol{\lambda}_{pm}.$$

$\mathbf{L}_s$  is the inductance matrix

$$\mathbf{L}_s = \begin{bmatrix} L_{asas} & L_{asbs} & L_{ascbs} \\ L_{bsas} & L_{bsbs} & L_{bscbs} \\ L_{csas} & L_{csbs} & L_{cscbs} \end{bmatrix}$$

and

$$\boldsymbol{\lambda}_{pm} = \lambda_{mpm} \begin{bmatrix} \sin(\theta_e) \\ \sin(\theta_e - \frac{2\pi}{3}) \\ \sin(\theta_e + \frac{2\pi}{3}) \end{bmatrix},$$

where  $\lambda_{mpm}$  is the amplitude of the PM flux linkage and  $L_{xays}$  are the self and mutual inductances between the three phases [30]. In stator variables, the phase self- and mutual inductances and the PM flux linkage is rotor position dependent. Therefore it is advantageous to express the voltage equations in a rotating reference frame where the inductances and PM flux linkage becomes rotor position independent. In this project, a  $dq0$  reference frame is used, which is visualized in figure 2.2. As can be seen in figure 2.2, the  $d$ -axis is located  $\theta_e$  away from the  $a$ -axis, which is the flux axis of phase- $a$ . The  $d$ -axis is located at the north pole of the permanent magnets and the  $q$ -axis is leading the  $d$ -axis by  $90^\circ$  electrically.

As explained in section A.1, a three phase system can be reduced to a two-axis reference frame, here the  $dq0$ -reference frame. To ensure that the information is the same before and after transformation, the two representations need to have one common variable, which is

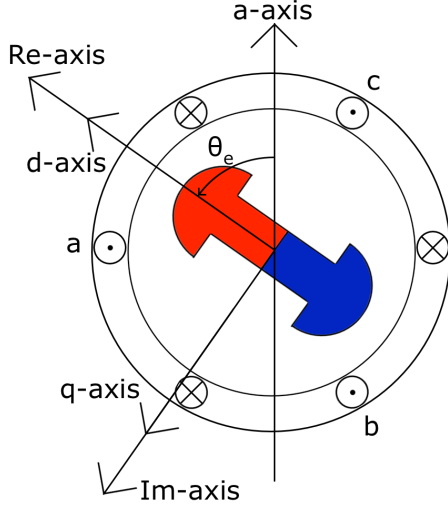


Figure 2.2: Visualisation of the chosen  $dq0$  reference frame. The magnet north pole is represented as red and the south pole is represented as blue.

the zero component expressed as

$$f_0 = \frac{1}{3}(f_a + f_b + f_c).$$

In a symmetrical three-phase system the zero component is zero and the three-phase signal can be represented by the space vector

$$\mathbf{f} = \frac{2}{3}(f_a e^{j0^\circ} + f_b e^{j120^\circ} + f_c e^{j-120^\circ}),$$

which is the same as for the  $\alpha$  and  $\beta$  components (equation A.1.2). In the  $dq0$ -reference frame, the vector is

$$\mathbf{f} = (f_d + j f_q) e^{j\theta_e},$$

which is found by projecting the vector to its  $dq$  components.  $\theta_e$  is the angle between the flux- $a$  axis and the  $d$ -axis.

The Park transformation introduced by Robert Park in 1928 can be used to transform a stationary  $abc$ -reference frame to a rotating  $dq0$ -reference frame as

$$\mathbf{K}_s = \frac{2}{3} \begin{bmatrix} \cos(\theta_e) & \cos(\theta_e - \frac{2\pi}{3}) & \cos(\theta_e + \frac{2\pi}{3}) \\ -\sin(\theta_e) & -\sin(\theta_e - \frac{2\pi}{3}) & -\sin(\theta_e + \frac{2\pi}{3}) \\ \frac{1}{2} & \frac{1}{2} & \frac{1}{2} \end{bmatrix}$$

[31]. The transformation from the rotating reference frame to the stationary frame can be described by the inverse matrix.

When transforming the voltage equations for the PMSM into the rotating  $dq0$ -reference frame one obtains

$$v_d = R_s i_d + \frac{d\lambda_d}{dt} - \omega_e L_q i_q \quad (2.1.1)$$

$$v_q = R_s i_q + \frac{d\lambda_q}{dt} + \omega_e L_d i_d + \omega_e \lambda_{mpm} \quad (2.1.2)$$

$$v_0 = R_s i_0 + \frac{d\lambda_{ls}}{dt},$$

where the permanent magnet flux linkage is assumed to be constant [30].  $R_s$  is the phase resistance, and  $d\lambda_d/dt = dL_d i_d/dt$  with  $L_d$  being the  $d$ -axis inductance and  $d\lambda_q/dt = dL_q i_q/dt$  with  $L_q$  being the  $q$ -axis inductance. Using the steady state voltage equations, the output power is

$$P_{out} = \frac{3}{2} (v_d i_d + v_q i_q + 2v_0 i_0).$$

Based on the fact, that the phase resistance has no influence on torque and that the torque is the output power divided by the mechanical speed, the electromagnetic torque can be found to be

$$T_e = \frac{3p}{2} (\lambda_{mpm} i_q + (L_d - L_q) i_q i_d). \quad (2.1.3)$$

The first term contributes to the main part of the torque, called the PM interaction torque. The second torque term is called the reluctance torque and is caused by the saliency of a machine, which exists for Interior Mounted PMSM. For a Surface Mounted PMSM (SPMSM), the reluctance torque can be assumed zero and only the PM interaction torque contributes to torque generation. The machine available in this project is a SPMSM which means that the  $d$ - and  $q$ -axis inductances can be considered equal and the machine will therefore only produce PM interaction torque.

The mechanical equation relating the torque and the speed is

$$T_e = J \frac{d}{dt} \omega_m + B_m \omega_m + T_L, \quad (2.1.4)$$

where  $J$  is the moment of inertia,  $B_m$  is the viscous friction coefficient and  $T_L$  is the load torque. Generally the Coulomb friction  $J_0$  can be included in the term  $T_L$ .



# 3

# Field Oriented Control of a PMSM

Vector control including FOC and DTC are widely used methods for controlling synchronous machines in the industry [3, 4, 7, 32]. The objective of both, is to control the instantaneous machine torque delivered to the load while operating the machine at a desired speed. This has to be accurately done regardless of load changes, machine parameter variations and external disturbances.

FOC originates from the control of DC machines where the currents producing flux and torque are independent. By holding the flux constant by controlling the field winding current, the torque can simply be controlled by the armature current. The advantage of having a decoupled control of flux and torque can be achieved for synchronous AC machines as well by transforming the stationary stator current into flux and torque producing current in the *dq*-reference frame [32].

As described in equation 2.1.3, the torque of a PMSM is independent of speed and is determined only by the *dq*-axis currents. From the torque reference obtained from the reference speed  $\omega_m^*$  (by equation 2.1.4), the reference currents can be calculated (using equation 2.1.3). Then, by using equations 2.1.1, 2.1.2 the necessary voltages can be calculated. Since a SPMSM is a non-salient machine, the torque produced is

$$T = \frac{3}{2} p \lambda_{mpm} i_q,$$

where  $\lambda_{mpm}$  is assumed to be constant. Therefore the machine torque is only dependent on the *q*-axis current, thus the torque can be directly controlled by means of the *q*-axis current. By this, independent control of torque and flux is obtained.

To achieve maximum torque of the machine, the angle between the stator flux vector (created by the stator windings) and the rotor flux vector (created by the PMs) has to be  $90^\circ$ . In the *dq*-reference frame this corresponds to a current vector which should be oriented at the *q*-axis and thus this type of control is sometimes called field angle control [3].

To reduce losses in the machine, the *d*-axis current is controlled to be zero. This is true when the machine operates below rated speed. If a higher speed is to be used, often field weakening is introduced and the *d*-axis current is controlled to be negative [33].

The location of the excitation rotor flux is always known since the PM flux linkage is aligned with the *d*-axis. Thus its position can be identified by use of an encoder to monitor the rotor position.

To ensure fast torque response without steady state errors, PI controllers will be used to control the current and the speed of the machine. The control structure of FOC can be seen in figure 3.1.

One PI controller is used in an outer speed loop and two PI controllers in an inner current loop. The speed controller and the *q*-axis current controller form a cascaded

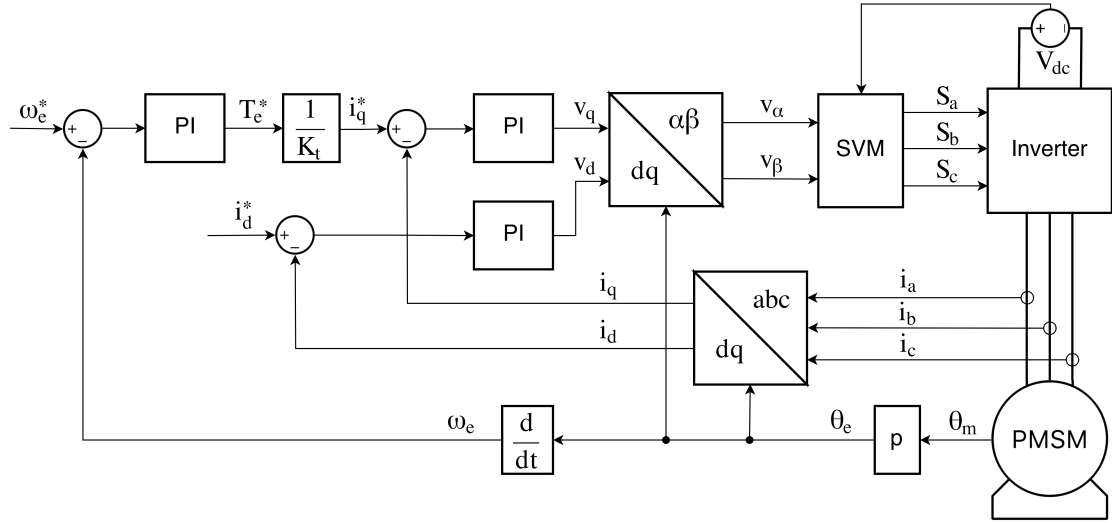


Figure 3.1: Field Oriented Control of a PMSM with two inner current loops and one outer speed loop.

controller that provides better rejection of disturbances compared to a single controller. The cascaded controller is useful in this application, since the current response is much faster than the speed response. For a cascaded controller, the inner loop has to be at least ten times faster than the outer loop, for the control to operate properly [21].

The output of the current controllers are the voltage commands for the machine. These voltages are transformed into a voltage space vector in the stationary reference frame, where SVM is performed to send the desired switching pulses to the inverter transistors.

The machine rotor position is measured using an encoder. This is used to perform the Park transformation and to calculate the rotor speed used in the outer speed loop. The speed error is fed into the speed controller which outputs the reference *q*-axis current.

Now the control structure of the FOC has been presented and the tuning of the three PI controllers has to be examined. Because the dynamic of the current controllers will have to be much faster (10x) than the dynamics of the speed controller, the inner current loop is approximated as a unity gain for a system without time delay and a first order lag response for system with time delay, when designing the speed controller. Thus, the inner and outer loop can be analysed and tuned independently [21, 34]. The controller designs will be based on linear control theory.

### Controller requirements

This paragraph has the purpose of introducing the requirements for the closed loop controlled system. The requirements are selected as a reference for the controllers in this project. These will later be used to validate if predictive control can fulfil these requirements during a frequency-modulation ratio lower than what classical FOC can achieve.

- A maximum overshoot in the current loop of 2%.
- A maximum overshoot in the speed loop of 10%.
- The bandwidth of the current loop should be 500 Hz.
- The speed loop should be at least ten times slower than the current loop.

### 3.1 Controller Design Without Time Delay

The design of the controllers for the inner current loop will be derived from the voltage equations presented in equations 2.1.1, 2.1.2. To keep the analytical analysis simple, only the two or three most dominant system poles will be considered. The design will both be done in continuous and discrete domain. The inverter model is neglected regarding dead time, making it linear in nature and thus appear as a simple gain. This gain will simply be compensated in the controller afterwards and will therefore not be present in the control structure to be presented. In the design of controllers for both the inner current loop and the outer speed loop, the controller zero is placed to cancel the slowest pole of the plant to be controlled. This is in general not a good approach since variations in machine parameters due to changes in temperature and saturation levels will not make the controller cancel the plant pole in a physical setup. Hence the controller zero can in general be placed a better place. However this zero-pole cancellation method is used in this project, since it simplifies the overall system and gives a good initial design for the controller when implementing it in an experimental setup.

For the first design, the system is assumed to include a controller and the plant ignoring the effect of time delay.

The voltage equations of the PMSM in the Laplace domain are

$$v_d(s) = R_s i_d(s) + s L_d i_d(s) - \omega_e L_q i_q(s) \quad (3.1.1)$$

$$v_q(s) = R_s i_q(s) + s L_q i_q(s) + \omega_e L_d i_d(s) + \omega_e \lambda_{mpm}. \quad (3.1.2)$$

As can be seen from equations 3.1.1 and 3.1.2, the two voltage equations are coupled due to the back-EMF voltage term in each of them. To use classical control theory these equations have to be decoupled. This can be done in two ways. In the first method, the coupled terms can be seen as disturbances to the system and therefore neglected in the controller design. Alternatively, since both machine velocity and the *dq*-axis currents are measured, these coupled terms can be removed from the control structure by subtracting the back-EMF term in the *d*-axis current loop and adding it in the *q*-axis current loop. This is known as back-EMF decoupling [35]. This can be seen in figure 3.2, where the principle is shown for the *d*-axis current. Since the physical machine configuration cannot be changed, the back-EMF decoupling term can be used to simplify the analysis.

Using back-EMF decoupling, the machine plant can now be described from the *dq*-voltages to the *dq*-currents as

$$\begin{aligned} \frac{i_d(s)}{v_{d,PI}(s)} &= \frac{1}{R_s + sL_d} \\ \frac{i_q(s)}{v_{q,PI}(s)} &= \frac{1}{R_s + sL_q}, \end{aligned} \quad (3.1.3)$$

where  $v_{d,PI}$  and  $v_{q,PI}$  is used to distinguish the voltage applied to the machine terminals with the voltage from the PI controller, when the equations are decoupled as seen in figure 3.2. Since  $L_d = L_q$ , only one of the current controllers has to be designed, since they will be identical. When the back-EMF voltage is decoupled, the open loop transfer function is

$$G_{ol} = G_c G_p = \frac{K_{p,c}s + K_{i,c}}{s(R_s + sL)} = \frac{\frac{K_{i,c}}{K_{p,c}} + s}{s/K_{p,c}} \frac{1/L}{\frac{R_s}{L} + s},$$

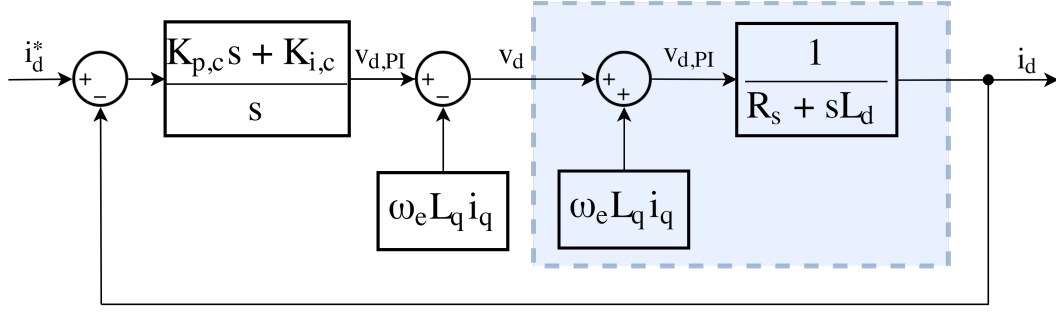


Figure 3.2: The back-EMF decoupling of the  $d$ -axis current loop including the plant and a PI controller. The blue area represents the machine which configuration cannot be changed.

where  $L$  is the value of the  $d$  or  $q$ -axis inductance. A common approach which is described in [34], is to choose the zero of the controller to cancel the pole of the plant. By doing so the open loop transfer function reduces to a first order system, which is stable for all values of  $K_p$ . The gain can then be adjusted to obtain the desired settling time or rise time. For the zero of the controller to cancel the plant pole

$$\frac{K_{i,c}}{K_{p,c}} = \frac{R_s}{L}.$$

In [34], the proportional gain is suggested to be

$$K_{p,c} = \alpha_c L,$$

where  $\alpha_c = \ln(9)/t_r$  is derived from the rise time of a first order system and therefore represents the bandwidth.

### Controller Design for Outer Speed Loop

From equation 2.1.3 and 2.1.4, which describe the machine torque in terms of electrical and mechanical parameters, the transfer function from the  $q$ -axis current to the mechanical speed is

$$G_s(s) = \frac{\omega_m(s)}{i_q(s)} = \frac{1}{Js + B_m},$$

where the load torque  $T_L$  can be seen as a disturbance in the speed loop. Since the dynamics of the current loop is much faster than the dynamics of the speed loop, the current loop seen from the speed loop is approximated with a unity gain. To control the speed loop, the zero of PI controller is made such that it cancels the pole of the mechanical plant, which is

$$\frac{K_{i,s}}{K_{p,s}} = \frac{B_m}{J}.$$

Since the bandwidth of the speed loop is desired to be ten times slower than the speed loop, the proportional gain is calculated as

$$K_{p,s} = \frac{\alpha_c}{10} \frac{J}{K_t},$$

which is also described in [34]. Figure 3.3 shows a block diagram of the speed loop including the PI controller and the current loop gain.

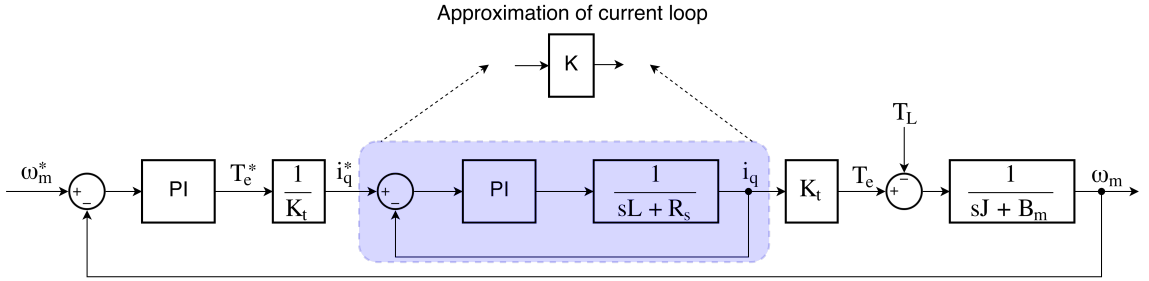
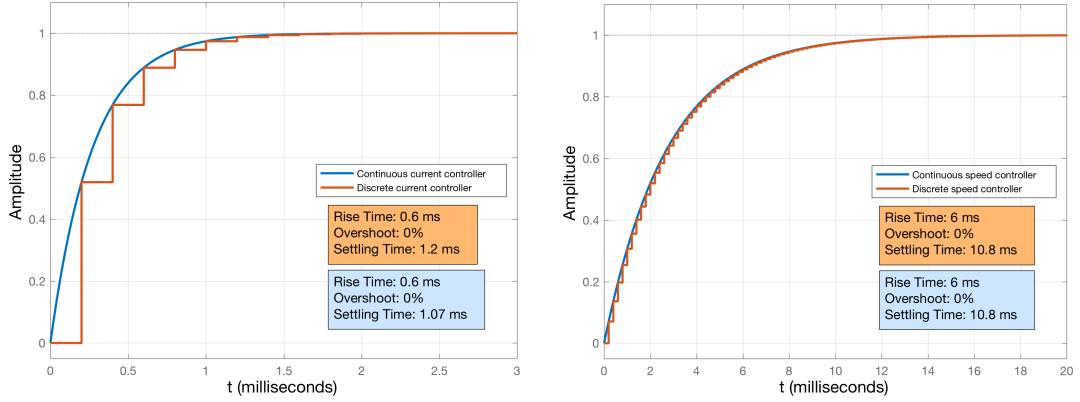


Figure 3.3: Block diagram of speed loop including a PI controller, a gain approximation of the inner current loop and the mechanical plant.



(a) Unit step of closed current loop with controller.  $K_{p,c} = 20.14$  and  $K_{i,c} = 4121$ .

(b) Unit step of closed speed loop with controller.  $K_{p,s} = 0.846$  and  $K_{i,s} = 7.859$ .

Figure 3.4: Sampling frequency for both graphs is 5 kHz.

In figure 3.4(a) and 3.4(b), a step response of the current and speed loop behaviour is seen, both for continuous and discrete time. The PI parameters obtained were calculated to  $K_{p,c} = 20.14$  and  $K_{i,c} = 4121$  for the current controller and  $K_{p,s} = 0.846$  and  $K_{i,s} = 7.859$  for the speed controller. The sampling frequency used for the discretisation is 5 kHz. As seen in the figures, both the current and the speed have the desired rise times and without any overshoot. This is because the system is modelled as a first order system, which when implemented in a digital computer is not true anymore, especially not when time delay is considered.

For the discrete response shown, the discretisation can be done with discrete equivalents or by emulation, where the continuous time transfer functions are approximated in discrete time. Different techniques are available to do this discretisation including Tustin, Zero Order Hold (ZOH) and matched pole-zero method. The plant transfer function should be discretised using the ZOH method, since this is how the signals are provided to it in the physical system, whereas often the matched pole-zero method is used to discretise the controller [21], as it is in this case. The Tustin method only gives good approximations when the frequency-modulation ratio is above 25. In general, discrete design by emulation should only be used, when the frequency-modulation ratio is above 25 and at minimum 10. If this is not fulfilled a full discrete design should be utilized. If design by emulation is to be used for  $m_f \approx 10$ , the design should be carefully analysed using discrete analysis tool and the controller parameters might need to be adjusted [21]. The next section will not

rely on design by emulation for the discrete response of the system, but on a full discrete design even though the difference might not be crucial.

### 3.2 Controller Design Including Time Delay

In the following sections, modelling of time delay in both continuous and discrete time will be described. Stability analysis of the closed loop poles of the system will be done and the PI controllers described in previous sections will be retuned to the case of time delay, both in continuous and discrete time.

#### Continuous Time Delay Approximation

The system to be controlled is now modelled as a PI controller, a time delay and the plant. An exact expression for the time delay in the Laplace domain is

$$G_D(s) = e^{-sT_d}, \quad (3.2.1)$$

where  $T_d$  is the time delay [21]. The phase of the exact delay can be seen in figure 3.5(a). Here it is evident from the line at  $-180^\circ$ , that for a value of  $\omega = 3/T_d$  it is impossible to stabilize the system since the phase margin will be negative. This example is conducted in the ideal case where both the plant and controller does not contribute to phase lag, so in reality it would become unstable before  $\omega = 3/T_d$ . This shows the influence of the time delay on the decrease in bandwidth and phase margin.

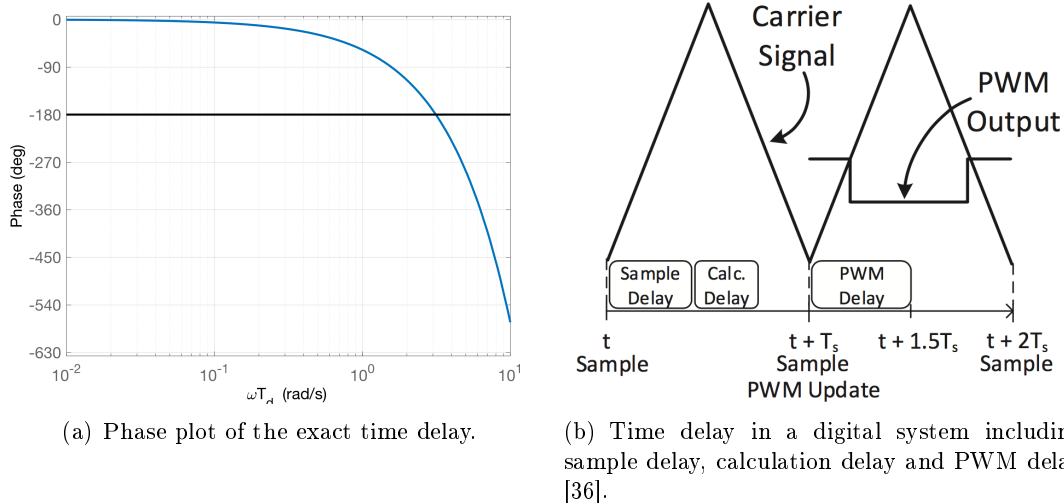


Figure 3.5: Phase characteristics and origin of time delay.

The cause of time delay in a digital control system can be seen in figure 3.5(b). In all digital systems there is a delay associated with the time it takes to sample a signal in the Analog to Digital Converter (ADC). After the sampling delay, the control algorithm takes time to calculate the next switching state of the VSI based on the measured quantities. After the calculation delay, the Microcontroller ( $\mu$ C) will have to wait until the next sample instant to update the calculated switching state. The modulator has a delay of a half sampling period. This is the average time for the modulation technique to generate the

desired output voltage [37, 38]. This means that a delay of  $0.5T_s$  is present from the Pulse Width Modulation (PWM) update to a average change in output voltage. Actually the modulator applies a series of inverter states (see section A.1) to produce the desired output voltage. To assume the average voltage to be applied at the beginning of this period is unrealistic. If instead it is said to be applied at the end of the period, a too conservative estimate is given. Therefore the average voltage is estimated to be applied at half of the switching period [38]. For the digital system used in this project, the time delay should be  $1.5T_s$ , where  $T_s$  is the sampling period. This is verified in appendix B.3

As explained in [21], Bode plots and Nyquist diagrams can be drawn with the expression of the exact time delay and stability analysis can be carried out by inspection together with simulation. However, stability analysis cannot be done analytically for approaches which uses the characteristic equation of a rational transfer function to analyse the system. Therefore if more in-depth analytical analysis is desired including Routh-Hurwitz' stability criterion and root locus analysis, an approximation of the time delay is needed.

One such approximation is the Padé approximation. The Padé approximation is based on the Maclaurin series of the exponential function which is

$$e^{-x} = \sum_{k=0}^{\infty} \frac{(-x)^k}{k!} = 1 - x + \frac{x^2}{2!} - \frac{x^3}{3!} + \frac{x^4}{4!} - \dots + \dots \quad (3.2.2)$$

The Padé approximation of order  $(m, n)$  is defined as the rational function  $R_{m,n}(x)$  of the Maclaurin series expressed as

$$R_{m,n}(x) = \frac{P_m(x)}{Q_n(x)}$$

with the polynomials being

$$P_m(x) = \sum_{k=0}^m \frac{(m+n-k)!m!}{(m+n)!k!(m-k)!} (-x)^k$$

and

$$Q_n(x) = \sum_{k=0}^n \frac{(m+n-k)!n!}{(m+n)!k!(n-k)!} (-x)^k.$$

When comparing equation 3.2.1 with 3.2.2 it is clear that to get the transfer function of the Padé approximation, the only necessary step is to substitute  $x = sT_d$  [39]. From this a well known (and very crude [21]) approximation of the time delay is given with  $m = 0$  and  $n = 1$  to be

$$e^{-T_d s} \approx \frac{1}{1 + T_d s}. \quad (3.2.3)$$

As proposed in [21], and verified in [36] the nonrational delay is well approximated by a second order Padé approximant ( $m = n = 2$ ) expressed as

$$e^{-T_d s} \approx \frac{1 - \frac{T_d s}{2} + \frac{(T_d s)^2}{12}}{1 + \frac{T_d s}{2} + \frac{(T_d s)^2}{12}}. \quad (3.2.4)$$

In figure 3.6, the closed loop step response of the  $(0,1)$  Padé approximation (equation 3.2.3) and the  $(2,2)$  Padé approximation (equation 3.2.4) is compared to the exact delay (equation 3.2.1). A plant similar to equation 3.1.3 with the machine parameters inserted

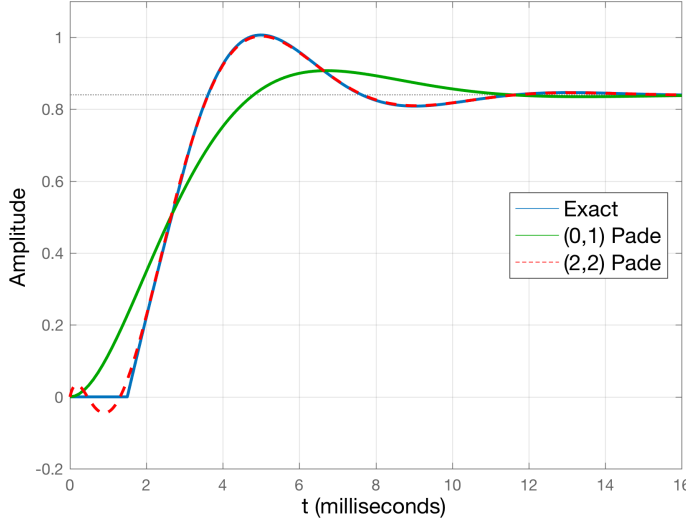


Figure 3.6: Comparison of step response of (0,1) Padé approximation (equation 3.2.3) and the (2,2) Padé approximation (equation 3.2.4) with exact delay (equation 3.2.1).

is used for the comparison. It is seen that the simple approximation of equation 3.2.3 is not capable to resemble neither the right shift in time nor the right overshoot, whereas the second order Padé approximation shows similar behaviour.

### Discrete Time Delay Approximation

To approximate the time delay in discrete time, a mapping of the continuous Padé approximation (e.g. equation 3.2.4) to the discrete time domain is done by using the Tustin method. As described earlier, the Tustin method only gives a good approximation of the system, if the modulation frequency is above 25. Therefore other methods will also be investigated.

Consider the transfer function

$$G(s) = e^{-T_d s} H(s).$$

If an integer  $l$  is defined together with a positive number  $m$  less than one, then  $T_d$  can be expressed as  $T_d = lT_s - mT_s$ . Then

$$\frac{G(s)}{s} = e^{-lT_s s} \cdot \frac{e^{mT_s s} H(s)}{s}. \quad (3.2.5)$$

If

$$H(s) = \frac{K}{s + a},$$

which is the case for the plant of this project, then

$$G(z) = \frac{z - 1}{z^{l+1}} \frac{K}{a} \mathcal{Z} \left\{ \frac{e^{mT_s s}}{s} - \frac{e^{mT_s s}}{s + a} \right\},$$

where the first term in the  $\mathcal{Z}$ -transform is a unit step shifted left by  $mT_s$  seconds and the second term is an exponential shifted by the same amount. The samples are given as  $1(kT_s)$  and  $e^{-aT_s(k+m)}1(kT_s)$  which has the  $\mathcal{Z}$ -transforms  $z/(z-1)$  and  $ze^{-amT_s}/(z-e^{-aT_s})$

respectively [40]. The transfer function in discrete time is therefore

$$G(z) = \frac{z-1}{z^{l+1}} \frac{K}{a} \left\{ \frac{z}{z+1} - \frac{ze^{-amT_s}}{z - e^{-aT_s}} \right\}. \quad (3.2.6)$$

Another approach to model a fractional delay is by a so called Thiran filter. This is an allpass filter with unity gain in the entire frequency band. The  $N^{th}$  order Thiran filter is given by the following transfer function

$$H(z) = \frac{z^N A(z^{-1})}{A(z)} = \frac{z^{-N} (a_0 + a_1 z + \dots + a_N z^N)}{a_0 + a_1 z^{-1} + \dots + a_N z^{-N}} \quad (3.2.7)$$

where

$$a_k = (-1)^k \binom{N}{k} \prod_{n=0}^N \frac{d+n}{d+k+n} \quad \forall k = 0, 1, 2, \dots, N \quad (3.2.8)$$

where  $N$  is the order of the filter given as the ceiling value of  $T_d/T_s$  and  $d$  is the fractional part of the delay in the range -1 to 0 calculated as  $d = T_d/T_s - N$  [41, 42]. With a time delay of  $1.5T_s$ , the second order Thiran approximation of the delay becomes

$$H(z) = \frac{-0.02857z^2 + 0.4z + 1}{z^2 + 0.4z - 0.02857}.$$

To compare the different approximations, a plant with the a transfer function similar to that shown in equation 3.1.3 is used. A sampling period,  $T_s$ , of 1 ms is used (this results in a larger overshoot and hence it is easier visually to compare the different methods) together with a time delay,  $T_d$  of  $1.5T_s$ . When using equation 3.2.6 the coefficients will be

$$a = \frac{R_s}{L} \quad \text{and} \quad K = \frac{1}{L}$$

since  $L_d = L_q = L$ . In figure 3.7 the open loop bode plot of the different techniques is plotted together with the exact delay given by equation 3.2.1. It is seen that at low

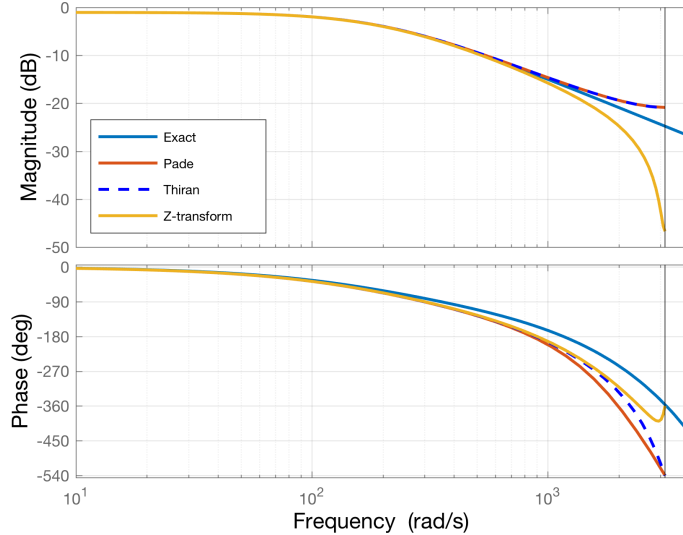


Figure 3.7: Bode plot of discrete time delay approximations compared with exact delay. In the magnitude plot the Padé and Thiran methods are identical.

frequencies all three methods gives a good approximation of the time delay. However, as

the frequency approach the Nyquist frequency the deviation between the exact delay and the approximations become larger. The  $\mathcal{Z}$ -transform method shows quite large deviations in the magnitude plot, when the frequency increases compared to the two other methods. The Padé and Thiran approximations shows exactly the same magnitude behaviour, but the Thiran filter resembles the phase of the exact delay slightly better.

To further investigate the differences between the methods, a step is given to the closed loop transfer function of the system to see the dynamic response. This is shown in figure 3.8. It is seen that the methods show almost identical responses with an overshoot which

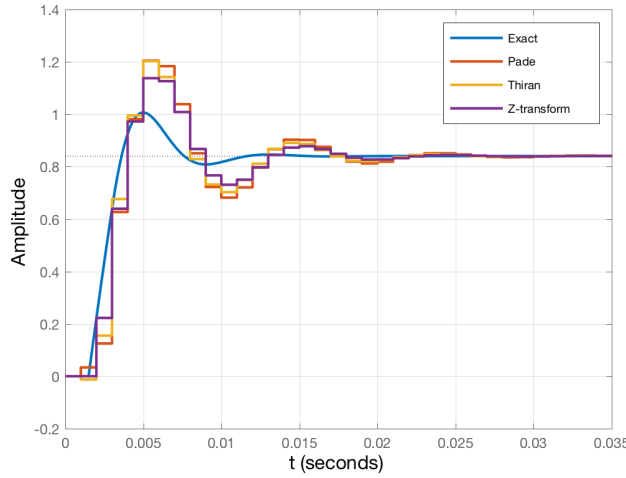


Figure 3.8: Comparison of closed loop step response of plant proceeded with ZOH and  $T_d = 1.5T_s$ . At  $t = 0$  a unit step is provided.

is larger than that of the exact delay and slightly shifted in time. This could indicate that the approximations are estimating a time delay which is larger than the one given with the exact delay. To transform the plant from continuous time to discrete time a ZOH is used. This is done since the ZOH exactly resembles the effects of the ADC in the physical system. The plant proceeded by a ZOH will however introduce a half period of delay [21, 38] and thus the total delay will be  $0.5T_s$  larger. It is noted that the delay introduced by the modulator is also equivalent to  $0.5T_s$ , so when a ZOH is used together with a unit delay, the total equivalent time delay will be  $1.5T_s$ , which is the desired value. In figure 3.9, the step response is shown where a unit delay is used together with a plant proceeded with a ZOH. It should be noted, that in equation 3.2.5 when  $l = 1$  and  $m = 0$  the exact unit delay of  $z^{-1}$  is present. The same is the case with the 1<sup>st</sup> order Thiran filter given in equation 3.2.7 and 3.2.8 with  $N = 1$  and  $d = 0$ .

In figure 3.9 it is seen that the delay is now modelled almost exactly both with the Thiran method (which is actually a unit delay in this case) and with the Padé approximation. The Padé approximation is however still an approximation and thus gives a slightly worse response. In figure 3.7, 3.8, and 3.9 the values of  $R_s$  and  $L$  is not the physical machine parameters. This is chosen to make an easier visual comparison between the different methods.

### 3.2.1 Continuous Time Controllers

The continuous time controllers including time delay will in this subsection be designed for both the current and speed loop. The current loop is tuned iteratively using an initial

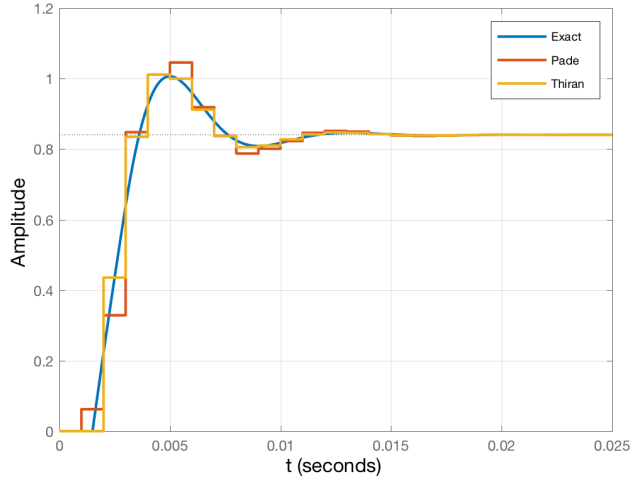


Figure 3.9: Comparison of closed loop step response when a unit delay together with a ZOH is used.

guess based on classical control theory. For the speed loop, a discussion on how to treat the inner current loop is also given.

### Controller Design for Inner Current Loop

The open loop model when designing the current controller is a PI controller together with an approximation of the physical setup. The physical plant for the current loop is modelled as a second order Padé approximation together with the electrical decoupled machine model, which is

$$G_p(s) = \frac{T_d^2 s^2 - 6T_d s + 12}{(T_d^2 s^2 + 6T_d s + 12)(Ls + R_s)}.$$

The desired bandwidth of the system is 500 Hz, hence the closed loop magnitude at 500 Hz should be -3 dB. To tune the controller, the phase margin is often used, which is related to the desired overshoot in a system. For a third order system there is no analytical relation between the overshoot and the phase margin, but there is for a second order system. Assuming that the system can be approximated by a second order system, the overshoot is related to the damping coefficient as

$$\zeta = \cos \left( \tan^{-1} \left( \frac{-\pi}{\ln(OS\% / 100)} \right) \right)$$

which is related to the phase margin as

$$PM = \tan^{-1} \left( \frac{2\zeta}{\sqrt{\sqrt{1+4\zeta^4} - 2\zeta^2}} \right) \cdot \frac{180}{\pi}$$

Thus, by considering a maximum overshoot of 2%, the phase margin should be approximately 77° [21]. This is in the case of a second order system, hence the estimated phase margin needed might not correspond exactly to the desired closed loop performance, but is used as an initial guess for the phase margin.

To find the values of the proportional and integral gains, the frequency at which the desired phase margin occurs is found. This is  $\omega_1$  in

$$\angle G_p(j\omega_1)H(j\omega_1) = -180^\circ + PM + 5^\circ,$$

where  $H(s)$  represents the feedback gain which in this case is unity. For the open loop transfer function given,  $\omega_1$  is found to be 171.9 Hz. The proportional gain should be equal the reciprocal of the magnitude at that frequency. At 171.9 Hz, the magnitude is -15.6 dB, leading to a proportional gain of

$$K_{p,c} = \frac{1}{10^{\frac{-15.6}{20}}} = 6.026.$$

The magnitude of the controller zero is selected to be placed one decade before  $\omega_1$  [43], so

$$\frac{K_{i,c}}{K_{p,c}} = 0.1\omega_1 \Rightarrow K_{i,c} = 0.1\omega_1 K_{p,c} = 0.1 \cdot 2\pi \cdot 171.9 \cdot 6.026 = 650.81$$

As can be seen in figure 3.10(a), the response has no overshoot which suggests that the chosen phase margin was too conservative compared with the controller requirements. Also the evaluated settling time is not desirable. Furthermore when evaluating the bandwidth of the system, this was found to be 260.2 Hz, which in the step response corresponds to a rise time of 1.7 ms. This is much lower than the desired bandwidth of 500 Hz. From this, the initial design can be made faster by allowing the controller to have an overshoot of 2% as specified in the controller requirements. The retuned parameters were done iteratively in MATLAB and the values obtained were  $K_{p,c} = 8.3$  and  $K_{i,c} = 1770$ . This resulted in the desired bandwidth of approximately 500 Hz with an overshoot below 2%, which can be seen in figure 3.10(b). This design has a phase margin of 63.7°, which also concludes that the initial guess of 77° was too conservative.

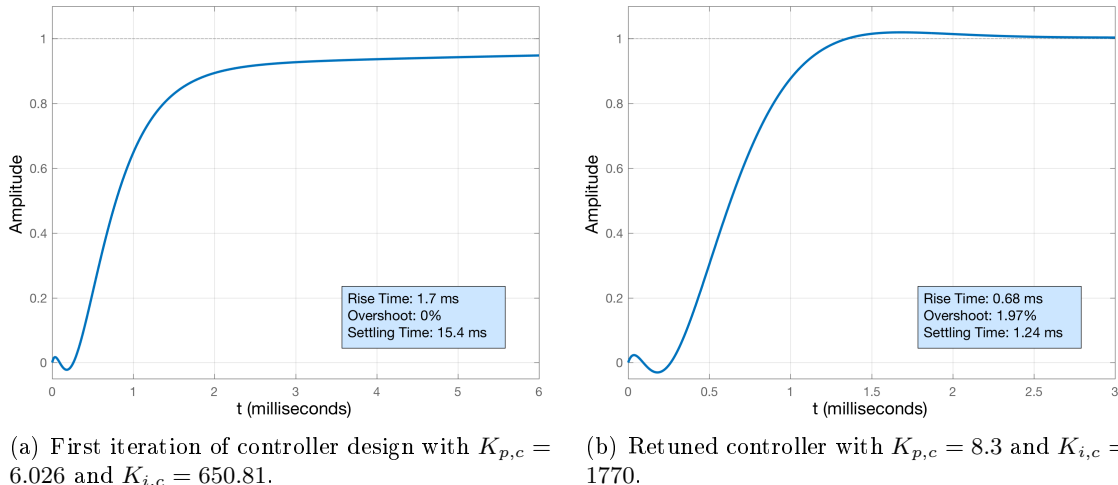


Figure 3.10: Feedback step response of the controlled plant including second order Padé approximation as time delay.

### Controller Design for Outer Speed Loop

The outer speed loop is modelled by a PI speed controller, the inner current loop and the mechanical plant linking the current, torque and rotor speed. Since the current loop is tuned to be ten times faster than the outer speed loop, the current controller, time delay and the electrical machine model is approximated with a first order system with a time constant of  $\tau_c$ . From figure 3.10(b), the time constant is approximately 0.72 ms. Since the bandwidth of the current loop is chosen to be ten times larger than that of the speed loop, the time delay will not have much influence in the speed loop. Furthermore, since the time delay is included in the approximation of the first order current loop, this first order system approximation is assumed to be an accurate representation of the full closed loop transfer function of the inner current loop. The outer speed loop can be seen in figure 3.11.

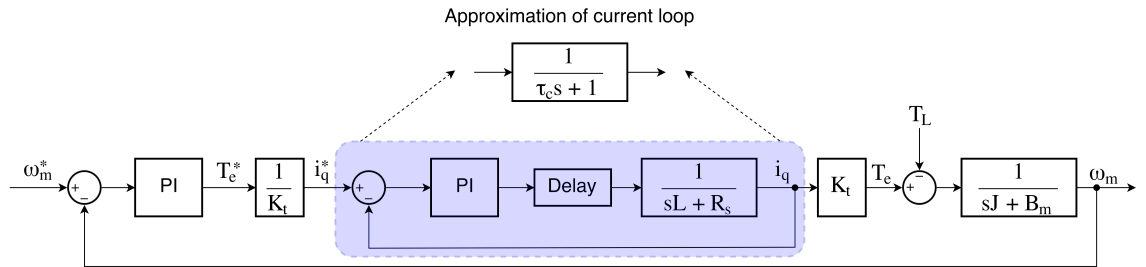


Figure 3.11: Block diagram of speed loop including a PI controller, a first order approximation of the inner current loop and the mechanical plant.

Here it can be seen, that the current output  $i_q$  is multiplied with the torque constant to get the torque. The load torque and Coulomb friction is included as a disturbance. The remaining torque is then fed into the mechanical machine model and the rotor speed is feed back to the speed controller. The open loop transfer function including controller, approximation of current loop and the mechanical model is

$$G_{p,s} = \frac{K_{p,s}s + K_{i,s}}{s} \frac{1}{\tau_c s + 1} \frac{1}{Js + B},$$

where subscript s denotes speed loop, which is used to distinguish between transfer functions of the current and speed loop. It is defined that

$$K = \frac{1}{J}, \quad T_c = \frac{K_{i,s}}{K_{p,s}}, \quad T_m = \frac{B_m}{J}.$$

This results in the following open loop transfer function

$$G_{ol,s} = \frac{s + T_c}{s/K_{p,s}} \frac{K}{s + T_m} \frac{1}{s + 1/\tau_c},$$

where  $T_c$  is the controller zero and  $T_m$  is the pole of the mechanical plant model. If the controller zero is set to cancel the slowest pole, the system will become faster and be reduced to a second order system. This is done by setting

$$T_c = T_m \Rightarrow \frac{K_{i,s}}{K_{p,s}} = \frac{B_m}{J},$$

which reduces the open loop transfer function to

$$G_{ol,s} = \frac{K}{\frac{1}{K_{p,s}}s^2 + \frac{1}{\tau_c}s} = \frac{1}{\frac{J}{K_{p,s}}s^2 + \frac{J}{\tau_c}s}.$$

The proportional gain is chosen such that the desired bandwidth is obtained. One way to do this, is to increase or decrease the magnitude curve of the open loop Bode plot. The magnitude of the open loop transfer function at the desired bandwidth is found to be  $M$ . An initial guess of the proportional gain is then

$$K_{p,s} = \frac{1}{10^{\frac{M}{20}}}.$$

Since the bandwidth of the closed loop transfer function may not be the same as where the open loop gain crosses zero dB, the value of  $K_{p,s}$  has to be validated from the closed loop Bode plot. Using the closed loop Bode plot, the proportional gain resulting in a desired bandwidth (frequency at -3 dB) was found to be 3.8. This resulted in an integral gain of 0.41. The open loop transfer function including this controller has a phase margin of 79.7°. A step response of the speed controller is shown in figure 3.12. From this, the machine will be able to e.g. accelerate from zero to a given speed in approximately 12 ms. This might be destructive for the machine and not possible for the inverter to output the needed current, so often in practise, the rate of the machine speed is limited to avoid inverter over-current.

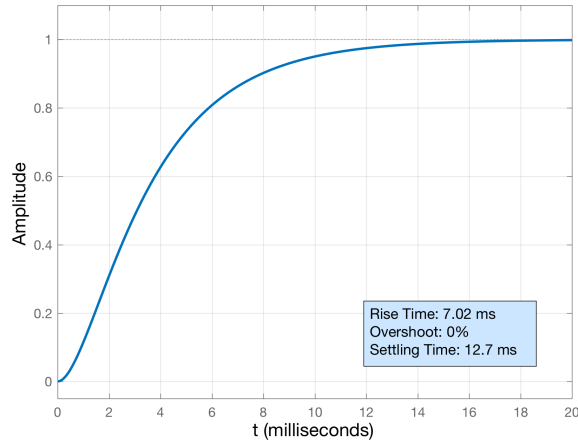


Figure 3.12: Step response of speed loop controller in continuous time.  
 $K_{p,s} = 3.8$  and  $K_{i,s} = 0.41$

### 3.2.2 Discrete Time Controllers

The discrete time controllers including time delay will in this subsection be designed for both the current and speed loop. Both the current and speed controllers are designed on the method where the controller zero is placed such that it cancels the pole of the plant transfer function. At last, a step response showing the behaviour of the controllers is shown.

#### Discrete Controller for Inner Current Loop

As for the continuous case, the block diagram consists of a discrete time controller, a time delay and the plant. As discussed earlier in this section, a unit delay is used to model the time delay since the plant is delayed half a sampling period when proceeded with a

ZOH. The discrete time PI controller is taken from the continuous domain to the discrete domain using backward Euler and can be expressed as

$$G_c(z) = K_{p,c} + \frac{K_{i,c}T_s z}{z - 1} = \frac{z - \frac{K_{p,c}}{K_{p,c} + K_{i,c}T_s}}{\frac{z - 1}{K_{p,c} + K_{i,c}T_s}}.$$

The plant including a unit delay is

$$G_p(z) = \frac{K}{az} \frac{1 - e^{-aT_s}}{z - e^{-aT_s}},$$

where again  $a = R_s/L$  and  $K = 1/L$ . Again the controller zero is placed to cancel the pole of the plant. This gives that

$$\frac{K_{p,c}}{\tau_z} = \frac{K_{p,c}}{K_{p,c} + K_{i,c}T_s} = e^{-aT_s},$$

where  $\tau_z = K_{p,c} + K_{i,c}T_s$ . The open loop transfer function reduces to

$$G_{ol,c}(z) = \frac{\tau_z K (1 - e^{-aT_s})}{a(z - 1)}.$$

Then  $\tau_z$  is selected such that the closed loop bandwidth is 500 Hz. The proportional and integral gains are then calculated as

$$K_{p,c} = \tau_z e^{-aT_s} \quad \text{and} \quad K_{i,c} = \frac{\tau_z - K_{p,c}}{T_s}.$$

Based on these equations, the proportional and integral gain when  $f_{sw}$  is 5 kHz is found to be  $K_{p,c} = 7.967$  and  $K_{i,c} = 1664$ . This is close to the gains found for the continuous case since the sampling period is rather small. The step response can be seen in figure 3.13, where it can be seen that the response has an overshoot of only 0.925%. Hence the controller is able to achieve a faster rise time and settling time with an increase in overshoot. Since small discrepancies will always exist between the modelled system and the physical system, this retuning is done on the physical setup where the values found in this section will act as a starting point.

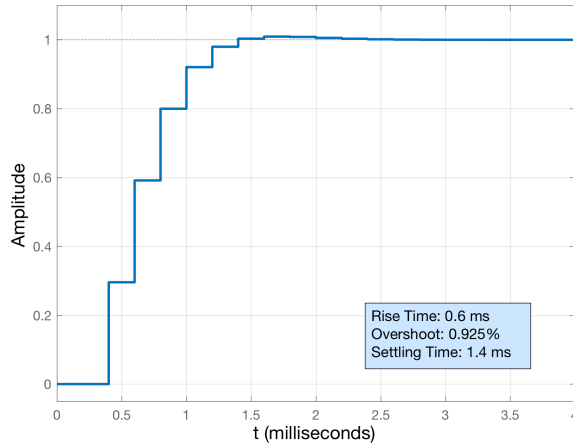


Figure 3.13: Step response of inner current controller in discrete time.  $K_{p,c} = 7.967$  and  $K_{i,c} = 1664$ . Sampling frequency is 5 kHz.

### Discrete Controller for Outer Speed Loop

The block diagram of the outer speed loop is equivalent to the continuous case and is shown in figure 3.11. Taking the approximation of the current loop, the PI controller and the mechanical plant into the discrete domain, the open loop transfer function becomes

$$G_{ol,s}(z) = \frac{z - \frac{K_{p,s}}{K_{p,s} + K_{i,s}T_s}}{\frac{z-1}{K_{p,s} + K_{i,s}T_s}} \frac{z}{z\left(1 + \frac{\tau_c}{T_s}\right) - \frac{\tau_c}{T_s}} \frac{\left(1 - e^{-\frac{B_m}{J}T_s}\right)}{B_m\left(z - e^{-\frac{B_m}{J}T_s}\right)}.$$

As for the continuous case, the controller zero is set to cancel the pole of the plant. This gives that

$$\frac{K_{p,s}}{\tau_z} = \frac{K_{p,s}}{K_{p,s} + K_{i,s}T_s} = e^{-\frac{B_m}{J}T_s},$$

which leads to the reduced open loop transfer function

$$G_{ol,s}(z) = \frac{\tau_z\left(1 - e^{-\frac{B_m}{J}T_s}\right)}{B_m(z-1)} \frac{z}{z\left(1 + \frac{\tau_c}{T_s}\right) - \frac{\tau_c}{T_s}}$$

As done for the discrete time current controller,  $\tau_z$  is selected to give the desired bandwidth (50 Hz), and the proportional and integral gains are calculated as described in the previous paragraph when the switching frequency is 5 kHz. The time constant of the inner current loop approximation is found from the step response of the current loop, which is approximately the same as for the continuous case (0.72 ms). This results in the following controller gains,  $K_{p,s} = 3.8$  and  $K_{i,s} = 0.41$ , which is exactly the same as is in the continuous case. This is also expected since the sampling frequency has much less effect on the speed loop compared to the faster current loop. The step response of the discrete speed controller can be seen in figure 3.14. The open loop transfer function including this controller has a phase margin of 78.4°.

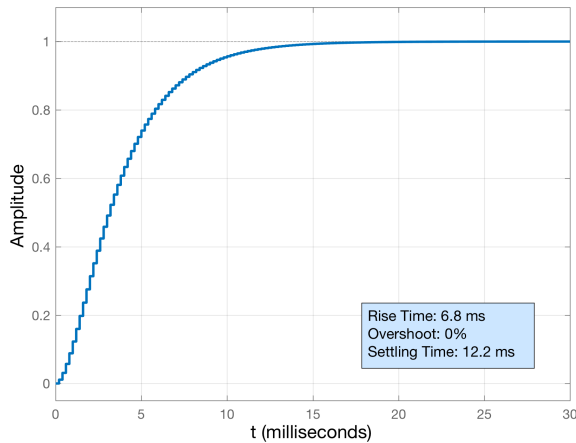


Figure 3.14: Step response of speed controller in discrete time.  $K_{p,s} = 3.8$  and  $K_{i,s} = 0.41$ . Sampling frequency is 5 kHz.

### 3.3 Stability Analysis

To better understand which parameters influence the stability of a system, an analytical form is often desired. This form is a trade-off between complexity and accuracy. If the

model of the physical system is complex, the analytical expression might be so complicated that no useful properties can be concluded from it. Therefore an analytical expression for system stability will in this section be given both in continuous and discrete time with maximum model accuracy where the analytical expression can still be useful.

### Routh-Hurwitz' Stability Criterion

A well known technique to evaluate information about the closed loop poles of a system and its stability without the inconvenience of solving for the poles is the Routh-Hurwitz stability criterion.

Routh-Hurwitz' stability criterion is tested on the continuous model of the physical system. The model consists of a PI controller, the first order electrical machine model and second order Padé approximation for the time delay. The characteristic equation is calculated as  $1 + T(s)$  where  $T(s)$  is the open loop gain. This gives

$$\begin{aligned} s^4 + \left( \frac{K_{p,c}}{L} + \frac{R_s}{L} + \frac{6}{T_d} \right) s^3 + \left( \frac{K_{p,c}R_s}{L^2} - \frac{6K_{p,c}}{LT_d} + \frac{6R_s}{LT_d} + \frac{12}{T_d^2} \right) s^2 \\ + \left( \frac{12K_{p,c}}{LT_d^2} - \frac{6K_{p,c}R_s}{L^2T_d} + \frac{12R_s}{LT_d^2} \right) s + \frac{12K_{p,c}R_s}{L^2T_d^2} = 0. \end{aligned}$$

The analysis and Routh array is derived and explained in detail in appendix C.1.

Using Routh's test, the sufficient condition for stability is that all elements in the first column of the Routh array are positive. To achieve that, it is found that  $T_d < 1.05ms$ , which corresponds to a sampling frequency of approximately 1430 Hz. This is based on the physical machine parameters and the current controller parameters obtained in section 3.2.1. The Routh-Hurwitz analysis is also verified through simulation where an exact representation of the delay was used instead of the second order Padé approximation. This is also shown in appendix C.1.

### Jury's Stability Criterion

For the continuous case, the system is stable if all the closed loop poles are located in the Left Half Plane (LHP). In the discrete case, stable poles from the continuous domain are mapped to the unit circle centred around the origin. This means that for a stable system in the discrete time domain, the closed loop poles have to lie within the unit circle, thus Routh's test cannot be used to analyse stability of a discrete system. To analyse the stability of a discrete system, Jury's stability criteria can be used [40]. The open loop transfer function of the discrete system consists of a unit time delay and the plant proceeded by a ZOH, which will give the exact time delay as described in section 3.2. The plant proceeded with a ZOH is now calculated. First the frequency domain expression of the plant is moved to the time domain as

$$\mathcal{L}^{-1} \left\{ \frac{G_p(s)}{s} \right\} = \mathcal{L}^{-1} \left\{ K \frac{1}{s(s+a)} \right\} = \frac{K(1-e^{-at})}{a}, \quad (3.3.1)$$

where  $K = 1/L$  and  $a = R/L$  for the current loop. Now taking the  $\mathcal{Z}$ -transform of the expression gives

$$\mathcal{Z} \left\{ \frac{G_p(s)}{s} \right\} = \mathcal{Z} \left\{ \frac{K}{a} (1 - e^{-aT_s}) \right\} = \frac{K}{a} \frac{z(1 - e^{-aT_s})}{(z-1)(z - e^{-aT_s})}.$$

Using that the  $\mathcal{Z}$ -transform of  $1/s$  is  $z/(z - 1)$  (used to cancel the added  $1/s$  in equation 3.3.1), the discretised plant becomes

$$G_p(z) = \frac{z - 1}{z} \frac{K}{a} \frac{z(1 - e^{-aT_s})}{(z - 1)(z - e^{-aT_s})} = \frac{K}{a} \frac{1 - e^{-aT_s}}{z - e^{-aT_s}}. \quad (3.3.2)$$

Using the discretised plant, a unit delay and a discrete time PI controller, the characteristic equation is

$$\begin{aligned} F(z) &= z^3 - (1 + e^{-aT_s})z^2 + \left( \frac{K}{a}(K_{p,c} + K_{i,c}T_s)(1 - e^{-aT_s}) + e^{-aT_s} \right) z \\ &\quad - \frac{KK_{p,c}}{a} (1 - e^{-aT_s}) = 0. \end{aligned}$$

It is shown in appendix C.2, that for stability

$$1.47K_{p,c}|1 - e^{-123.64T_s}| < 1. \quad (3.3.3)$$

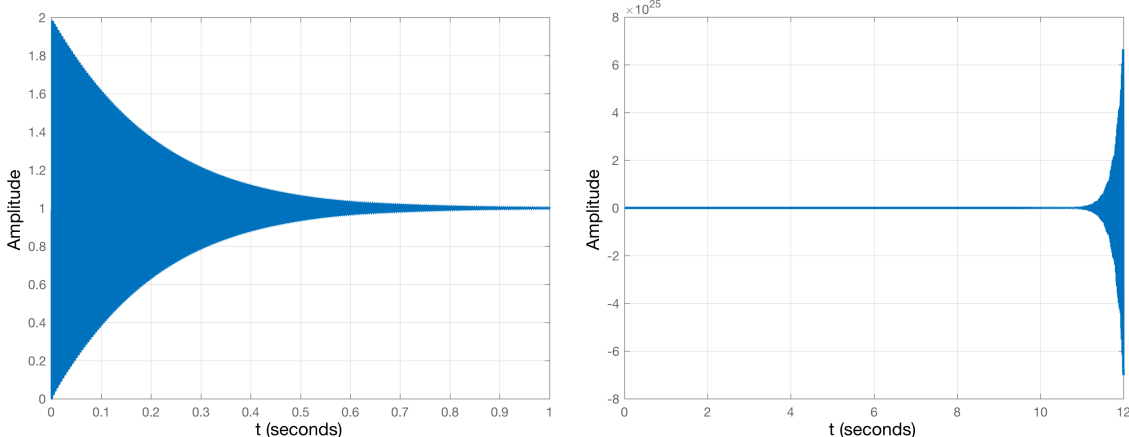
It is noticed that if  $0 < K_{p,c} < 1$ , the system can be made more robust for larger values of  $T_s$ . However, this might not be desirable for reason regarding the controller requirements. Furthermore it is shown that to ensure stability

$$|2.163K_{p,c}^2q_1^2 - 1| > \left| 1.47q_1K_{p,c}\left(1 + \frac{K_{i,c}T_s}{K_{p,c}} - q_2\right) + q_2 - 1 \right|, \quad (3.3.4)$$

where

$$q_1 = 1 - e^{-123.64T_s} \quad \text{and} \quad q_2 = 1 + e^{-123.64T_s}.$$

Thus, when the controller is designed, the values of  $K_{p,c}$  and  $K_{i,c}$  can be used to see at what values of the sampling time, the system is stable.



(a) A stable step response when the sampling frequency is 1550 Hz. (b) An unstable step response when the sampling frequency is 1530 Hz.

Figure 3.15: Simulated unit step response of system to verify the analysis done using Jury's test derived in appendix C.2.

Using equation 3.3.3 and 3.3.4 and the controller parameters for the discrete current controller ( $K_{p,c} = 7.967$  and  $K_{i,c} = 1664$ ), one can obtain that to ensure stability  $T_s < 0.72$  ms which corresponds to a sampling frequency of 1385 Hz. From the Routh-Hurwitz

stability test the stability boundary was found to be 1430 Hz. Normally, when using a discrete model the system will not be able to maintain stability to a lower sampling frequency. Therefore this is tested in simulation to see if the stability boundary is actually at 1385 Hz. The simulation results can be seen in figure 3.15(a) and 3.15(b), where it is shown, as expected, that the stability boundary is at a higher sampling frequency for the discrete case.

As the result results from Jury's test is based on approximations and simplifications on the system this could explain the slightly wrong value of the stability boundary. Furthermore this analysis only takes into account the PMSM without any interaction of the inverter and load machine, which could possibly increase the robustness of the system. However both Routh-Hurwitz' test and Jury's test has analytically proven that time delay can cause a system to become unstable and is able to predict an approximate frequency where it happens.

### 3.4 Simulation of FOC

overpicTo verify the controllers designed in the previous sections, a simulation model is build in Simulink. A schematic of this model can be seen in figure 3.16. The FOC is generated similarly to figure 3.1. In fact, the structure of figure 3.16 is the same as that of figure 3.1, but without considering SVM and the inverter. The PMSM in figure 3.1 is replaced with the machine equations. Equations 2.1.1 and 2.1.2 is written on integral form to isolate  $i_d$  and  $i_q$  to avoid numerical differentiation.

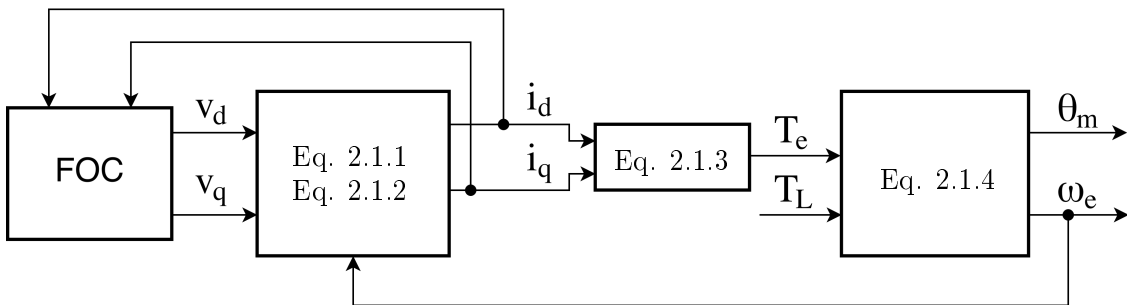


Figure 3.16: Schematic of the machine model and FOC implemented in Simulink.

To make the simulation resemble the physical setup as close as possible, a part of the model is run as to mimic the discrete controller and another part of the model is run to mimic the continuous behaviour of the physical machine. The model structure can be seen in figure 3.17. As can be seen, the model is run at two different sample frequencies. The machine model is sampled very fast to simulate the continuous behaviour of the machine in the laboratory, whereas the controller part of the model is run with the sampling period of  $T_s$ . A pulse generator is used to trigger and execute the controller part of the model every  $T_s$ . The sampled values from the plant is used together with the reference values for the  $d$ -axis current and the speed of the rotor to calculate the  $dq$ -axis voltage values. The influence of the inverter is not modelled and therefore all model variables are kept in the  $dq$ -reference frame. The PWM delay of  $0.5T_s$  is modelled as a transport delay in the continuous system. A unit delay is added to the  $dq$ -axis voltage values to simulate the

behaviour of the µC. This gives effectively a time delay of  $1.5T_s$  as desired. In the analysis done for the tuning of PI controllers, a unit delay and a plant proceeded with a ZOH was found to effectively give a delay of  $1.5T_s$ . However it is seen from the physical setup, that a time delay of  $1.5T_s$  is present in the system while at the same time, the plant is proceeded with a ZOH from the Digital to Analog Converter (DAC). This gives effectively a time delay of around  $2T_s$  and not  $1.5T_s$  as previously assumed. Therefore in order to make the simulation model resemble the physical setup, a unit delay of  $T_s$ , a PWM delay of  $0.5T_s$  and the effect of the plant being proceeded with a ZOH has to be included.

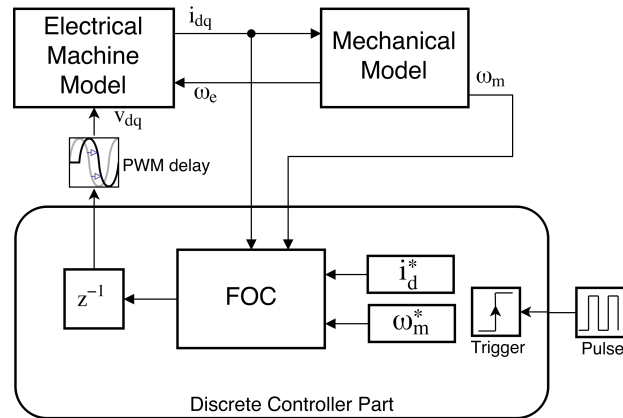


Figure 3.17: Structure of simulink model where the controller part is run in discrete time and machine part is run in "continuous" time.

When implementing the controllers including time delay, as was described in previous sections, no focus has been on the control effort of the controller. In reality, the system will not be able to respond to any commanded value and hence, when designing controllers this should be considered. When implementing the speed controller, to achieve the desired rise time of approximately 7 ms, the commanded  $q$ -axis current was simulated to be 2500 A, which is definitely not possible in the physical system. This means that the controller will not be able to work properly in the laboratory due to physical limitations. The control effort of the current controllers showed to be fine regarding laboratory limitations. To include this non-linearity of the system in the controller, saturation and integral wind-up is discussed.

### Antiwindup of Integral Term

In any physical system limitations exists. This could be on e.g. maximum output voltage of the VSI, maximum machine current and maximum speed of the machine. Therefore a controller either has to be designed such that these limits are never violated or its output has to be saturated to the limits if it happens. When the controller output is saturated, the operation of the controller becomes nonlinear since a change in the controller output does not change the output of the system.

One problem encountered when a controller is saturated is regarding the integral action of the PI controller. The action from the integrator becomes very large, since it keeps integrating the error between the commanded value and the saturated output. This is

called integration windup, which is an undesired effect of the control loop that can cause big overshoots and oscillations if not compensated. A common way to compensate this effect, is by the antiwindup technique called back-calculation. Here another feedback path is introduced after the controller output. If the controller is saturated, the integral action is reduced through the gain  $K_a$ .  $K_a$  is usually set to  $1/K_p$  [44]. Sometimes, if a simple antiwindup technique is used, or the value of  $K_a$  is not satisfactory, the integral action can simply be bypassed when the controller is saturated. This is also referred to as integrator clamping. The back-calculation method with a PI controller can be seen in figure 3.18, where the inner current loop is taken as an example.

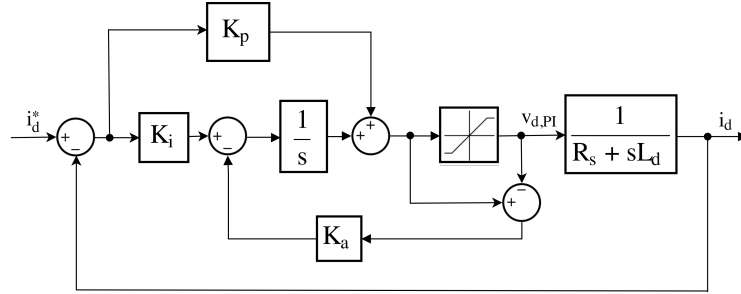


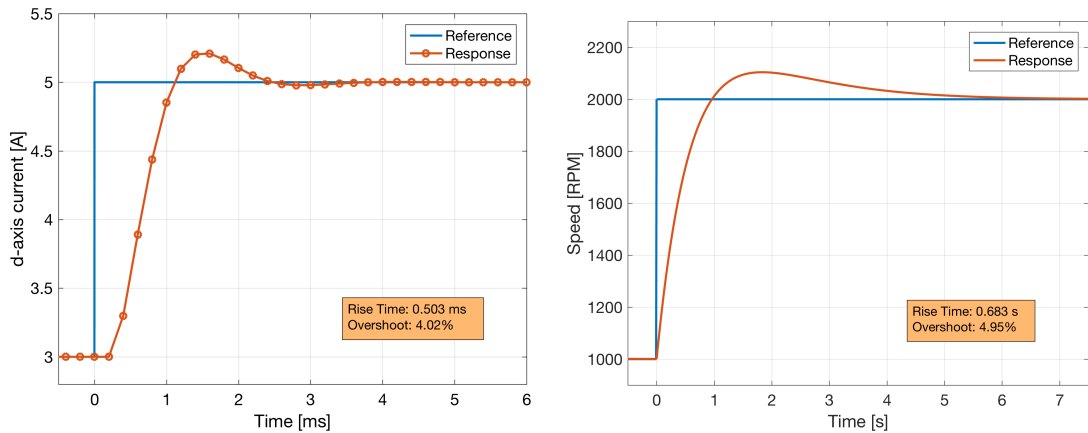
Figure 3.18: Back-calculation as antiwindup technique on the PI controller for the inner current loop. For a discrete simulation the integrator is substituted with a discrete time integrator.

The maximum allowed values for the physical setup used in the saturation blocks are

- Maximum  $q$ -axis current command is 25 A.
- Maximum torque command is 14 Nm to leave a margin on the inverter current.
- Maximum  $dq$ -axis voltage command is set to 300 V.
- Maximum rotor speed is set to 4500 RPM.

## Simulation Results

Using the physical limitations discussed above, with the saturation blocks, the speed



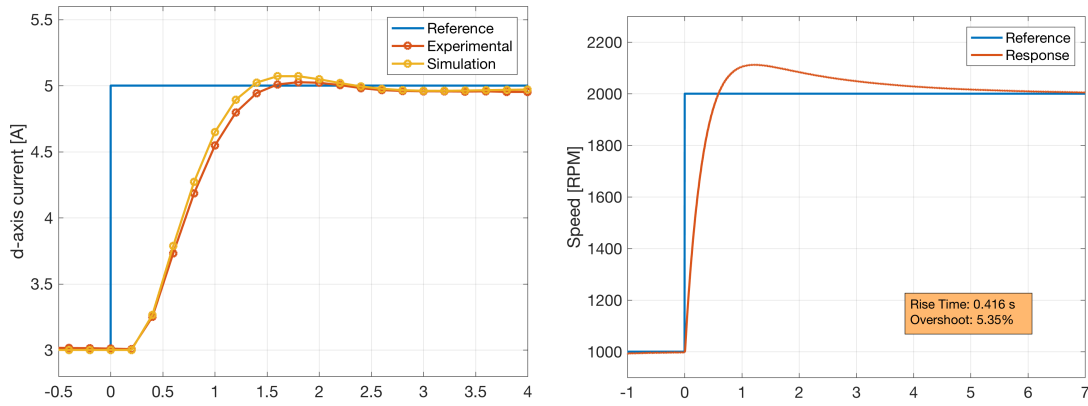
- (a) Simulated step response of  $i_d$  current from 3 A to 5 A.  $K_{p,c} = 7.967$  and  $K_{i,c} = 1664$ .
- (b) Simulated step response of reference speed from 1000 RPM to 2000 RPM.  $K_{p,s} = 0.007$  and  $K_{i,s} = 0.004$ .

Figure 3.19: Simulated step response of current and speed using FOC.

controller is retuned to achieve a commanded current that is obtainable. The proportional and integral gains were iteratively found to be  $K_{p,s} = 0.007$  and  $K_{i,s} = 0.004$ , which resulted in a maximum commanded  $q$ -axis current of approximately 20 A. Using this retuned discrete speed controller and the previously tuned discrete current controller together with the Simulink model structure shown in figure 3.17, the controllers can be tested in simulation. This is shown in figure 3.19(a) and 3.19(b). Here it can be seen that the tuned controller for the current loop gives an overshoot which is higher than the allowed. Therefore the current controller is retuned to comply with requirements. Through iteration the controller parameters for the current loop were found to be  $K_{p,c} = 7.1$  and  $K_{i,c} = 1250$ . The response using this controller is shown in the following section, where it is compared with the experimental response as well.

### 3.5 Laboratory Experiment of FOC

The controllers used in the simulation were implemented in the laboratory setup to test the performance of the system. Again, step responses in the  $d$ -axis current and the rotor speed were performed. The experimental results can be seen in figure 3.20. It can be noticed, that the current response resembles the simulated response well both when looking at the overshoot and rise time. The values for  $K_{p,c}$  and  $K_{i,c}$  are 7.1 and 1250 respectively as discussed in the previous section. It can be seen, that the simulated response shows slightly higher overshoot and a bit faster rising behaviour than the experimental. These differences could be caused by the idealised model of the inverter used in the simulation. It could also be caused by inductance and resistance values not being correct at the applied current levels and operating temperature present during the experiment. The difference is however very small and the model is thought to be acceptable. One thing to notice, is that the simulation is capable of predicting the same delay as seen in the laboratory. This again supports the discussion of using a time delay of  $1.5T_s$  together with the effect of the plant being proceeded with a ZOH.



(a) Experimental and simulated step response of  $d$ -axis current. Both responses have a settling time of approximately 7 ms.  $K_{p,c} = 7.1$  and  $K_{i,c} = 1250$ .

(b) Experimental step response of reference speed from 1000 RPM to 2000 RPM.  $K_{p,s} = 0.007$  and  $K_{i,s} = 0.004$ .

Figure 3.20: Experimental step response of current and speed using FOC.

For the speed response, the overshoot of the experimental results and the simulation is similar but the response seen experimentally is faster compared to simulation. This can be caused by discrepancies between the idealised simulation model and the physical system which allows a faster speed response.

Since the rotor speed cannot be allowed to change too fast due to limitations of inverter current, a limit on the change in rotor speed and hence the inverter current is introduced. The speed of the machine is limited depending on the rate change with a maximum rate change set to 2000 RPM/s. The speed controller is then retuned with  $K_{p,s} = 0.07$  and  $K_{i,s} = 0.05$ . The response of the setup with retuned speed controller can be seen in figure 3.21(a). Here it can be seen, that the speed response rises with almost same rate but without significant overshoot. Simulation and experimental results show similar performance. In figure 3.21(b), a zoomed view of the speed response can be seen. It is visible, that the simulation has a good prediction of the actual machine behaviour. Also the overshoot can be seen to be approximately 0.8%.

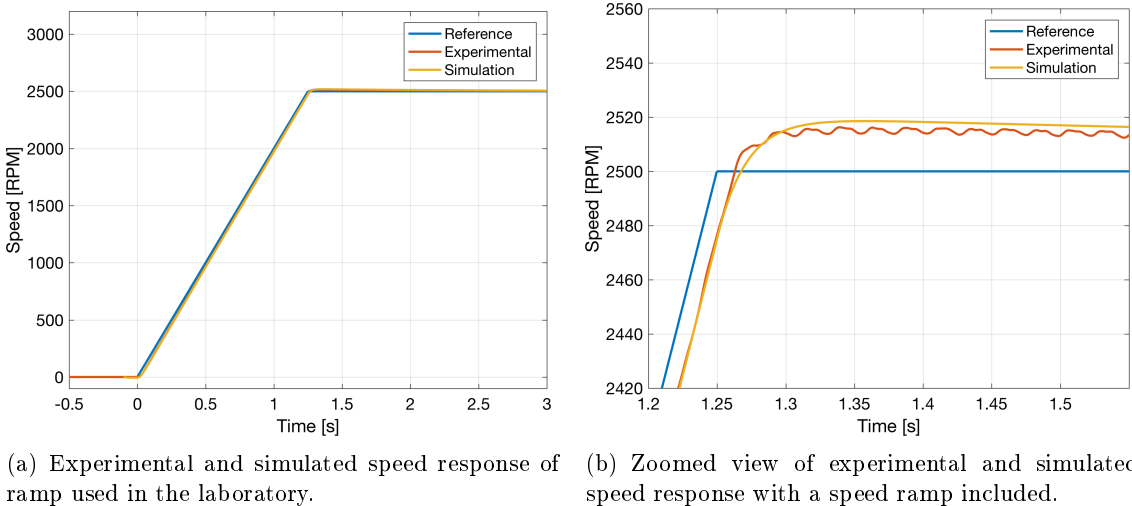


Figure 3.21: Laboratory and simulation results of speed controller with  $K_{p,s} = 0.07$  and  $K_{i,s} = 0.05$ .

### Inverter Voltage Error Compensation

The VSI used in the laboratory introduces complex and non-linear effects to the system due to inverter dead-time when switching the IGBTs and snubber capacitors in the gate drive circuit. These will cause errors that are dependent on inverter current. This implies, that when a voltage command is set in ControlDesk, a different voltage will be applied to the machine dependent on the operating condition of the machine. To compare simulation results with laboratory results, the voltage error caused by the inverter has to be known and compensated. In figure 3.22(a), the resulting  $d$ -axis current when  $\theta = 0$  for different voltage commands can be seen. Clearly a non-linear relationship between voltage and current due to the non-linearity of the inverter transistors exists. It is noticed that for currents above approximately 2.5 A, the relationship is linear. This linear part of the curve is used to evaluate the total resistance of the setup for one phase. This is found to

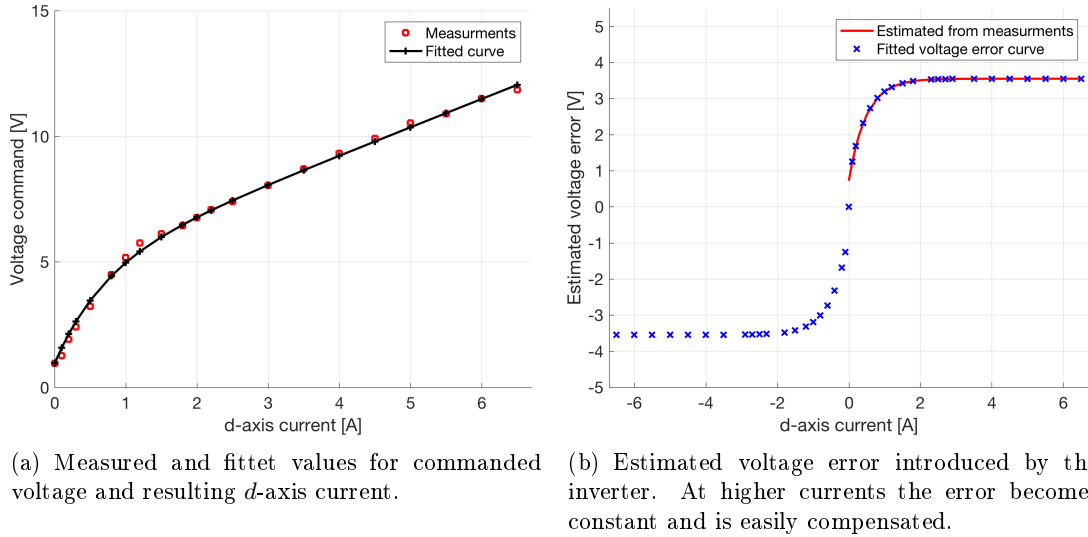


Figure 3.22: Estimation of voltage error introduced by the VSI.

be  $1.1253 \Omega$ , which was presented earlier in the system description section. A previously made MATLAB script, capable of estimating the inverter voltage error for measured sets of  $d$ -axis current and commanded voltage was provided by the supervisor of this project. The estimated voltage error for different current values can be seen in figure 3.22(b). Here it can be seen that as described before, the voltage error becomes constant for  $d$ -axis current above 2.5 A. This is the reason why the current steps presented is performed at values above 2.5 A. Here this constant voltage error is simply compensated in the setup to get results that are comparable with simulation results.

### Sampling frequency effects on system stability

Since the speed loop is not as sensitive to the used sampling frequency compared to the

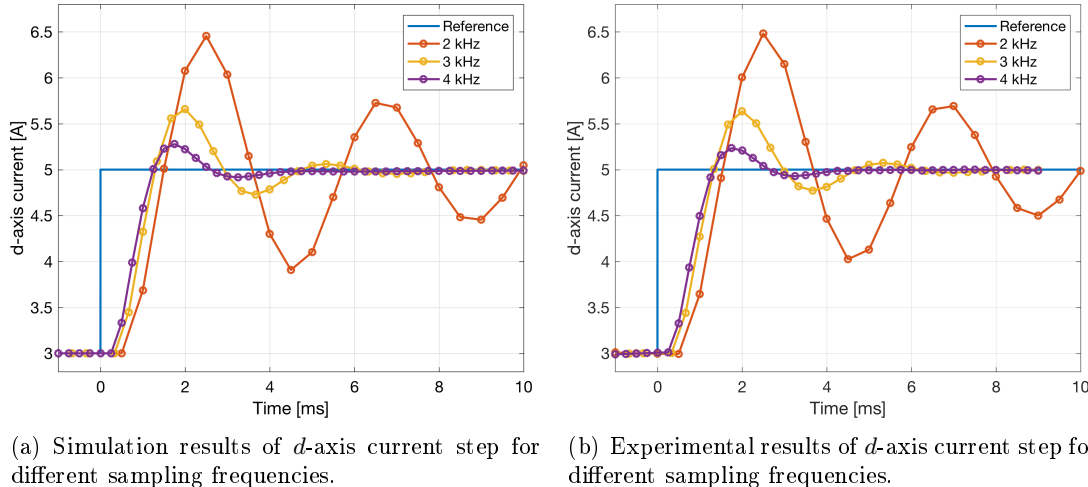


Figure 3.23: Effects on stability when reducing the sampling frequency.

current loop, only result from the current response will be used to see the behaviour in controller stability for a decreasing sampling frequency. Simulation results of this can be

seen in figure 3.23(a). Here it is evident, that by increasing the sampling frequency, the system becomes less stable. In figure 3.23(b), the same test is done in the laboratory. Here the same behaviour is evident with an almost indistinguishable response compared to simulation. For both cases, it is clearly seen, that decreasing the switching frequency degrades the stability of the system.

### 3.6 Discussion of Controllers

Since the machine is desired to be tested at decreasing frequency-modulation ratios, the switching frequency of the inverter has to be set accordingly. From the stability analysis done, it was shown that stability problems might occur at frequencies below approximately 1500 Hz. Therefore to have some margin a considered switching frequency of 2 kHz will be used. If the switching frequency is set to 2 kHz, then at 3000 RPM, the frequency-modulation ratio will be 10 and when the machine operates at 600 RPM the frequency-modulation ratio will be 50. Hence, by using a switching frequency of 2 kHz and run the machine between 600-3000 RPM a wide range of frequency-modulation ratios can be tested. Thus, a switching frequency of 2 kHz seems reasonable to avoid changing the switching frequency multiple times. This however means, that the time delay will increase with a factor of 2.5, which heavily influences the controller performance. Already when the switching frequency is lowered to around 4 kHz, it becomes impossible to have a phase margin of  $63.5^\circ$  and a bandwidth of 500 Hz in the closed loop current response using only a PI controller. Either the requirements have to be violated, which means to slow down the system performance, or another control strategy has to be introduced. For instance, if the switching frequency is set to 2 kHz and the overshoot requirement is kept, a maximum bandwidth of the current loop of approximately 200 Hz is achievable. This is achieved by manually retuning the controller iteratively.

The main problem when time delay increases, is that the decrease in phase for both open loop and closed loop will happen at lower frequencies. This implies, that when the proportional gain is selected to get a desired bandwidth, the phase margin is either too low to achieve the desired overshoot or in the case of a large time delay so low that the system will be unstable. To improve the phase when the time delay increases, e.g. for a lower switching frequency, a lead term could be introduced to the controller, which could increase the phase in a desired frequency range. This can also be achieved by introducing a derivative term in the PI controller. Using this approach, the switching frequency can be reduced, but not significantly since it only introduces a phase shift of maximum  $90^\circ$ , which at some point will not be enough, and it will be impossible to fulfil controller requirements or perhaps ensure system stability. Therefore a better approach is to investigate the opportunity of removing the problem by compensating the time delay. How to compensate time delay will be described in the following chapter.



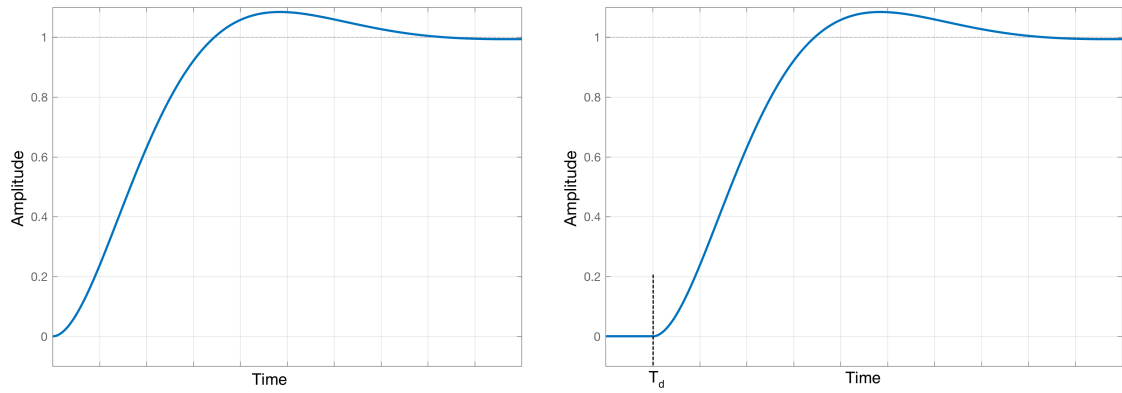
# 4

# Time Delay Compensation

As presented in the previous chapter, the stability of FOC is significantly decreased when the time delay is increased. To mitigate this problem and improve the stability of the setup, control strategies capable of compensating the time delay has to be introduced. This chapter will be devoted to this and it includes a derivation of the SP together with simulation and experimental test of this control strategy. Tests of stability and bandwidth of system will be compared to FOC, with and without load. Since the SP depends on machine parameters, a sensitivity analysis regarding these will be given and different control approaches trying to eliminate the need for these are developed and tested.

## 4.1 The Smith Predictor

If a controller is designed, using classical methods, to control a delay-free system, a unit step response could look like that in figure 4.1(a). Figure 4.1(b) shows the same step response, but shifted in time by  $T_d$ . Smith's principal says, that if the response of a delay-free design satisfies the design criteria (e.g. figure 4.1(a)), then the response in the delayed case should be exactly the same but shifted by  $T_d$  (figure 4.1(b)) [45].



(a) Example of a desired response of a system in a delay-free case. (b) Desired response of a system with a time delay. This is exactly a time shifted version of (a).

Figure 4.1: Visualisation of Smith's principle, which says that the desired response of a system including a delay, is exactly that of the delay-free case shifted in time [45].

Smith's principal can be used to derive what is known as Smith's method or the Smith predictor. Assume that a feedback system without delay can be written as

$$T(s) = \frac{G_c(s)G(s)}{1 + G_c(s)G(s)}.$$

This could give a response similar to figure 4.1(a). Obviously the response of figure 4.1(b) can then be obtained by

$$T(s) = \frac{G_c(s)G(s)}{1 + G_c(s)G(s)} e^{-T_{ds}}. \quad (4.1.1)$$

If it is assumed that this transfer function is achievable, the controller  $G_c^*(s)$  is modified and a block diagram similar to that of figure 4.2(a) can be obtained. The closed loop transfer function of this is

$$T(s) = \frac{G_c^*(s)G(s)e^{-T_{ds}}}{1 + G_c^*(s)G(s)e^{-T_{ds}}}. \quad (4.1.2)$$

Smith's principle now yields

$$\frac{G_c^*(s)G(s)e^{-T_{ds}}}{1 + G_c^*(s)G(s)e^{-T_{ds}}} = \frac{G_c(s)G(s)}{1 + G_c(s)G(s)} e^{-T_{ds}}$$

solving for  $G_c^*(s)$  gives

$$G_c^*(s) = \frac{G_c(s)}{1 + G_c(s)G(s)[1 - e^{-T_{ds}}]}. \quad (4.1.3)$$

The block diagram of this controller is seen in figure 4.2(b). Here  $G_c(s)$  is the controller designed for the delay-free case,  $G(s)$  the delay-free part of the plant, and  $e^{-T_{ds}}$  is the time delay.

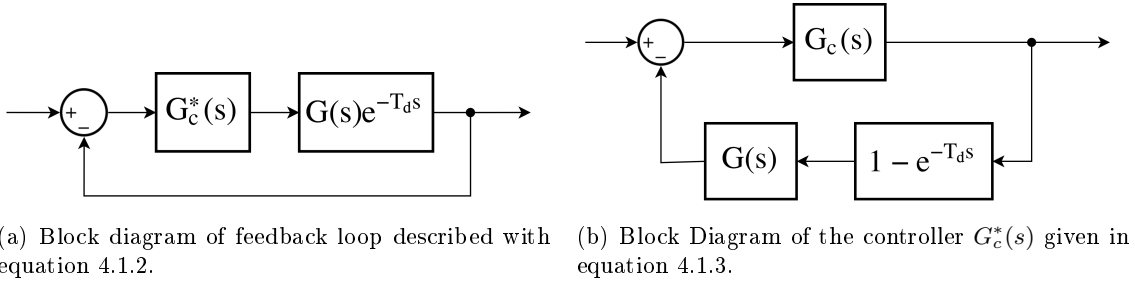


Figure 4.2: Block diagrams used in the derivation of the Smith predictor.

If it is possible to find a model for the delay-free part of the plant  $G_m(s)$  and a model of the delay  $G_{D,m}$ , then it is possible to design a controller in a delay-free case and then afterwards implementing  $G_c^*(s)$  (equation 4.1.3 and figure 4.2(b)) [45]. After substitution of  $G_c^*(s)$ , figure 4.2(b), into 4.2(a) and some rearrangement, the more familiar version of the Smith predictor, shown in figure 4.3, can be obtained. The input to output transfer function is given as [11]

$$T(s) = \frac{c(s)}{r(s)} = \frac{G_c(s)G(s)e^{-T_{ds}}}{1 + G_c(s)[G_m(s) + G_e(s)]} \quad (4.1.4)$$

where

$$G_e(s) = G(s)e^{-T_{ds}} - G_m(s)G_{D,m}.$$

If the model of the plant and the delay perfectly resembles the physical system,  $G_e(s) = 0$ . In this case, the signal at the point C of figure 4.3 is zero. When this is true, equation 4.1.4 reduces to equation 4.1.1 [11]. Furthermore the point B of figure 4.3 will be exactly the same as point A. These two facts could lead to an equivalent block

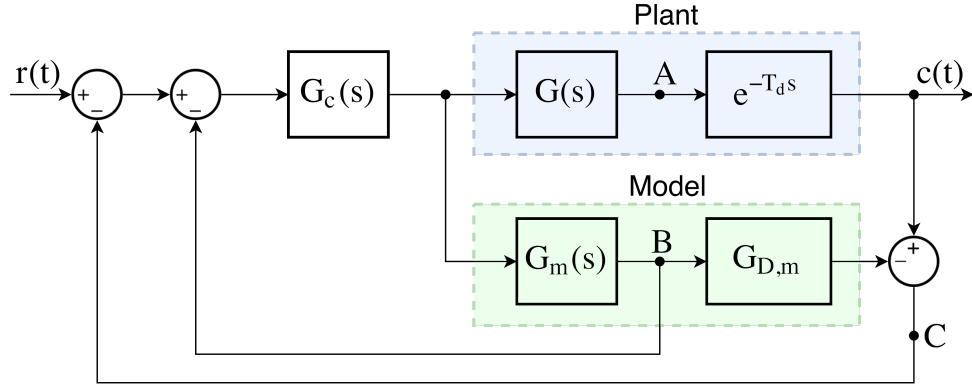


Figure 4.3: Block diagram of the SP [11].

diagram where the outer feedback loop is removed and the inner feedback is taken from point A instead of point B. Here no model of the plant and delay is needed resulting in the same response. However, generally the point A is inaccessible and the model part 'predicts' the behaviour of the physical delay-free plant (thus the name Smith predictor) and generates the point B. It is noticed that removal of the outer feedback loop, in case of a perfect model of the plant and delay, results in open loop control, which in general will not result in good performance, since in practise a perfect model is impossible to achieve [45]. In a later section, model mismatch in the Smith predictor is analysed to investigate this effect on system stability.

### Modified Smith Predictor

As described above, perfect modelling of the plant and delay will result in a signal with a value of zero at the point C in figure 4.3. In a practical case, measuring noise is almost unavoidable and will always be present in measurements. This noise will be transferred to the point C and the controller will try to compensate it. This is not desired since the noise is generated in the measuring system and might not be present in the plant. Therefore, the Smith predictor can be modified where a Low Pass Filter (LPF) is included in the outer feedback loop. This is done to remove high frequency noise and thus improve the performance of the controller. This technique is known as a Disturbance Observer (DO).

## 4.2 Implementation and Simulation of Smith Predictor

In this section, implementation and simulation of the Smith predictor is described. The simulation model is the same as shown earlier for FOC, but with inclusion of the Smith predictor model in the control strategy. To simulate the Smith predictor, a model of the plant has to be implemented. This is done in a MATLAB function, since this closely resembles the implementation on a Digital Signal Processor (DSP) and additionally it is easy to switch between different model cases. The decoupled electrical machine equations are used to predict the next current state using the measured  $dq$ -currents and the commanded  $dq$ -voltages from the PI controllers which is to be applied in the next switching period. This predictor using the decoupled machine model will be referred to as a MBP. Using a forward difference approximation for the time derivative, the decoupled

machine equation for the  $d$ -axis can be written as

$$v_{d,PI}(k) = R_s i_d(k) + L_d \frac{i_d(k+1) - i_d(k)}{T_s}$$

which gives that the next current state is

$$i_d(k+1) = \frac{(v_{d,PI}(k) - R_s i_d(k))T_s}{L_d} + i_d(k), \quad (4.2.1)$$

which is the current predicted to be at the point B of figure 4.3. The prediction for the  $q$ -axis current is simply obtained by substituting  $d$  with  $q$ . This current prediction is based on a continuous time model and its accuracy will be compared with a current predictor obtained from a discrete time transfer function of the plant. The transfer function of the plant proceeded by a ZOH is

$$\frac{i_d(z)}{v_{d,PI}(z)} = \frac{1 - e^{-\frac{R_s}{L_d} T_s}}{R_s z - R_s e^{-\frac{R_s}{L_d} T_s}},$$

which can be written as

$$i_d(z) \left( R_s - R_s z^{-1} e^{-\frac{R_s}{L_d} T_s} \right) = v_{d,PI}(z) \left( z^{-1} - z^{-1} e^{-\frac{R_s}{L_d} T_s} \right)$$

which taken into samples is

$$i_d(k) R_s - i_d(k-1) R_s e^{-\frac{R_s}{L_d} T_s} = v_{d,PI}(k-1) \left( 1 - e^{-\frac{R_s}{L_d} T_s} \right).$$

Moving all samples one step forward in time, the predicted current at time  $k+1$  can be calculated as

$$i_d(k+1) = \frac{v_{d,PI}(k) \left( 1 - e^{-\frac{R_s}{L_d} T_s} \right) + R_s i_d(k) e^{-\frac{R_s}{L_d} T_s}}{R_s}. \quad (4.2.2)$$

As before the  $q$ -axis prediction is obtained by replacing  $d$  with  $q$  in the equation, since the decoupled machine equations are used.

The time delay is approximated using the Thiran filter as described in section 3.2 with a time delay of  $1.5T_s$ . A second order Thiran filter can be used to model a time delay between one and two  $T_s$ , and is implemented as

$$\frac{i_{d,del}(z)}{i_d(z)} = \frac{a_0 z^{-2} + a_1 z^{-1} + a_2}{a_2 z^{-2} + a_1 z^{-1} + a_0},$$

which can be written as

$$i_d(z)(a_0 z^{-2} + a_1 z^{-1} + a_2) = i_{d,del}(z)(a_2 z^{-2} + a_1 z^{-1} + a_0).$$

Put into sample form and isolating the delayed current, one can get that

$$i_{d,del}(k) = \frac{a_0 i_d(k-2) + a_1 i_d(k-1) + a_2 i_d(k) - a_2 i_{d,del}(k-2) - a_1 i_{d,del}(k-1)}{a_0}, \quad (4.2.3)$$

where the Thiran coefficients ( $a_0$ ,  $a_1$ ,  $a_2$ ) can be found as described in section 3.2. The term  $i_d(k)$  in equation 4.2.3 is obtained at point B in figure 4.3. It corresponds to  $i_d(k+1)$

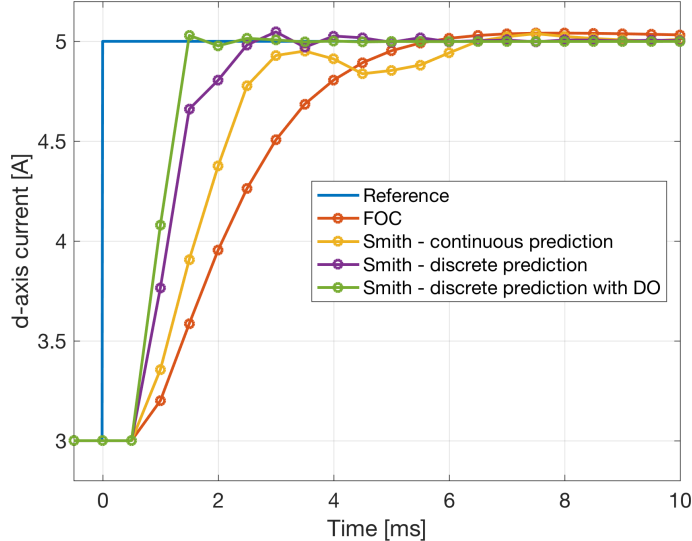


Figure 4.4: Simulated step response of  $d$ -axis current for FOC, the SP where a continuous model (equation 4.2.1) is used to predict the next current, the SP where a discrete model (equation 4.2.2) is used to predict the next current and the SP with the discrete model including a DO in the feedback path.

in equation 4.2.1 and 4.2.2.

The sampling frequency used in the simulation is 2 kHz. This is also the sampling frequency used through-out the remaining part of the project. The simulated results for FOC, the SP using a continuous model to predict  $dq$ -currents (equation 4.2.1) and the SP using a discrete model to predict  $dq$ -currents (equation 4.2.2) are shown in figure 4.4. Individual PI controllers are tuned to get optimal performance in each of the individual cases and the PI parameters used for the different figures can be found in appendix E. As can be seen, using the SP the bandwidth of the response can be increased compared to conventional FOC. For the continuous model this is true for the rise time of the response but the settling time is approximately the same as the response when using FOC, indicating mismatch between the model and the setup. Furthermore it is seen, that using the discrete model to predict the currents, a faster response can be obtained compared to the use of a continuous model for the prediction. This is in good agreement with the fact, that the discrete model is proceeded with a ZOH, which is exactly what the plant sees in both the physical system and in simulation due to the DAC. This means, that  $G(s)$  in the plant in figure 4.3, is modelled as a ZOH and the machine voltage equations. Therefore using the discrete model including the effect of the ZOH to predict the next values of  $dq$ -currents, the model of the plant is more accurate, hence a faster and better response.

As described for the MSP, a DO can be used in the feedback path to improve the response of the system. As can be seen in figure 4.4 the bandwidth of the system is increased and the current response is improved significantly when using a DO. The DO used is a LPF which can be represented by the following transfer function

$$DO(z) = \frac{z + 1}{z \left(1 + \frac{2}{T_s \omega_c}\right) + \left(1 - \frac{2}{T_s \omega_c}\right)},$$

where  $T_s$  is sampling period (0.5 ms) and ( $\omega_c$  [rad/s]) is the desired cut-off frequency of the filter. The cut-off frequency resulting in best simulated performance is 2 rad/s.

The responses shown in figure 4.4, are shown where mismatch between physical model and the model of plant is minimised as much as possible. From this, the discrete model (equation 4.2.2) with disturbance observer will be used when testing the Smith Predictor in the laboratory.

To see the improvement on bandwidth and system stability when adding a SP and a DO in the feedback path, closed loop bode diagrams are constructed for the SP with and without DO and for conventional FOC. These can be seen in figure 4.5. Here it is evident, that using a SP both the bandwidth and phase margin of the system can be increased. Conventional FOC without SP has a bandwidth of approximately 100 Hz, the SP without DO has a bandwidth of approximately 200 Hz and the SP with DO has a bandwidth reaching the Nyquist frequency, which in this case is 1000 Hz. Furthermore it can be seen that by introducing the SP, the phase is increased at higher frequencies which improves the system stability. It is also seen that the SP without DO, has a rapid increase in magnitude around 600 Hz. This is suspected to be due to the use of Thiran filter as an approximation for the time delay. The DO helps to dampen this peak, which also explains the improved response when including it in the feedback loop.

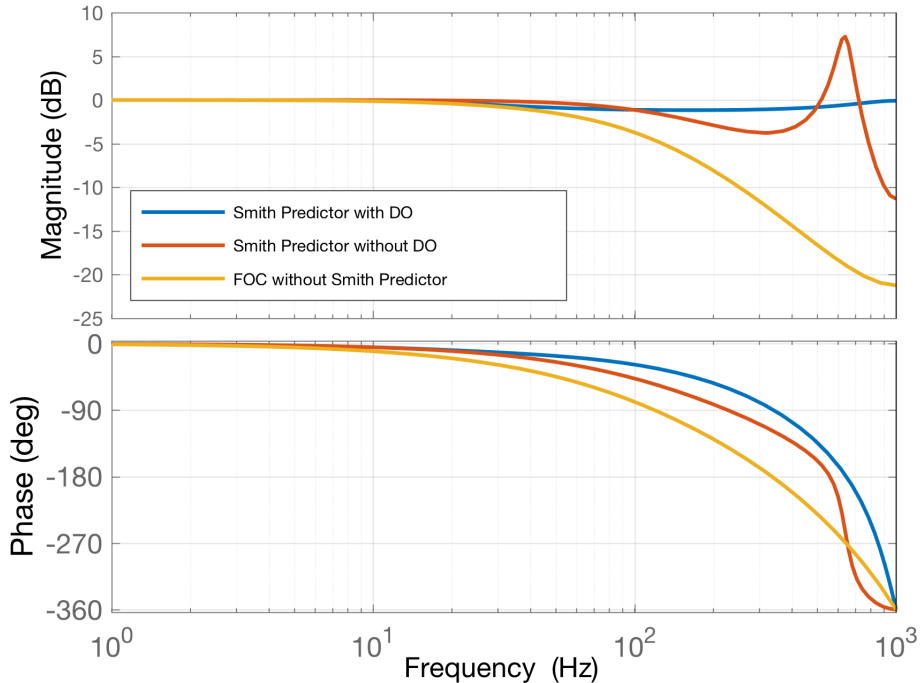


Figure 4.5: Bode diagram for SP with DO, without DO and conventional FOC.  
The PI parameters are as for figure 4.4.

### 4.3 Experimental Results of Smith Predictor

The implementation of the SP was discussed in section 4.2. It is implemented likewise in the laboratory. Similarly the sampling frequency is set to 2 kHz. Since the sampling frequency has been decreased, a new fit for the estimated voltage error caused by the in-

verter is made. This also resulted in a lower equivalent resistance of the setup due to lower switching losses. The resistance value of for the full setup at 2 kHz is found to be  $0.96 \Omega$ . This estimation is done as described in section 3.5, where the switching frequency was 5 kHz. The new resistance value is used in the SP for the current predictions. Individual controllers were tuned for the FOC response and SP response. This is done to show the best performance of the different control approaches. The controllers are tuned with the constrain of an overshoot less than 2% as described in the controller requirements and the bandwidth requirement is allowed to be violated. A  $d$ -axis current step from 3-5 A was done for both FOC and the SP. The optimal current controller for the FOC in the laboratory was almost identical to the controller used for simulation, which again supports the accuracy of the simulation model with the physical setup. The same applied to the current controller for the SP used in simulation and in the laboratory, which is also evident from the results to be presented. The experimental step response in  $d$ -axis current for FOC and SP with and without DO can be seen in figure 4.6. It can be seen that the Smith predictor is able to compensate time delay and improve bandwidth of the system also in the laboratory. Furthermore it can be seen, that the experimental response using the SP can be made faster by introducing a DO in the feedback path. A value of 120 rad/s as the cut-off frequency for the DO used in the laboratory was iteratively found give the best performance. This value of the cut-off frequency allowed for  $K_{i,c}$  to be increased to 3400 compared to 2500 in simulation. This iteration was only done for the step from 3-5 A, hence its validity for other current steps is unknown and should be revealed if commercially implemented.

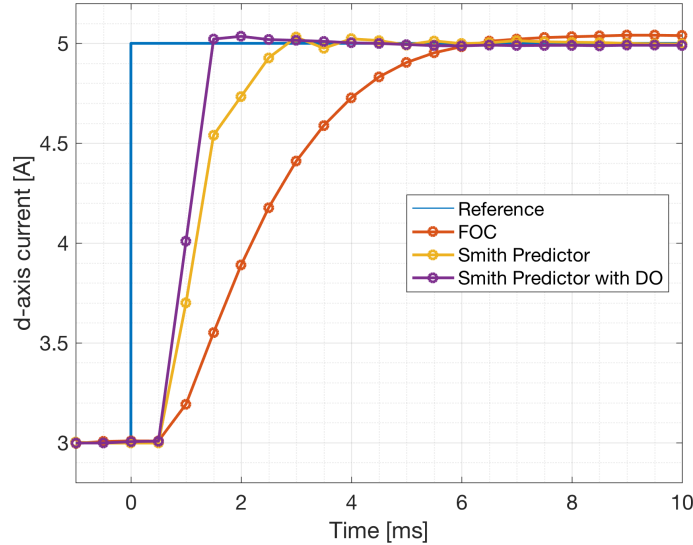


Figure 4.6: Comparison of  $d$ -axis experimental current steps of FOC, SP and SP with DO at a sampling frequency of 2 kHz.

To further validate the improvement of the SP compared to FOC, a step from conventional FOC to the SP with DO was done at a steady state rotor speed of 500 RPM and 1200 RPM, where each control approach (FOC and SP) used their own individual optimised PI controller, which can be found in appendix E. This means that when the control strategy was changed, so was the PI parameters for the current controllers. The response of phase currents,  $dq$ -axis currents and the rotor speed for 500 RPM and 1200 RPM can be seen in figure 4.7 and 4.8 respectively.

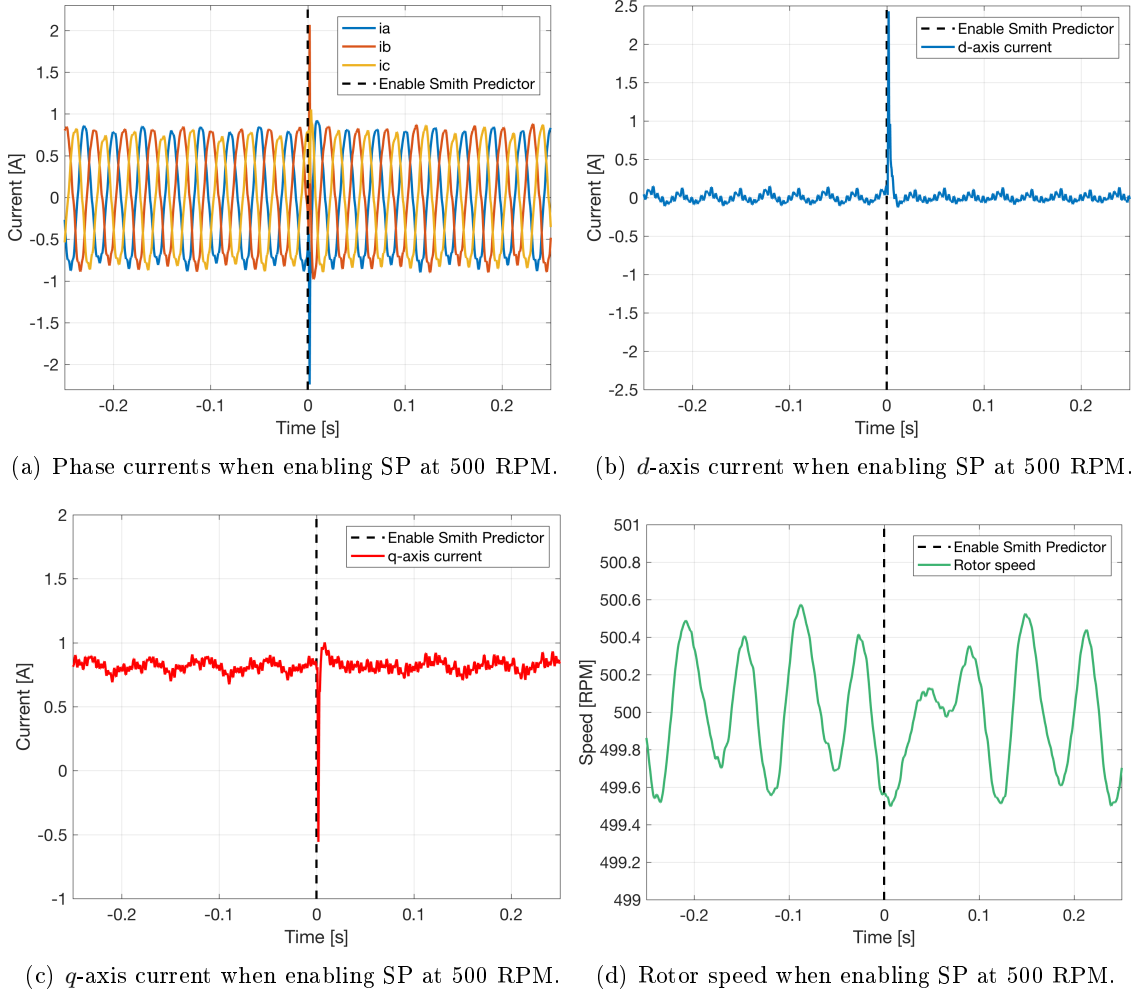


Figure 4.7: At a steady state speed of 500 RPM (33 Hz electrical frequency), the control approach was changed from FOC to SP. All results are from the experimental setup with a sampling frequency of 2 kHz. The results shown are for a no-load condition. The current controllers are tuned as in figure 4.6.

Here it can be noticed that at low speeds, in this case 500 RPM, the performance of FOC and SP are similar, where the SP gives tiny improvements regarding the ripple in the  $d$ -axis current. However when the steady state speed is increased to 1200 RPM, the difference between FOC and SP has become much more pronounced, and the system when controlled by FOC, is close to its boundary of stability.

To see when the different control strategies become unstable regarding frequency-modulation ratio, the rotor speed is ramped slowly from 1000 RPM to a point, where the system becomes unstable. This point is where the current rises above its maximum limits and the system is shut off either by external or software protection. The results of this test is shown in figure 4.9, where the speed reference uses a rate limiter of 10 RPM/s. As can be seen in figure 4.9, the system becomes unstable at 1280 RPM using FOC, at 1650 RPM using SP and at 2500 RPM using SP with DO. When the DO is included in the feedback path, the PI parameters can be tuned more aggressively without violating the overshoot constraint. These high PI parameters ( $K_{p,c} = 11$  and  $K_{i,c} = 3400$ ) makes the controller

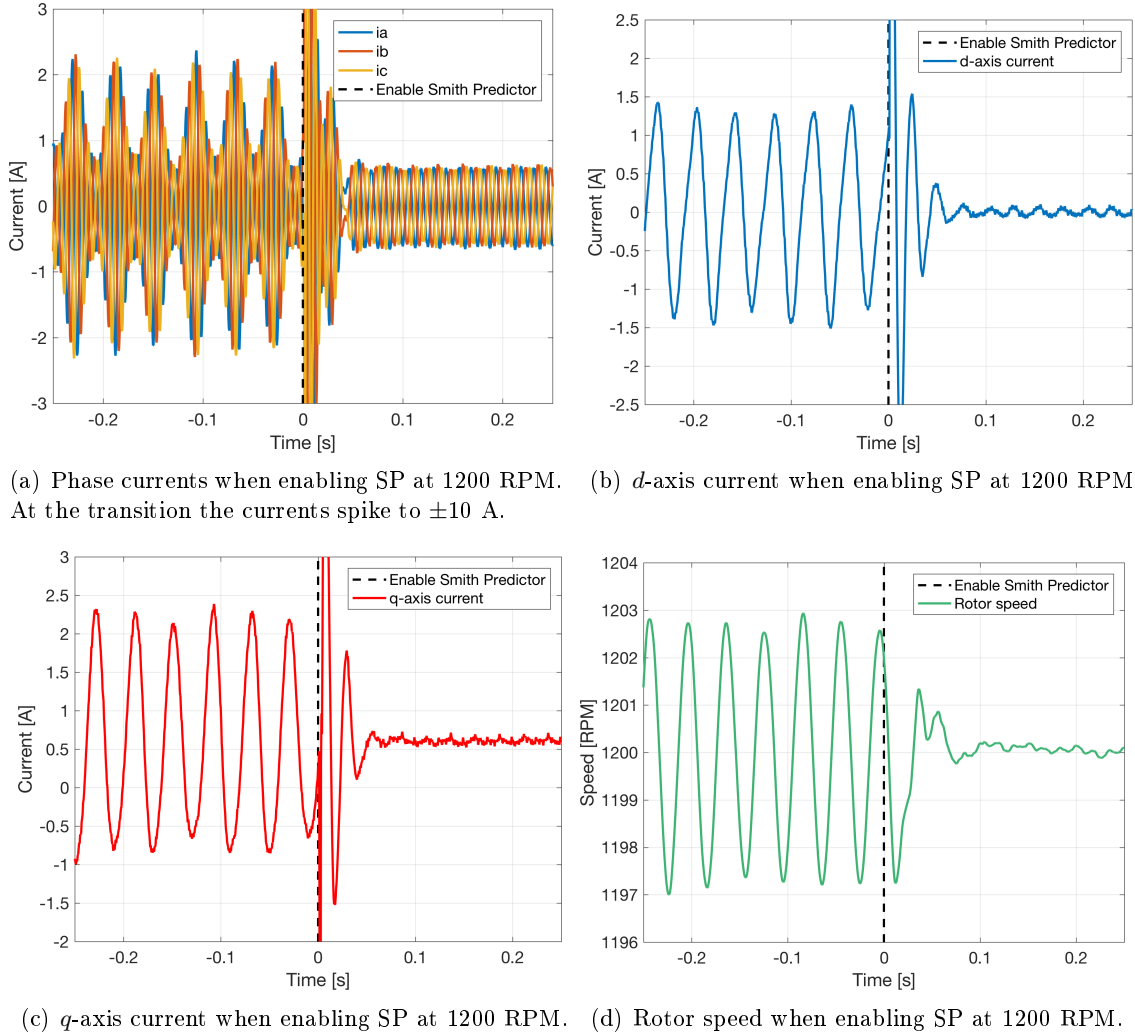


Figure 4.8: At a steady state speed of 1200 RPM (80 Hz electrical frequency), the control approach was changed from FOC to SP. All results are from the experimental setup with a sampling frequency of 2 kHz. The results shown are for a no-load condition. The current controllers are tuned as in figure 4.6.

able to ensure system stability at rotor speeds much higher than both FOC and the SP without DO. The overshoot requirements of the current controllers is however only tested at zero speed, which means that they do not necessarily comply with the requirements at load steps at high rotor speeds. This is a known fact that has to be further analysed if to be implemented in the industry or elsewhere. From the results presented in figure 4.9, the stability boundary for the frequency-modulation ratio for FOC is

$$m_{f,FOC} = \frac{2000\text{Hz}}{1280\text{RPM}/60 \cdot 4} = 23.44,$$

where 4 represents the number of pole pairs. The stability boundary for the frequency-modulation ratio for SP with DO is

$$m_{f,SP} = \frac{2000\text{Hz}}{2500/60 \cdot 4} = 12.$$

This means in this case, that by using the Smith predictor with DO instead of conventional FOC, the rotor speed can be increased with approximately 100% or the switching frequency

can for the same drive be halved. In the case of lower switching frequency the losses in the setup can be reduced significantly.

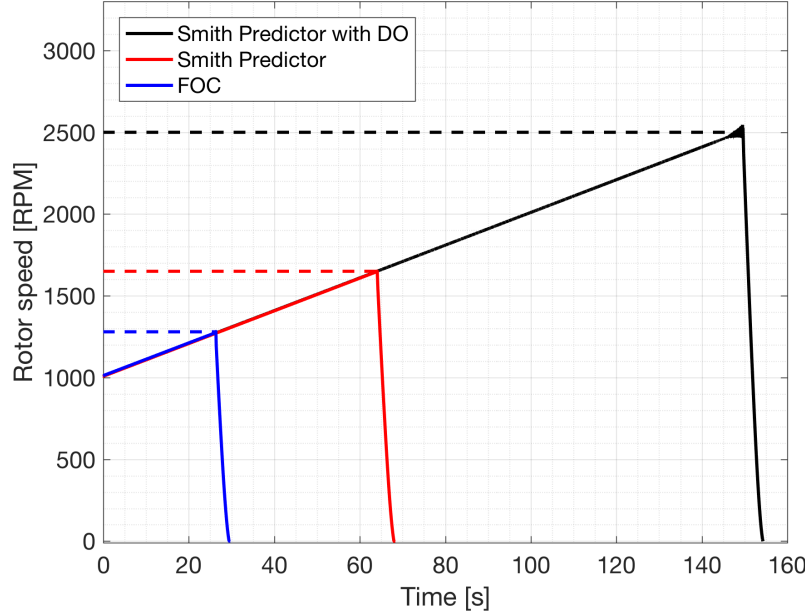


Figure 4.9: Experimental results from ramp of rotor speed using FOC and SP with and without DO. The rotor speed is slowly ramped using a rate limiter of 10 RPM/s to see at which speed, the control strategy becomes unstable. The controllers are tuned as the one used in figure 4.6.

### Load tests of FOC and Smith Predictor

The improvements observed when using SP compared to FOC is extended to the case of a loaded response and in particular, a load step during a steady state speed operation. To do so, the machine torque is stepped from zero to the rated torque of the machine (5.8 Nm). To step the load, an external three-phase power resistor is at the step point connected to the load machine. In order to achieve a torque step equal to the rated torque, the power dissipated by the power resistor has to be adjusted to that. Since the generated voltage of the load machine is quite low for low speeds (around 50 V at 1000 RPM), a variable-tap transformer is used to amplify the output voltage of the load machine, to a voltage level high enough to draw the desired current through the load resistor. The per phase load resistance used for all tests is  $60 \Omega$ . The transformer turns ratio is variable and is adjusted to get approximately same torque step for all the tests. In all cases, the current controllers were tuned as in figure 4.6. The speed controller is retuned with  $K_{i,s}$  increased to 0.8, to quickly regain the steady state speed after a load step.

In figure 4.10, a load step performed at 1000 RPM is done for FOC. As can be seen, FOC is able track the reference during a load step to rated torque. The operating speed can be seen to decrease during the step, but is quickly resettled to its reference value due to the increased integral value of the speed controller.

In figure 4.11, the same test is done but at an operating speed of 1100 RPM. Here it can be seen that FOC is no longer able to stabilise the system when loaded.

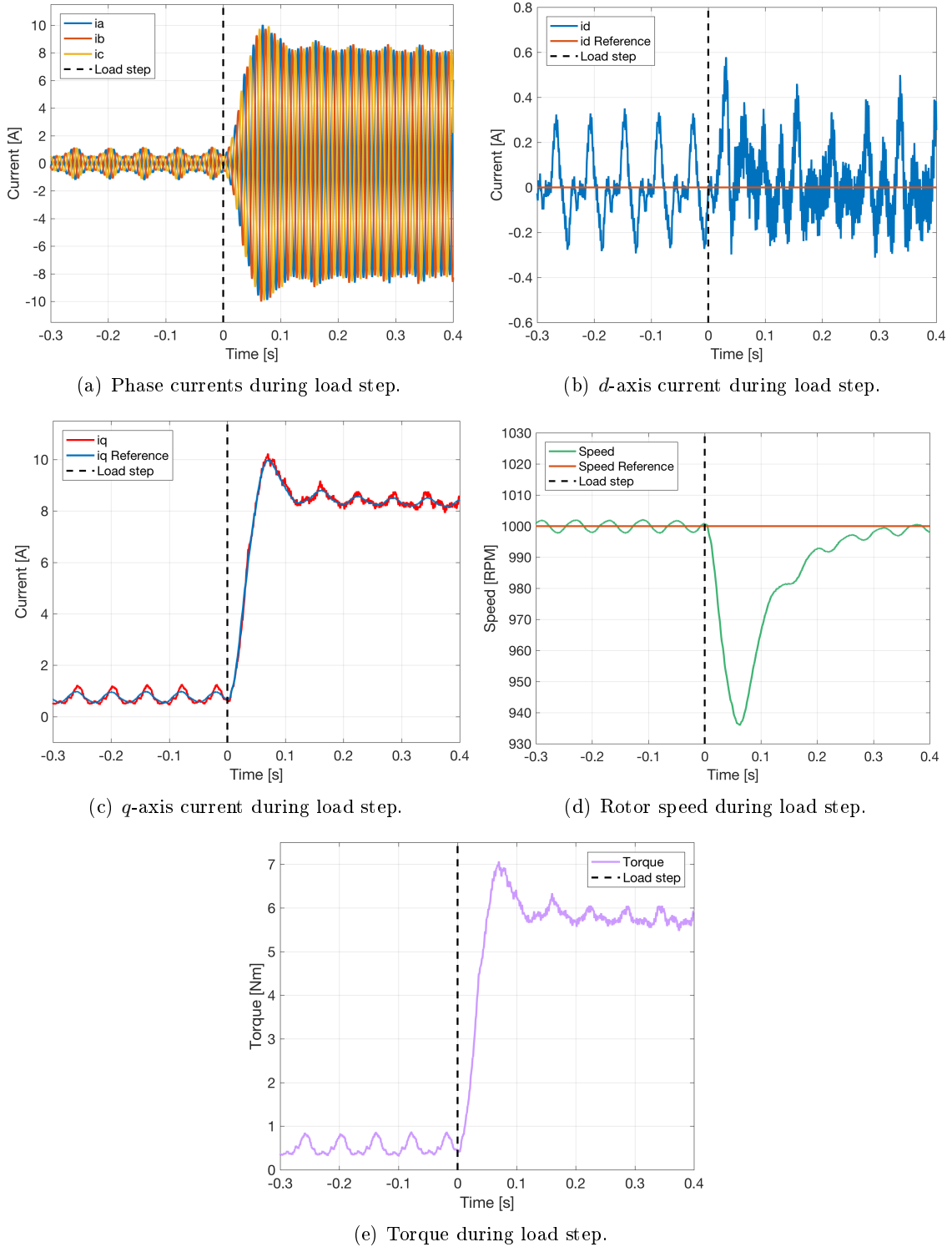


Figure 4.10: Load step at 1000 RPM using FOC. The sampling frequency of the system is 2 kHz.

In figure 4.12, the same test that destabilised the FOC controller is done for the SP with DO. Here it can be seen, that using the SP, the controller is able to track the reference when the load is stepped without any stability issues. An overshoot in the torque is evident, which is directly caused by the overshoot in  $q$ -axis current since these are propor-

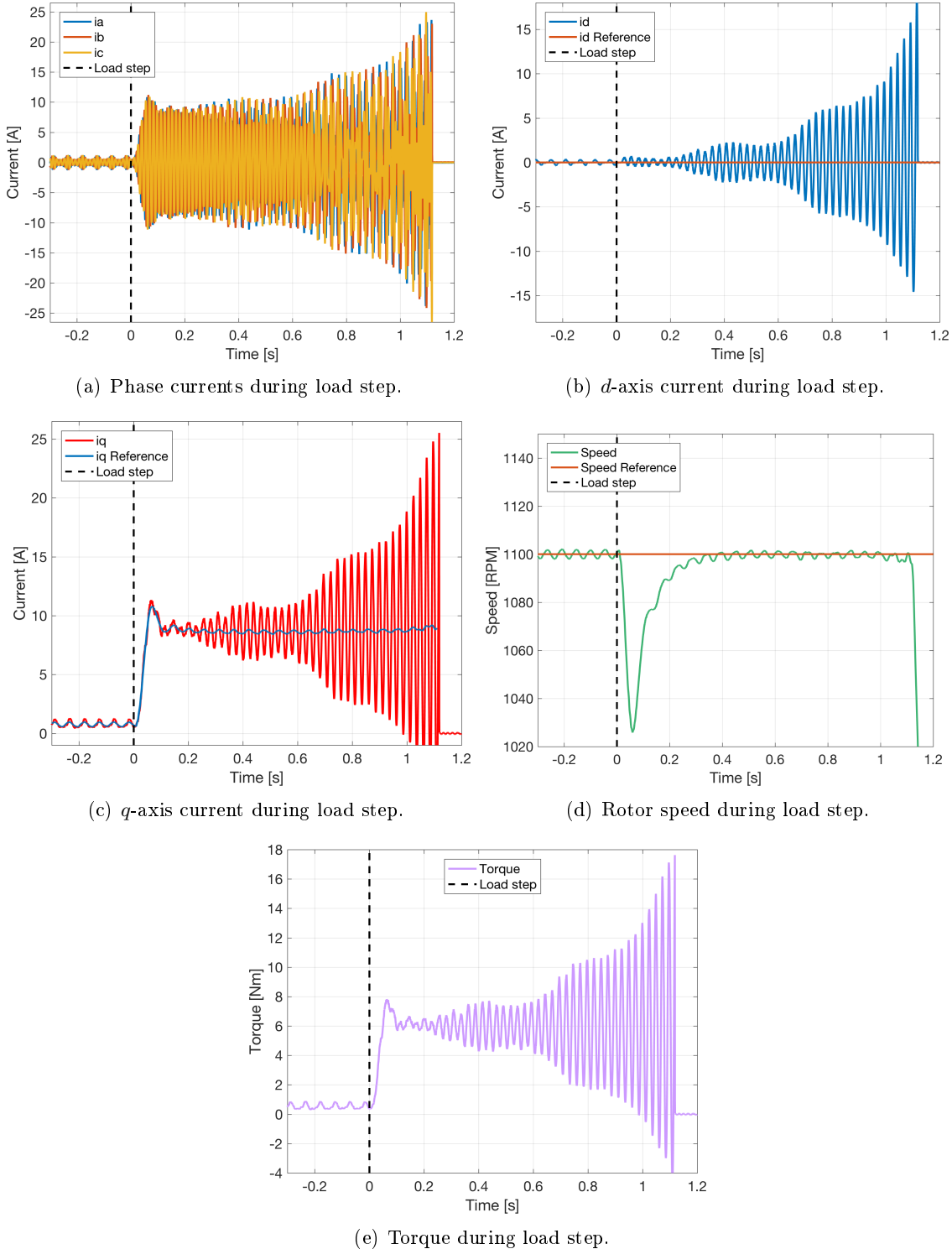


Figure 4.11: Load step at 1100 RPM using FOC which causes the system to become unstable. The sampling frequency of the system is 2 kHz.

tional to each other in the case of surface mounted PMs.

In figure 4.13, a load step to nominal torque is performed using the SP at 2000 RPM. Here it can be seen that the SP is still able to maintain a stable response, even though the

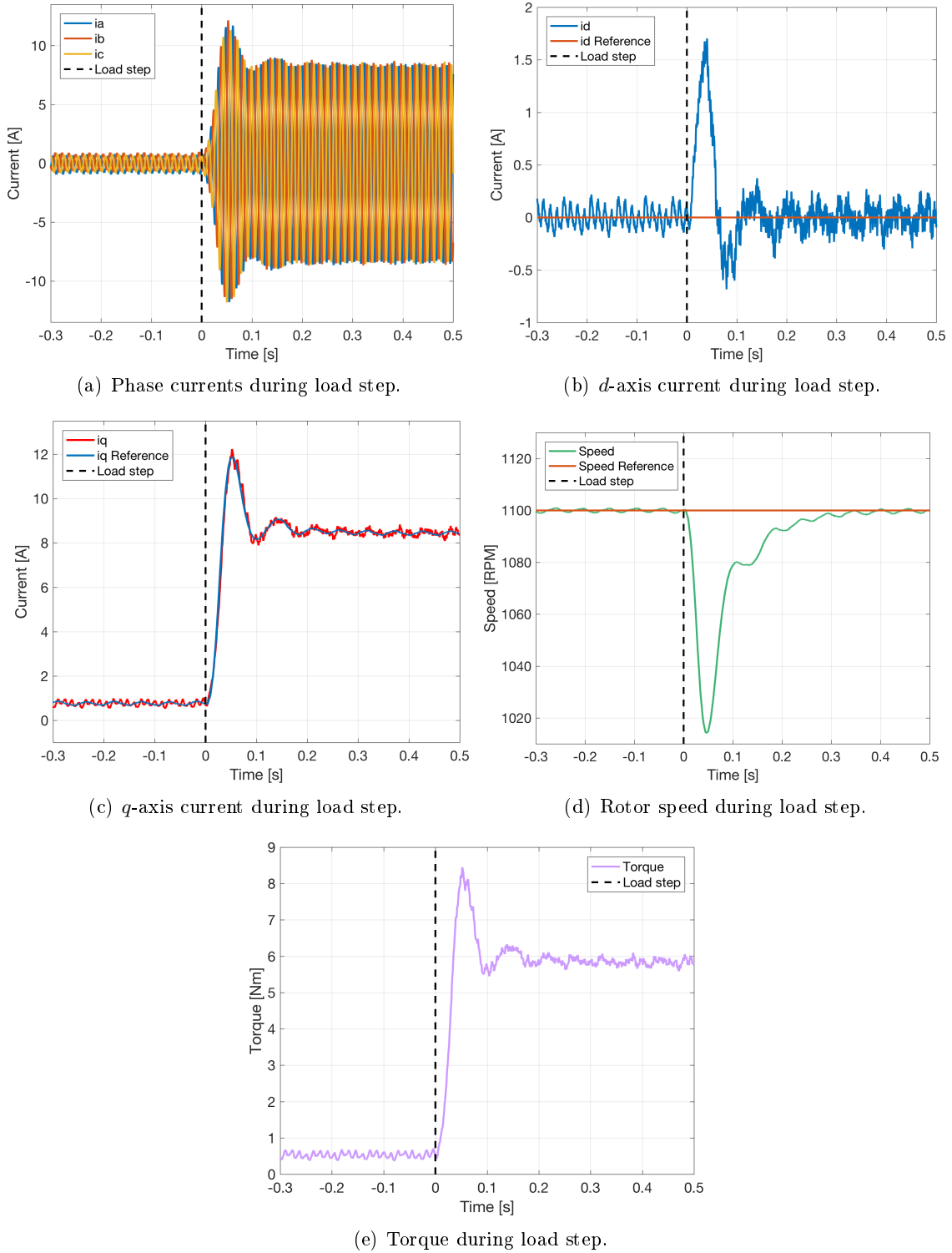


Figure 4.12: Load step at 1100 RPM using SP with DO. Using the Smith predictor, the response is improved significantly compared to FOC and remains stable after being loaded. The sampling frequency of the system is 2 kHz.

overshoot and ringing has increased significantly compared to the response shown for 1100 RPM. The same test was done for 2400 RPM. Here the SP could still produce a stable response but with sustained oscillations indicating that the operating speed was close to

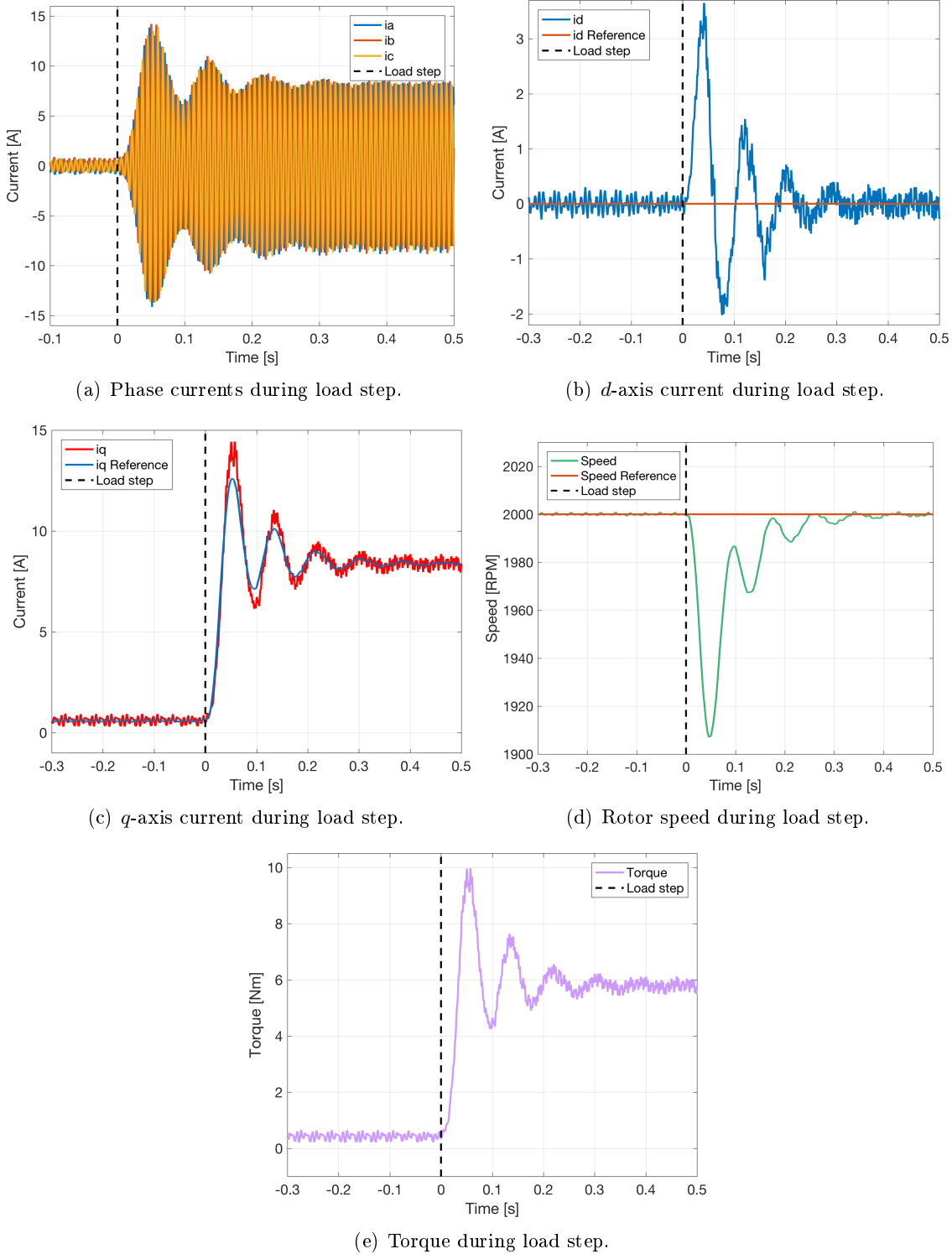


Figure 4.13: Load step at 2000 RPM using SP with DO. Higher overshoot and ringing starts to occur, but the controller still ensures a stable response. The sampling frequency of the system is 2 kHz.

the stability boundary of the system. This is in good agreement with the results shown in figure 4.9, where the SP with DO, enters the unstable region around 2500 RPM for a sampling frequency of 2 kHz.

By this, it is shown that the SP can offer superior performance compared to FOC with regards to risetime, stability and load changes when the frequency-modulation ratio is decreased. Even though the SP shows much improvement compared to FOC, oscillations are still present. Unavoidably sources of error in the experimental setup exist. These including measurement uncertainties and switching noise generated by the inverter, but any mismatch between the predicted plant and the physical plant will make the SP unable to fully compensate the delay. Furthermore the Thiran filter is an approximation to the real physical delay. Hence mismatch in machine parameters and time delay is a big drawback of the SP and the impact of parameter mismatch has to be understood in order to successfully implement the SP instead of FOC in a setup. The sensitivity of parameter mismatch will be discussed in the following section.

## 4.4 Parameter Sensitivity Analysis of the Smith Predictor

As described earlier, an accurate model of the plant is needed to make  $G_e(s)$  of equation 4.1.4 zero. In this section it is investigated what influence discrepancies between the model and the physical plant has on stability. It is assumed that the model parameters are kept constant, e.g. at datasheet values but at the same time the physical plant can have variable parameters as would be the case with change in temperature and saturation levels in the physical setup. The time delay is assumed to be constant and independent of time for a given setup. However it might be variable from setup to setup. To form a sensitivity analysis of the model parameters, a discrete time system is developed and simulated. The simulation is performed on the closed loop transfer function given by equation 4.1.4 moved to the  $z$ -domain. The plant and plant model is expressed as equation 3.3.2, the PI controller as equation C.2.1, and the physical delay and model of the time delay as a second order Thiran filter (equation 3.2.7). The controller gains are kept the same in all cases which is the controller used in simulation of the Smith predictor without a disturbance observer in the feedback path. These are  $K_p = 7.8$  and  $K_i = 1700$ .

In figure 4.14, step response plots are shown for various mismatches. From figure 4.14(a) it is seen that a model overestimation of 20% in the resistance will cause a high overshoot, whereas an underestimation will cause slow rise time. The same behaviour is seen with the inductance mismatch, shown in figure 4.14(b). The inductance has however a more significant influence on the response. Figure 4.14(c) shows mismatch of the time delay. It is clearly seen that an underestimation will cause a large overshoot which is also expected since the integrator of the PI controller will integrate the error caused by the delay. On the other hand, an overestimation causes oscillations and a slow settling time. Figure 4.14(d) shows a combination of mismatches. One being a worst case in overshoot with 20% overestimation of resistance and inductance combined with a underestimation of the time delay. The other being a worst case in rise time with 20% underestimation of resistance and inductance combined with a overestimation of the time delay. In either case it can be seen that if mismatch between the model of the plant and the actual plant exists, the performance of the SP is degraded which in extreme cases result in a response that is worse than or comparable to using FOC at a low sampling frequency.

One way to look at the stability for parameter variation is through step responses in

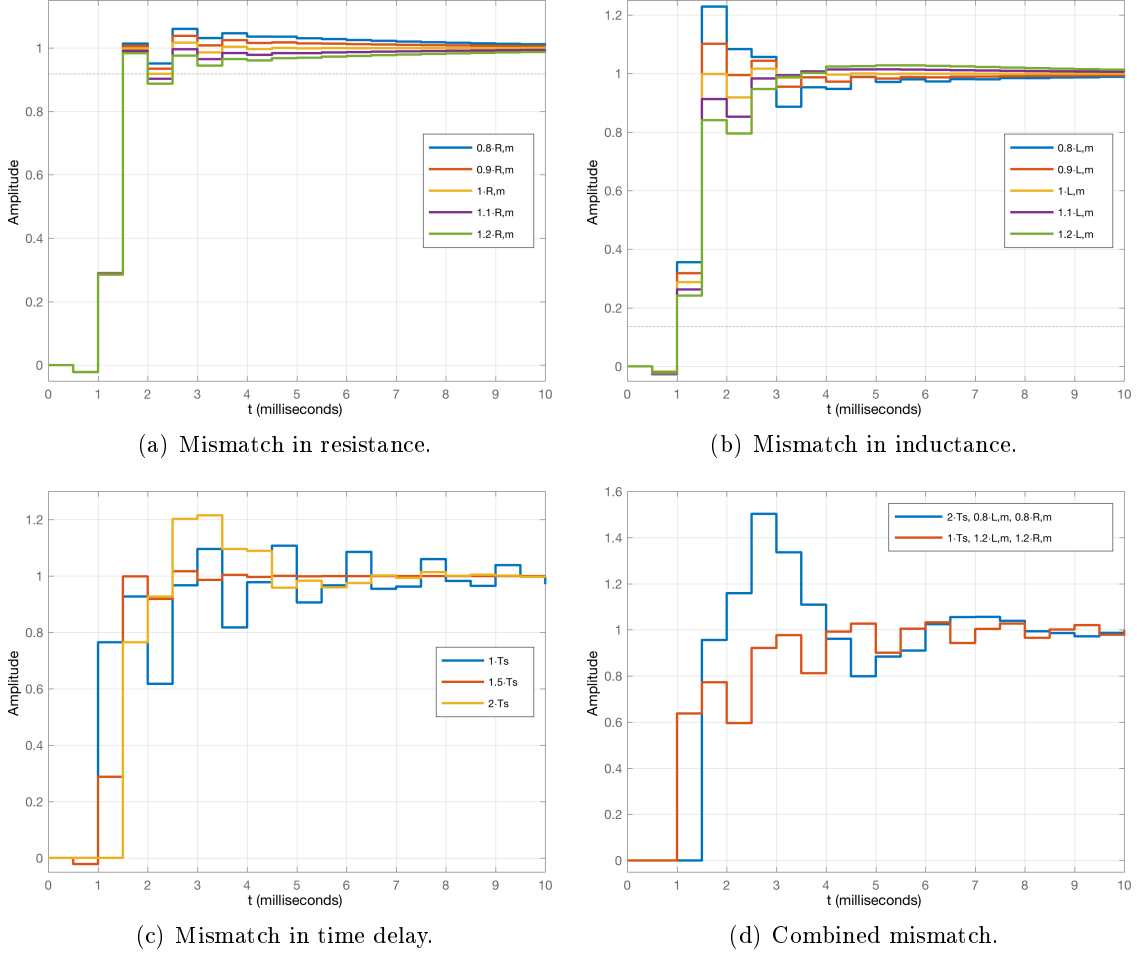


Figure 4.14: Comparison of various mismatches between the plant and the model used in the Smith predictor (figure 4.3). The results are simulated results at a sampling frequency of 2 kHz. In the plots, it is assumed that the modelled value is kept constant and the plant values are variable. This is done to resemble the physical case where temperature will change the resistance and saturation level will change the inductance value. The time delay is assumed to be constant when the same plant is used, but could be variable with different setups.

the time domain, which is shown above. However, it can be difficult to see underlying trends and predict how the response will behave for other mismatches. Hence sensitivity of parameter mismatch is analysed using pole-zero maps, where the location and more important the change in location of the system poles can be seen. The poles and zeros are plotted in the  $z$ -plane where lines for constant damping ratios and natural frequencies can be seen. Poles are denoted by crosses and zeros by circles. Figure 4.15 shows pole zero maps for different mismatches. The arrows indicates the movement of the poles as the plant values changes compared with the SP model values. In figure 4.15(a), a variation in the plant resistance is shown. It is seen that even with a variation in plant resistance from  $0.1R_m \rightarrow 2R_m$ , all poles are still located inside the unit circle and thus indicates a stable system. Furthermore the damping ratio, which influences the overshoot, will not decrease below 0.7, which normally is a desired damping ratio when designing controllers. Thus,

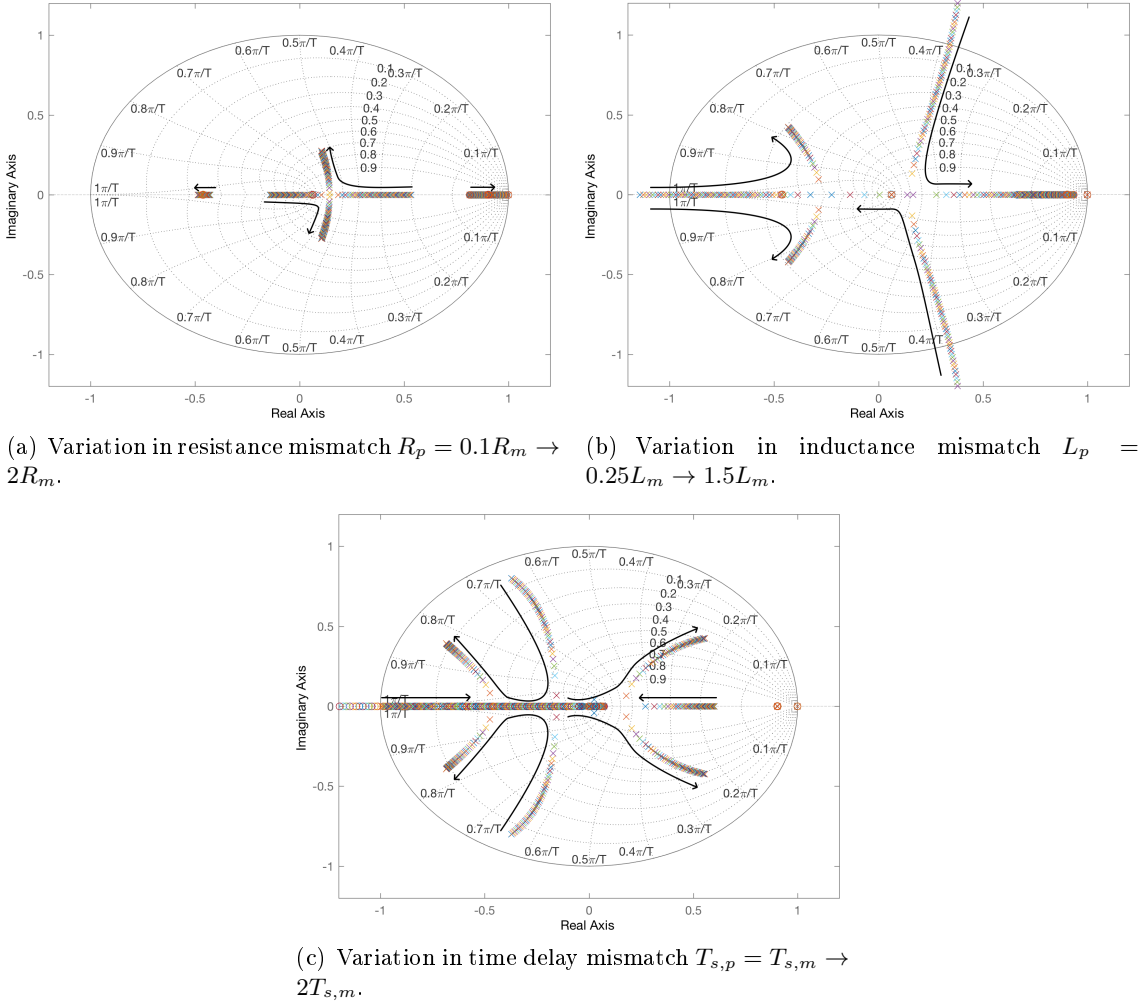


Figure 4.15: Pole zero map in the case of model mismatch at a sampling frequency of 2 kHz. Subscript  $p$  denotes plant value and subscript  $m$  denotes model value. In all cases the arrows indicates the movement of the poles as the plant values changes compared with the SP model values as indicated. For each case only one parameter is changed keeping the other values as a perfect match. The controller is the same as in figure 4.14.

mismatch in the resistance value will not have a significant effect on the system stability and overshoot.

When looking at figure 4.15(b), where the plant inductance is varied from  $0.25L_m \rightarrow 1.5L_m$ , it is noticed that with large overestimated values (low plant inductance), the system is no longer stable. When compared with figure 4.15(a), it is seen that the stability is more dependent on a accurate estimation of the inductance compared to the resistance. Figure 4.15(c) shows the movement of the poles when the time delay is changed from  $T_{s,m} \rightarrow 2T_{s,m}$ . A rather complex change in pole location is observed, but the poles are located within the unit circle. Even though the system seems to be stable in the analysed range of time delays, a underestimated value for the time delay can easily cause unacceptable system performance due to a very low damping ratio. A test is performed when the time delay of the model is set to be zero when the plant includes a time delay of  $1.5T_s$ . Here two poles are located outside the unit circle indicating that the system is unstable.

Hence again as shown in figure 3.15, time delay is able to cause the system to become unstable if not compensated.

As concluded for the inductance, an accurate estimation of the time delay is crucial for the SP to work satisfactory. Hence tests could be done to accurately measure the time delay. When this test is performed the time delay should not change significantly during operation in a given setup and is therefore not a crucial parameter since it will not change dependent on current and temperature levels as the inductance. The inductance can be included as function of current to account for saturation levels in the machine. In both cases, this might be undesirable due to increased model complexity, increased DSP calculation time and inconvenience of doing physical tests on the setup. A more practical approach, which could be beneficial for the industry and the flexibility for a control system to be adapted to different setups, is to make the SP independent of or less dependent on machine parameters. The investigation on how this can be achieved is given in the following sections.

## 4.5 Parameter Independent Predictors

As described in the previous section, it is advantageous to have a current predictor that is robust towards parameter variations or even better, to have a predictor that is completely independent of machine parameters. In this section, focus will be on how the model of the plant in the SP can be made independent of machine parameters or made more robust to variations in these.

### 4.5.1 MBP with Estimated Inductance

According to the previous section, it was shown that the machine parameter which has the largest impact regarding model mismatch is the inductance. Therefore in order to make a model that is more robust to parameter variations, a model independent of the inductance is investigated. One approach to obtain such a control strategy, is to make an online estimation of the inductance. Given that the  $d$ -axis current is controlled to be zero, the  $d$ -axis voltage equation reduces to

$$v_d = -\omega_e L_q i_q,$$

assuming no noise and oscillations in the  $d$ -axis current. Using this, the inductance can be estimated as

$$\hat{L} = -\frac{v_d}{\omega_e i_q}.$$

To reduce the effect of the inevitable oscillations in the  $d$ -axis current in the laboratory, the estimated inductance is filtered to get the mean value. One drawback of this simple estimation is that when the speed is zero, the estimation cannot be calculated. Therefore, one has to use an initial value for the inductance or simply use FOC at start-up and then switch controller at a certain rotor speed. By using the estimated inductance, the predicted current is calculated as for the MBP (equation 4.2.2) as

$$i_d(k+1) = \frac{v_{d,PI}(k) \left( 1 - e^{-\frac{R_s}{\hat{L}} T_s} \right) + R_s i_d(k) e^{-\frac{R_s}{\hat{L}} T_s}}{R_s},$$

where the back-EMF voltage terms are decoupled in the controller using the estimated

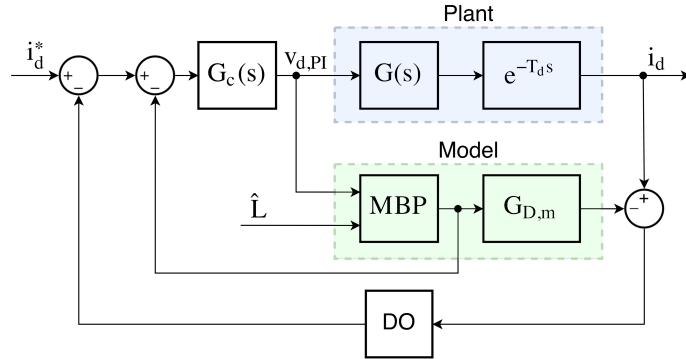
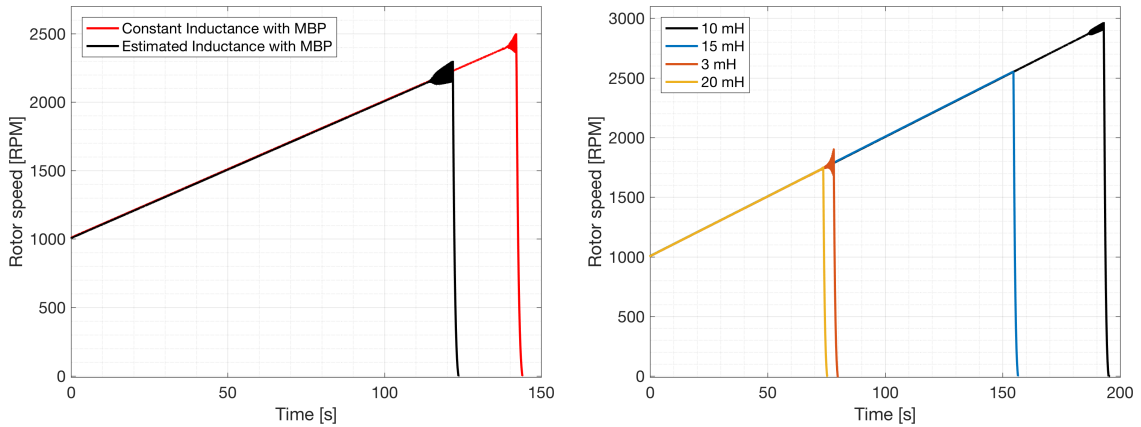


Figure 4.16: Block diagram of SP using estimated inductance in the MBP.

inductance as well. The estimation of the inductance was tested in the laboratory at no load. Here it was noticed that the estimated inductance was increasing linearly with increasing speed. At no load, the back-EMF term is not dominating the voltage equations anymore and variations in the  $d$ -axis current will have more significant effects on the inductance estimation. Furthermore, the accuracy of the measurements might not be accurate enough at these low currents, and the machine currents were not resembling a balanced three phase system as the equation assumes. Thus, to get a useful estimation of the inductance, the machine should be loaded. When this is done, the inductance is found to be independent of speed. It was estimated to be 25.8 mH. This value is of cause much bigger compared with the tested value for the machine inductance of 5.5 mH, but the inductance estimated, is based on the validity and simplicity of the machine voltage equations. This means, that any model errors will be introduced in this term. Many factors could introduce errors in the estimation, including uncompensated inverter effects, cross coupling effects in the machine, not perfectly balanced machine currents etc.



(a) Stability comparison between estimated inductance ( $K_{p,c} = 1$  and  $K_{i,c} = 10$ ) and constant inductance in model based predictor ( $K_{p,c} = 11$  and  $K_{i,c} = 3400$ ).

(b) Stability sensitivity to mismatch in inductance ( $K_{p,c} = 11$  and  $K_{i,c} = 3400$ ) of model based predictor.

Figure 4.17: Ramp test of speed to analyse stability at different estimations of the inductance. All tests are done at 2 kHz.

In figure 4.17(a), a comparison of the stability when using the estimated inductance

and constant inductance in the model based predictor can be seen. In order for the system to be stable using the estimated inductance, the PI parameters had to be decreased significantly compared to the parameters of the constant inductance (5.5 mH) MBP, seen in figure 4.17(a). Here it can be seen, that the estimated inductance, even though the PI parameters are low, are able to keep the system stable up to around 2200 RPM. As can be seen in figure 4.17(b), the MBP is tested at different values of the inductance which is both used in the current predictor and the decoupling. This is done to see the sensitivity regarding inductance estimation errors. In figure 4.17(b), it can be seen that increasing the inductance to 10 mH actually improves the stability of the MBP to a rotor speed just below 3000 RPM, ( $m_f \approx 10$ ). An inductance value of 15 mH gives approximately same result as when 5.5 mH is used. This indicates, conflicting with the analysis done in section 4.4, that the MBP used in the SP is not as sensitive to inductance mismatch as thought. In the sensitivity analyses, the DO is not included and other non-modelled behaviours could introduce robustness to the system. It can also be seen in figure 4.17(b), that the robustness is decreased if the inductance estimator underestimated the inductance, again in contradiction to the sensitivity analysis done in section 4.4. To reveal why the sensitivity analysis regarding stability, presented in section 4.4, does not seem to match the laboratory results shown in figure 4.17(b), pole-zero maps were made, where the parameters of the physical plant were held constant and the parameters of the SP model were varied, which is opposite of what was done in section 4.4. This showed the same behaviour as seen in figure 4.17(b). This indicates, that the sensitivity analysis cannot be generalised to the case of constant plant parameters with varying SP model parameters. Hence a more in-depth analysis of this has to be done in order to see the full stability consideration regarding model mismatch.

A test was also done for an inductance value of 2.7 mH. Here the system was not able to start up due to instability of the controller. The same result were found from a pole-zero map of this condition. As can be seen in figure 4.17(b), an overestimation in the inductance to some extend improves the critical frequency-modulation ratio, however, when the inductance is overestimated a lot, as seen in figure 4.17(b) with an inductance value of 20 mH, the stability is decreased significantly. This also explains, why the PI parameters have to be decreased when the inductance is estimated to 25 mH to ensure stability.

From the tests performed, it is noticed that if the inductance estimator does not underestimate the inductance in a significant manner and does not overestimate the inductance with a factor of approximately three, the SP including a machine model independent of inductance is able to keep the system stable for frequency-modulation ratios much lower compared to FOC. However this comes with the drawback of large overshoots in the currents when stepped with these overestimations in inductance. This can be seen in figure 4.18, where it can be noticed that to achieve high stability, the current response is far from acceptable. This is as expected from figure 4.14(b), where step plots were performed for inductance mismatch. Hence to achieve an improvement in controller stability while simultaneously comply with overshoot requirements, a better inductance estimator should be used. The predictor using the estimated inductance was also tested during a load step from approximately 50% of rated torque to rated torque. It was noticed,

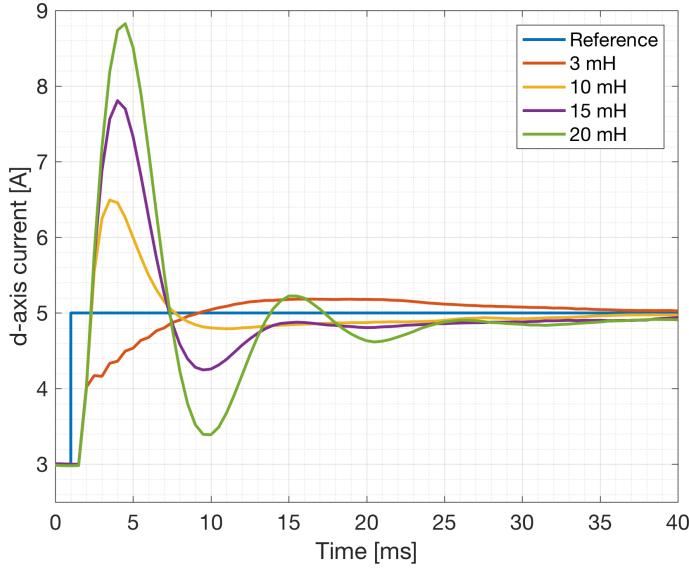


Figure 4.18: Experimental step in  $d$ -axis current when inductance is varied in MBP in the SP.

that the inductance estimation is dependent on the machine loading. At light load, the inductance value was as described, estimated to be around 25 mH, where at rated torque it was estimated to be 12 mH. This also means, that the estimator will perform better when the machine is loaded. However when the machine is not loaded, to be able to use the high PI parameters and acceptable current responses, as for the MBP, the inductance estimation should be improved in order to get a value in the vicinity of the correct physical one.

#### 4.5.2 Linear Predictor

Instead of using the voltage equations with an estimated inductance, a control strategy independent of machine parameters is investigated. A parameter independent model of the plant should be able to predict the future machine current based on available measurements. One of the simplest ways to establish that, is to assume the machine current to change linearly based on the past and present current measurement. This assumes the current to follow the same slope as for the previous calculation step. By this, the predicted future current for the  $d$ -axis is

$$\begin{aligned} i_d(k+1) &= \frac{i_d(k) - i_d(k-1)}{T_s} T_s + i_d(k) \\ &= 2i_d(k) - i_d(k-1). \end{aligned}$$

When the machine plant is a RL-circuit with a large inductance, the current changes linearly between sampling instances, when the switching frequency is sufficiently fast. This is assumed to be an acceptable approximation for this predictor to perform satisfactory. A block diagram of the scheme can be seen in figure 4.19.

The linear predictor is tested in simulation. In figure 4.20(a) a  $d$ -axis step response performed at 2 kHz can be seen and compared with FOC and SP using model based predictions. Here it is evident, that the linear predictor has a faster response compared

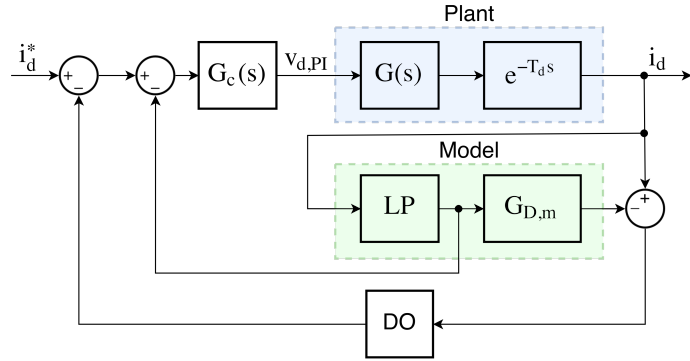
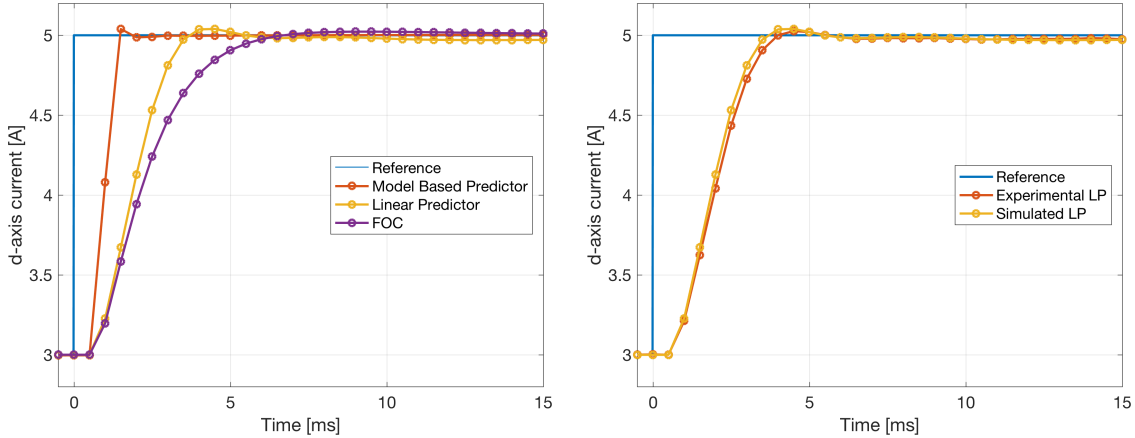


Figure 4.19: Schematic of the LP, which uses the measured currents to predict the next currents.

to FOC, but it also suffers from a longer settling time. The cut-off frequency of the DO used for the linear predictor and the MBP is 120 rad/s. In figure 4.20(b), the simulated response using LP is compared with the response obtained in the laboratory. As seen for other responses, the simulation model closely resembles the actual behaviour seen in the laboratory.



(a) Simulated  $d$ -axis current step reponse for MBP, FOC and linear predictor. The simulation is done at a sampling frequency of 2 kHz.

(b) Simulated and experimental  $d$ -axis current step reponse for linear predictor. The tests are done at a sampling frequency of 2 kHz.

Figure 4.20: Experimental and simulated response where a linear predictor is used as predictive model in the SP.

Test of stability, where the speed is ramped slowly from 1000 RPM to the point where the controller becomes unstable, is also performed for the LP. The rotor speed which resulted in instability of the controller was just below the speed when using FOC, so no improvements in stability was gained using this approach. Using this simple approach to predict the future currents, it is seen that the rise time becomes more than double that of the SP with MBP. Furthermore using the linear predictor, the rise time of the current response compared to FOC can be decreased, but the robustness and stability of the controller is decreased compared to FOC. Since the linear predictor does not use information about the voltage to be applied in the next switching state, it does not know in what direction the current will change. Including the  $dq$ -axis voltages to be applied in the next

switching period, therefore might lead to a more accurate prediction, since the predicted currents is dependent on the applied voltage. Based on this a Modified Linear Predictor (MLP) was developed. This takes into account the future voltage to be applied and the reference current when predicting the next current state. In appendix D, the analysis, implementation and test of this method is presented. The results for the MLP, showed a current step response almost as fast as seen for the MBP. This indicated, that the inclusion of reference current and output voltage of the PI controller did improve the predictability of the LP. However, when exposed to a ramped speed test, to test stability, the approach resulted in a critical frequency-modulation value higher than that achieved with FOC.

The MBP algorithm includes a rather random selection of gains to help the predict move in the correct direction and the effect of these gains on the system stability is complex to analyse. Therefore instead of a tailor made predictor, which utilises multiple gains to compensate for different complex effects in the system, a study is done to investigate the relationship between the output voltage of the PI controller and the predicted current using the MBP. This investigation is described in the following subsection.

#### 4.5.3 Investigation of Model Linearity

As described earlier, the machine plant should, (when decoupled) behave like an RL-circuit and thus in a small time step, it should be possible to assume linearity between the machine voltage and current. To further investigate if this is true, a step in the  $q$ -axis current is performed. Since a change in the  $q$ -axis current will change the speed of the machine, only a short pulse is given. Hence the rotor speed should not change much due to the large mechanical time constant compared to the electrical one. The step is performed at different rotor speeds to investigate if linearity also exists here.

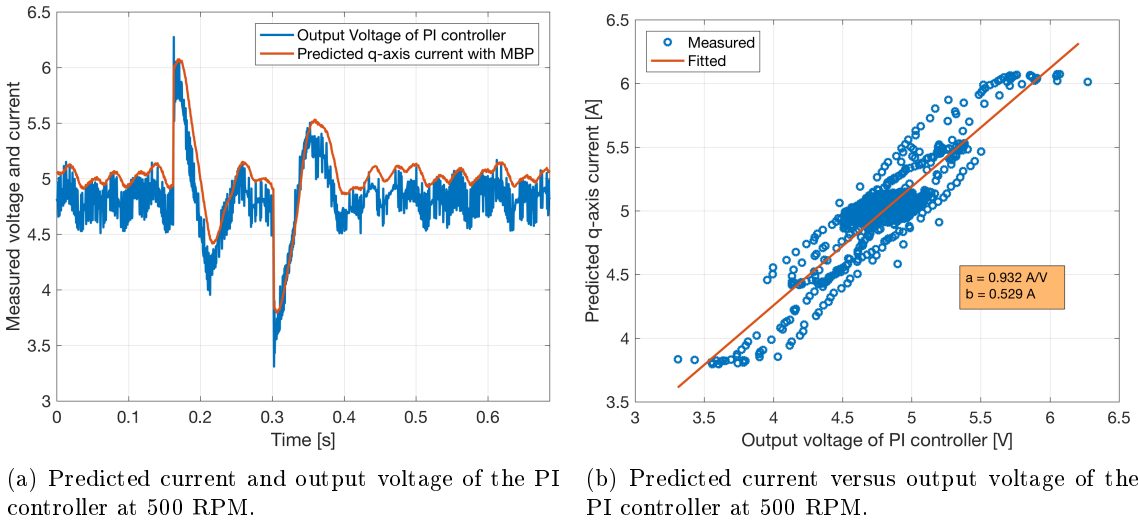


Figure 4.21: The linearity is investigated through a step in the  $q$ -axis current. The current predicted by the MBP is linearly related to the voltage output of the PI controller. The rotor speed during this test is 500 RPM

The MBP gives excellent results with an accurate plant model. Therefore the goal of a linear predictor is to reproduce the predicted output current of this. In figure 4.21(a),

the predicted output current of the MBP and the output voltage of the PI controller when decoupled can be seen. If the predicted current is plotted as a function of the output voltage of the PI controller, as seen in figure 4.21(b), an approximately linear relationship can be seen. The slope is found to be 0.932 A/V at a speed of 500 RPM.

The slope calculated as in figure 4.21(b) is done for multiple different speeds. Since the machine is loaded with the transformer and a resistive load, an increasing speed will increase the torque and hence the  $q$ -axis current. The relationship between the output of the PI controller and the predicted current where the rotor speed is varied from 0-1900 RPM can be seen in figure 4.22. This reveals a linear relationship with increasing current. A best linear fit is performed to the measured data. The fitted slope or admittance is found

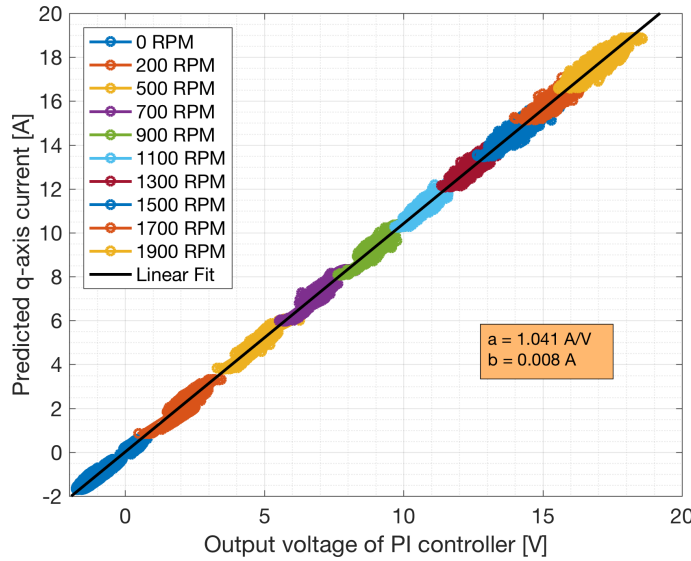


Figure 4.22: Relationship between output voltage of PI controller when decoupled and predicted  $q$ -axis current at different rotor speeds. A clear linear behaviour can be seen from the experimental data.

to be  $1.04 \text{ A/V}$ , which is equivalent to a resistance of  $0.96 \Omega$ , which is exactly the resistance of the setup at a switching frequency of 2 kHz. Furthermore, the slope approximately passes through the origin, which further supports the validity of using Ohm's law as a predictor. From this, it can be seen that linearity exist and that the predicted current of the MBP should approximately equal

$$i_q(k+1) \approx \frac{v_{q,PI}(k+1)}{R_s},$$

which is given the name, Ohm's Predictor (OP).

OP is implemented and tested in the laboratory for the prediction of the  $q$ -axis current. The  $d$ -axis current was tested with both the original MBP and using OP, resulting in almost identical behaviour. This indicates, as expected, that the linear dependency in the  $d$ -axis can also be applied when the back-EMF voltage is decoupled. In order to make the controller stable using OP the PI parameters of the current regulators, have to be decreased significantly. A step in  $d$ -axis current using OP can be seen in figure 4.23(a). Here it is evident, that the current has a very slow response with a rise time above 20 ms. However as can be seen in figure 4.24, the controller is able to stabilise the system up to just above 2000 RPM, which is a big improvement compared to FOC.

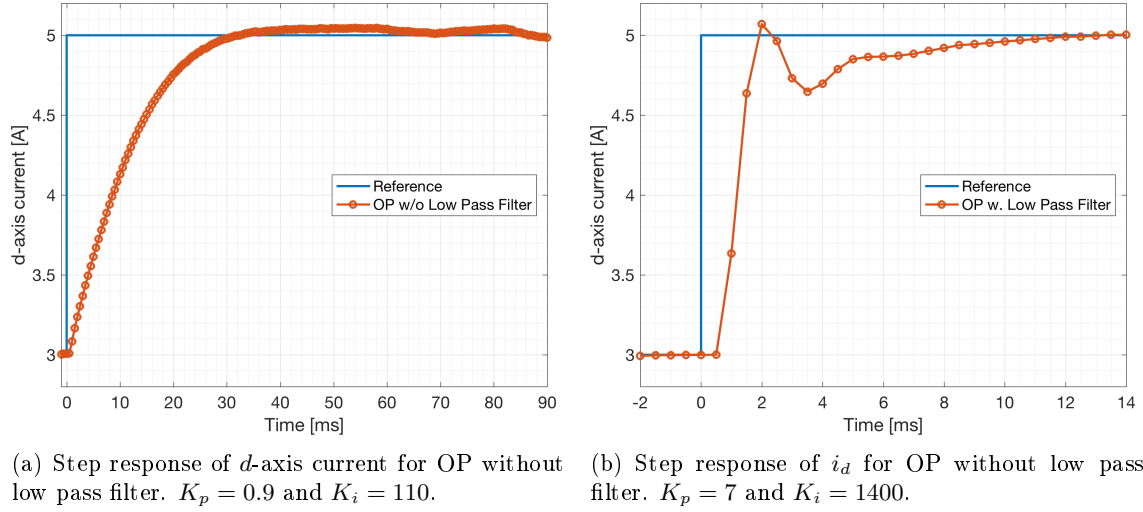


Figure 4.23: Step response of  $d$ -axis current for OP. If a low pass filter with a cut-off frequency of 200 rad/s is used at the output of the predictor, the PI controller can be tuned to get a faster response.

Since the output voltage of the PI controller includes a significant amount of noise which is directly feed through in the predicted current, the PI parameters has to be tuned conservatively in order to keep the system stable. To solve this problem, a LPF with a cut-off frequency of 200 rad/s is put on the predicted currents. This removes the unwanted noise but keeps the low frequency behaviour of the system. This greatly improves OP and permits the PI controller to be tuned much more aggressively while still complying with a maximum current overshoot of 2%. The block diagram of OP including LPF can be seen in figure 4.25.

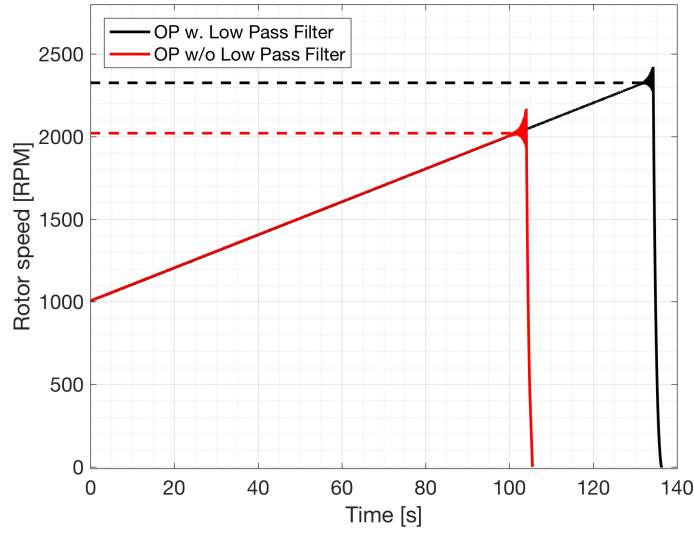


Figure 4.24: Experimental result from ramp of rotor speed using OP with and without a low pass filter. The rotor speed is slowly ramped using a rate limiter of 10 RPM/s to see at which speed, the control strategy becomes unstable. The controllers are tuned as for figure 4.23

The current response using OP with filtered predicted currents is shown in figure

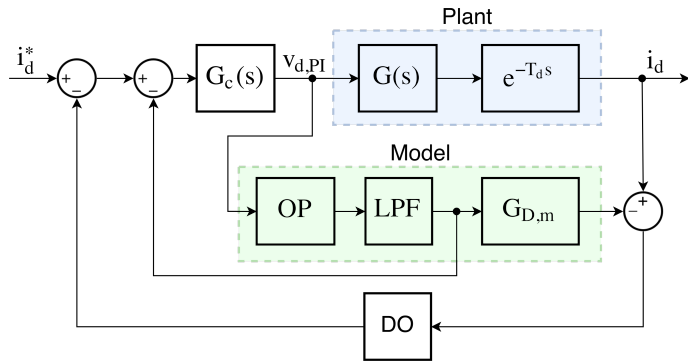


Figure 4.25: Schematic of OP, which uses the next output voltage to predict the next current. A LPF is introduced in order to attenuate noise from the output voltage of the PI controller.

4.23(b). Here it can be seen that the response is almost as fast as the MBP, but with an undershoot in the current around 3.5 ms. Using OP with the LPF included, the system is kept stable up to above 2300 RPM, which is shown in figure 4.24. Using OP, the system can be made stable down to a frequency-modulation ratio of

$$m_{f,SP} = \frac{2000 \text{ Hz}}{2320/60 \cdot 4} = 12.93,$$

which is only 7% higher than the critical frequency-modulation ratio obtained with the MBP.

Introducing a LPF to the predicted currents of OP, not only increases the bandwidth of the controller significantly, but also improves the stability and robustness of the system. Therefore, OP is extremely simple and capable of controlling the setup in a manner almost as good as the MBP when the back-EMF terms are decoupled. A great advantage of OP is, that the only machine parameter needed for the current prediction is the resistance of the setup. The resistance can quickly and easily be measured or can be estimated online. However since the back-EMF voltage is decoupled using the values for PM flux linkage and machine inductance, not much improvement is done regarding the independence of machine parameters. It is shown that equation 4.2.2, can be simplified significantly by assuming a simple linear relationship between voltage and current, but the machine parameters are still needed, since decoupling of the back-EMF voltage terms are performed.

OP including the LPF is also tested during a load step. The response is shown in figure 4.26, where the load is stepped from zero torque to nominal torque (5.8 Nm) at a rotor speed of 2000 RPM.

It is clearly seen that OP easily tracks the load step even at this low modulation frequency. Furthermore, it is seen that the speed is oscillating before the step. This is because the controller is less stable at no-load condition. This problem can also be seen in the  $dq$ -currents where the oscillations are significantly reduced when the machine is loaded. The load step from no-load to rated torque gives almost exact similar response as seen for the MBP in figure 4.13(e), which again supports the validity of assuming the model to be linear. Compared to the response using the MBP shown in figure 4.13(e), the  $dq$ -currents and hence speed were not very oscillatory at no load. This indicates that some of the robustness and stability at low currents is lost when using OP instead of the MBP.

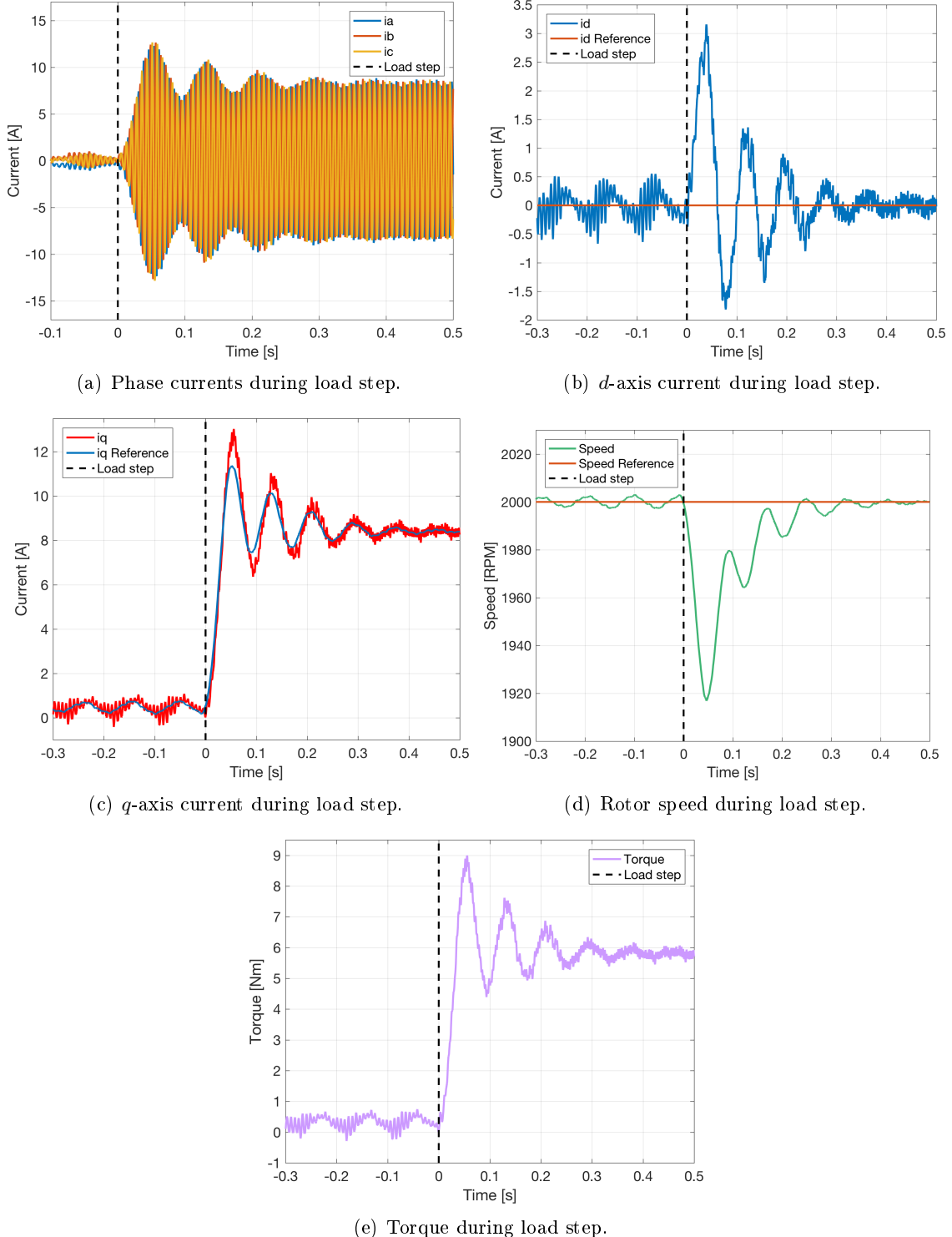


Figure 4.26: Load step at 2000 RPM using OP with LPF on the predicted currents. The sampling frequency of the system is 2 kHz and the current controllers are tuned as in figure 4.23(b).

As described earlier, the tests were done when the back-EMF voltage terms of the  $dq$ -axes were decoupled. This implies, that the PM flux linkage and machine inductance have

to be known. One way to improve OP, could be to investigate what relationship exists between the predicted current using the MBP and the voltage applied to the machine terminals including the back-EMF term. By this, a modification to OP might make it able to work satisfactory without the need to know the PM flux linkage and machine inductance. The drawback of this, is that the back-EMF term consists of the PM flux linkage, machine inductance,  $dq$ -axes currents and rotor speed, where the last two are measured. Therefore in order to make a best fit of the back-EMF term to the predicted currents, one would probably find that the fitted value approximately equals the inductance and PM flux linkage. By this, the problem is still how to select such parameters if not known. One solution could again be to try to do online estimation of the machine parameters in a more accurate manner than briefly considered in this project.

# 5

# Conclusion

Electrical machines are widely used in many industrial applications and are involved in more than 60% of the electricity consumption in the world [1, 2]. This suggests that efficient control of electrical machines is a relevant topic within the field of electrical engineering. One way of lowering losses, is to reduce the switching frequency of the inverter, since switching losses contribute significantly to the overall losses in an inverter-drive application.

Recently very high speed drives have started to receive more interest. Due to limits on IGBT switching frequencies the ratio between the switching frequency and the fundamental output frequency of the inverter,  $m_f$  (frequency-modulation ratio), will be low at these high speeds. Since the VSI is only able to change the output voltage on every switching instant, a delay of at least one switching period (typically one and a half) is inevitable when using digital control. The influence of this delay increases as  $m_f$  decreases. For these reasons, strategies to compensate time delay have been developed. A few of these include deadbeat control, which if not accurately modelled has a steady state error in the output, MPC which rely on minimisation of a cost function leading to a high computational effort, and the SP which rely on a model of the plant as for deadbeat control but still include PI controllers to remove steady state errors. Since the SP is a mature technique, this was chosen as a starting point for the time delay compensation of this project. Based on this analysis, the problem laying the basis for this project was formulated.

To test the methods developed, a laboratory setup was needed. A thorough description of this was given to ensure the reproducibility of the results achieved throughout the project. A motor-generator setup was used with the machines being of comparable size and similar parameters. Both machines were surface mounted PMSMs. Since accurate knowledge about machine parameters are essential for modelling and control, these were experimentally identified.

To control the machine, a dSPACE µC was programmed using Simulink providing the gate driver of the VSI with switching signals. The electrical and mechanical behaviour and the relation of these for a PMSM was described along with the reference frame used.

Since FOC is a widely used control method in the industry [3, 32], this is used as a reference to the predictive control strategy developed. As a starting point, controllers were designed without considering time delay. This was done for both the inner current loop and the outer speed loop. With an increasing time delay, a stable response with no overshoot using this assumption is however not realistic, hence an approximation of the delay was needed. It was shown, that in continuous time the (2,2) Padé approximation provided good results. In discrete time, a Thiran filter was found to give the best approximation. The controllers were then retuned with the delay included.

The stability of the controllers were investigated using Routh-Hurwitz' stability

criterion for the continuous case and Jury's stability criterion for the discrete time case. The stability boundary was found to be at a switching frequency of 1430 Hz and 1385 Hz for the continuous and discrete case respectively. This was validated through simulation.

The controllers were implemented in a simulation model and in the physical setup in the laboratory, showing almost identical responses. This indicated that the simulation model developed was a good representation of the physical setup. To investigate the influence of an increasing time delay, the switching frequency was decreased. This showed that as the switching frequency was decreased, a higher overshoot combined with significant oscillation starts to occur. This problem could to some extend be avoided by retuning the controllers, however, it would not be possible to achieve an acceptable rise time and overshoot. Since FOC was not performing satisfactory at a low  $m_f$ , some sort of time delay compensation was needed. Via Smith's principle, a technique known as the SP was developed. Here a model of the plant and delay were used to cancel the effects of the time delay and thus simplifying the control to a delay-free case. Simulation of the SP with a switching frequency of 2 kHz showed exceptionally good results, especially with the introduction of a DO in the outer feedback path. With a step input, the current was able to reach the reference within two sampling periods as compared to nine obtained with FOC. In both cases, the controller were tuned as fast as possible while still complying with the current overshoot requirements.

The laboratory implementation of the SP with the DO showed the same response as for the simulation. It was shown, that a reduction of 50% in  $m_f$  was possible. The SP also showed great performance when the machine was loaded.

Since the SP relies on a model of the plant, the sensitivity towards model mismatch was investigated. Here it was concluded, that the inductance was the most sensitive parameter and that an accurate resistance estimation was not crucial. It is generally not desired to have a control scheme which relies on model parameters. This is due to the added work associated with the identification of these parameters and due to parameter change caused by e.g. temperature change, which leads to model mismatch. Therefore, a parameter independent model was investigated. The layout of the SP was used as a basis, with the plant model being modified.

Online estimation of the inductance was incorporated into the strategy, by assuming the  $d$ -axis current to be zero. In a stability test performed, this method showed slightly better results compared to the MBP dependent on the value of the estimated inductance. Furthermore, it also showed higher overshoots in the current response exposed to a step when the inductance estimation was not precise. However, if overshoot is not of great concern e.g. if the load change is ramped instead of stepped, this method could result in a highly simplified model, where the only parameters necessary are the resistance and PM flux linkage.

To get a parameter independent predictive model, it was investigated whether a LP could be used. Here the predicted current was based on the present and previous current value. It showed better results when looking at a step response compared to FOC, however, in a ramp stability test, the performances were similar. Therefore, a MLP was proposed and tested. This strategy took the present value of the current, the output voltage of the PI controller and the reference current into account, making it better equipped to predict the next current value. Here results comparable to the MBP were obtained regarding a current step. The stability test for the MLP did however not result in better performance

compared to FOC and another strategy was attempted.

Since the SP with the MBP showed the best results, it was investigated whether the predicted current of the MBP could be approximated linear with respect to output voltage of the PI controller when the back-EMF voltage terms were decoupled. It was shown, that including back-EMF decoupling, it is possible to predict the next current output as the voltage output of the PI controller divided with the resistance of the setup. This control strategy was named Ohm's predictor. A LPF was added to the output of OP, resulting in similar performance compared to the MBP regarding stability test and on a load step test. Thus, if decoupling is possible, it is shown that the only needed machine parameter is the resistance of the setup.

A requirement for the current controller presented in the beginning of the project was, that the bandwidth should be 500 Hz. Due to the low switching frequency of 2 kHz this means, that the current response should reach its reference value in approximately one sampling period, which was difficult to achieve. Therefore each controller was instead tuned as fast as possible while still complying with the requirement of maximum 2% overshoot. From this, it was possible to compare the stability of the different control strategies presented, by using the ramped speed test. The controller requirements were set up, in order to be able to conclude, whether a predictive control strategy could fulfil these for frequency-modulation ratios lower than what FOC could achieve. This is throughout the project indeed validated and the SP using the MBP showed superior performance compared to FOC, allowing either the switching frequency to be reduced with 50% or the operating speed of the drive to be doubled.

## 5.1 Future Work

This section is devoted to the work and investigations that should be done to improve the stability and performance of the control strategies described throughout this project. This includes further investigation on how to improve the performance of a fully parameter independent predictor, how parameters can be estimated to get improved performance and an analysis of other predictive strategies than the SP.

### In-depth Investigation of Model Behaviour

To get a parameter independent model, the analysis of the LP and OP has to be further enhanced. This includes an in-depth analysis and understanding of the influence, the variables including voltage, current and rotor speed, have on the electrical machine. This also includes a thorough analysis of the most important characteristics for the model of the electrical machine. By this, it might be possible to further simplify the current predictor without the need for PM flux linkage and  $dq$ -axes inductances. One way to achieve that, could be to look at the difference in  $v_{PI}$  to be able to decouple or eliminate the back-EMF voltage terms of the  $dq$ -axis voltage equations. Since the rotor speed can be assumed constant from one sampling instant to the next, change in the controller might be assumed only to correspond to the RL-circuit of the machine. From this, a better understanding of the most important characteristics of the MBP, might enable the possibility to establish a predictive model which is independent of machine parameters with negligible errors compared to the MBP.

### Online Parameter Estimation

As seen for OP, it is possible to simplify the MBP significantly using the information of the resistance of the setup only. However the tests done, were performed when the back-EMF terms were decoupled. This means, that in order to get rid of the necessity of knowing the inductance and PM flux linkage, a term approximating the back-EMF term has to be developed. Since the only unknowns in the back-EMF decoupling terms are the inductance and PM flux linkage, the developed model or fitted term will probably be the inductance, PM flux linkage or a combination of these. Therefore a better approach might be, instead of assuming pre-measured machine parameters to be constant, to do online parameter estimation during machine operation. In [46], it is described how a full online parameter characterization by injecting a sinusoidal current to the  $d$ -axis during operation can be done. Based on a recursive least square algorithm for different operating points of the machine, the machine parameters can be extracted. In [47], a so-called particle swarm optimizer has been used as an optimization technique for system identification and are shown to be capable of solving the issue of parameter cross-coupling and inverter non-linearities. By this, several methods exist which offer the possibility of accurately estimate machine parameters. Here machine parameters do not have to be considered constant, neither with respect to current, temperature, cross-coupling effects or other non-linearities. This introduces model complexity, since the estimator is capable of tracking parameters variations due to change in current and temperature levels. Using accurate estimated machine parameters in the current prediction in the SP, could result in a control strategy successfully capable of ensuring stability at high time delays and parameter variations.

### Comparison to other Predictive Strategies

When an accurate model is developed e.g. by the use of parameter estimators, the performance and stability using the SP as control strategy should be compared to other predictive methods. This could include a comparison to finite set MPC, where as for the SP, a machine model is used to predict the future current. However for the MPC strategy, a cost function is used to select the switching state which minimises the error between the machine currents and their references. Here a thorough comparison regarding, stability and performance during different loading conditions should be done in order to reveal if MPC can enhance the performance of the drive compared to the SP considered in this project. By this, the best candidate should be chosen and optimised with respect to comply with industry requirements and needs. This could enhance the implementation of more predictive controllers in the future industry when a high speed drive or low frequency inverter is used.

Through-out this project, the SP and variations of this, have been considered in the search for a simple, parameter independent and accurate control strategy that is capable of compensating time delay. Even though great results were achieved using the SP, many other strategies could be tested and their drawbacks mitigated in order to develop an appealing solution for the industry. From this, the complex control problem investigated in this project, can accurately be summarised by the following quote.

*Prediction is very difficult, especially about the future.*

- Niels Bohr

# Appendix



# A

# Laboratory Setup

This chapter of the appendix shows the physical components used in the experimental setup, gives a description of the VSI including switching scheme, and describes how the measurements are taken and implemented in dSPACE.

## Motor Setup

In figure A.1, the motor setup can be seen including drive machine, load machine and coupling with a torque transducer in between.

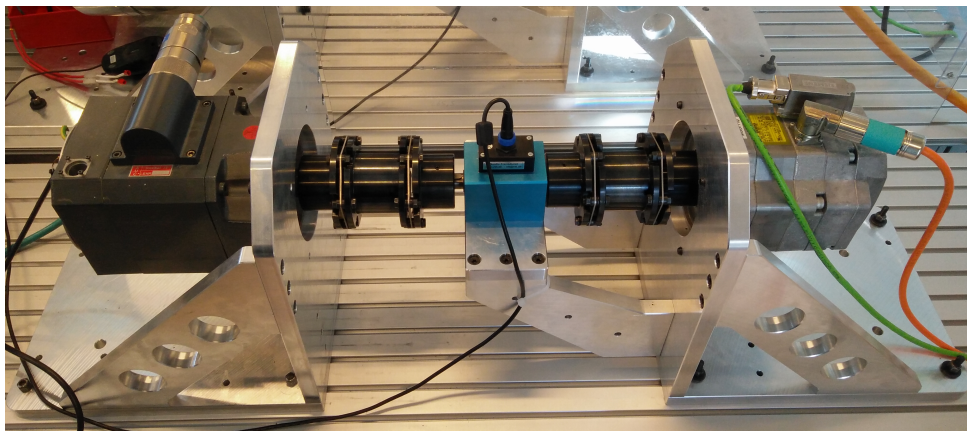


Figure A.1: Motor to generator setup, where the machine to be controlled is the one seen to the left. The load machine is seen to the right. They are coupled with a torque transducer in between.

## A.1 Voltage Source Inverter

To supply and control the PMSM, a 2-level Danfoss FC302 inverter is used to invert the DC-bus voltage into a sinusoidal voltage with variable amplitude and frequency. A schematic of the VSI can be seen in figure A.2.

Each leg corresponds to one phase where two IGBTs are used to connect the load to either the positive or negative DC-bus. Each IGBT has an antiparallel diode used to commutate the current during turn off of an inductive load. To prevent a short circuit of the DC bus, the two IGBTs in the same leg cannot be turned on at the same time. When this is fulfilled the VSI has eight possible switching states, where two of them results in zero output voltage. This happens when all the top transistors are on or when all the bottom transistors are on.

$S_x$  where  $x = a, b, c$  is defined to be a variable that takes the value one if the top transistor in the given leg is on and takes the value zero when the bottom transistor in the

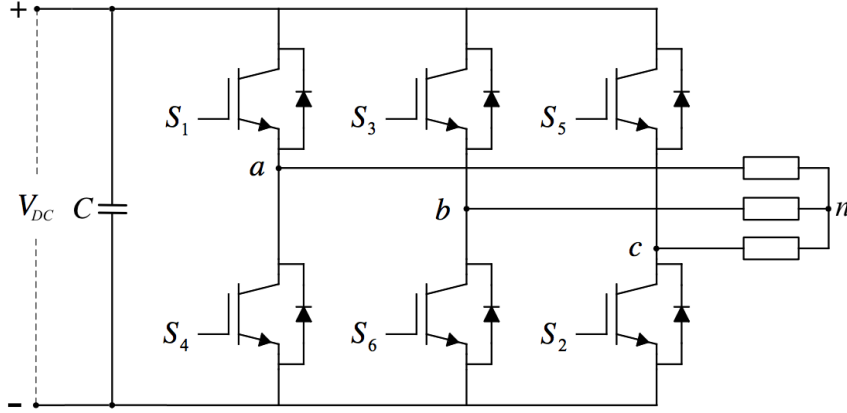


Figure A.2: Schematic of IGBT VSI [48].

given leg in on. If all the top transistors are turned on  $S_a = S_b = S_c = 1$ , the switching state is 111 which in binary corresponds to the seventh switching state. Using this, the different switching states and line-to-line output voltages can be obtained as seen in table A.1.

Switching states of the VSI					
State No.	Switching State	$v_{ab}$	$v_{bc}$	$v_{ca}$	
0	000	0	0	0	
1	100	$V_{DC}$	0	$-V_{DC}$	
2	110	0	$V_{DC}$	$-V_{DC}$	
3	010	$-V_{DC}$	$V_{DC}$	0	
4	011	$-V_{DC}$	0	$V_{DC}$	
5	001	0	$-V_{DC}$	$V_{DC}$	
6	101	$V_{DC}$	$-V_{DC}$	0	
7	111	0	0	0	

Table A.1: The line-to-line voltages of the three phases for the eight possible switching states.

Written in matrix form the line-to-line voltages are

$$\begin{bmatrix} v_{ab} \\ v_{bc} \\ v_{ca} \end{bmatrix} = V_{DC} \begin{bmatrix} 1 & -1 & 0 \\ 0 & 1 & -1 \\ -1 & 0 & 1 \end{bmatrix} \begin{bmatrix} S_a \\ S_b \\ S_c \end{bmatrix} \quad (\text{A.1.1})$$

The different switching states are simulated for a 2-level 3-phase inverter and the line-to-line voltages can be seen in figure A.3. Here it can be seen that the line-to-line voltages switch between zero and the positive and negative DC-bus voltage. The line-to-line voltages are normalized with the DC-bus voltage. Since switch 4 is switched complementary to switch 1, switch 6 complementary to switch 3, and switch 2 complementary to switch 5, actually all switching states can be seen in figure A.3.

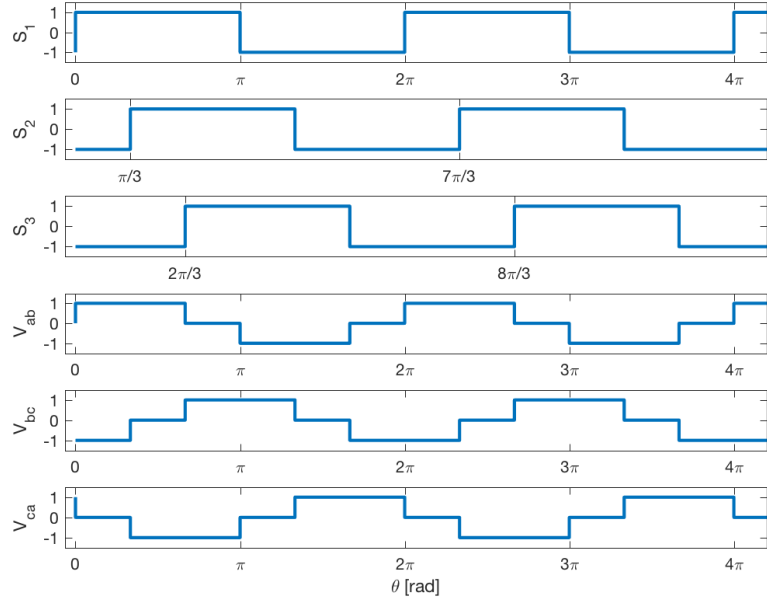


Figure A.3: Line-to-line voltages at different switching states where the gate signals for switch 1, 2 and 3 are shown. All line-to-line voltages are normalized with the DC-bus voltage.

In a star-connected symmetrical three phase system, the line-to-line voltages are related to the line-to-neutral voltages as

$$v_{ab} = v_{an} - v_{bn}$$

$$v_{bc} = v_{bn} - v_{cn}$$

$$v_{ca} = v_{cn} - v_{an}$$

and from Kirchoff's Voltage Law

$$0 = v_{an} + v_{bn} + v_{cn}$$

Using matrix A.1.1 and the relation between the line-to-line and the line-to-neutral voltages, these can be obtained using the DC-bus voltage and the switching state as

$$\begin{bmatrix} v_{an} \\ v_{bn} \\ v_{cn} \end{bmatrix} = \frac{V_{DC}}{3} \begin{bmatrix} 2 & -1 & -1 \\ -1 & 2 & -1 \\ -1 & -1 & 2 \end{bmatrix} \begin{bmatrix} S_a \\ S_b \\ S_c \end{bmatrix}$$

The line-to-neutral waveforms for the different switching states is simulated and shown in figure A.4. It can be seen that the line-to-neutral voltages can take four different values. These are  $-2V_{DC}/3$ ,  $-V_{DC}/3$ ,  $V_{DC}/3$  and  $2V_{DC}/3$ .

The simulations presented and the equations used assumes that the IGBTs are ideal and that there is no dead time in the inverter. By this, it is shown that by selecting

switching states in a given order, the VSI is able to produce a bipolar voltage to the load, which will imitate a sinusoidal voltage. How this order should be selected will be described in the following subsection.

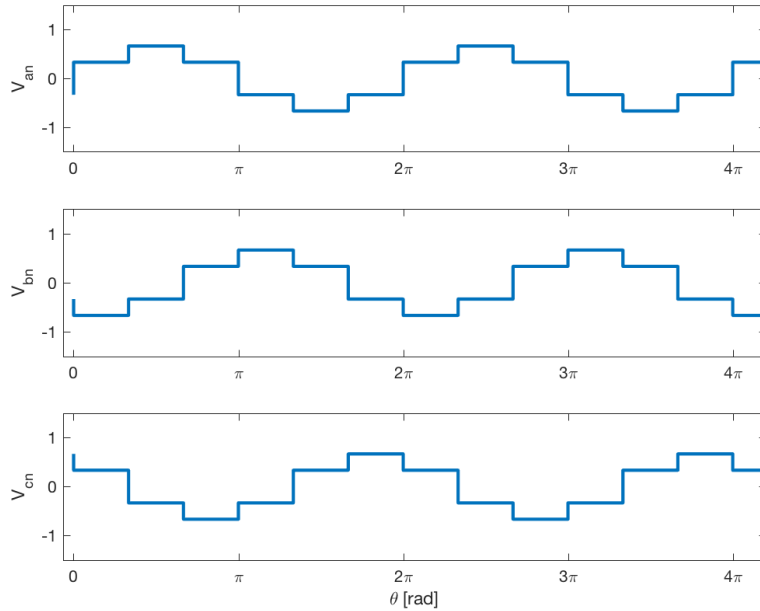


Figure A.4: Line-to-neutral voltages at the different switching states shown in figure A.3. All line-to-neutral voltages are normalized with the DC-bus voltage.

### A.1.1 Modulation Scheme

To control the transistors in the inverter to produce a desired output voltage, a modulation scheme is needed. Two widely used methods for a sinusoidal reference is the Sinusoidal Pulse Width Modulation (SPWM) and SVM. SVM is often used since it offers easier digital implementation, higher utilisation of the input DC voltage and lower voltage THD compared to SPWM [49, 50]. By injecting a third order harmonic to the SPWM the output voltage can be boosted in the linear range enabling a higher DC voltage utilisation as for SVM. However, compared to SVM, Third Harmonic Injection PWM does not equally distribute the zero vectors and hence impose non-uniform stress on the transistors. Based on this description, SVM will be the modulation technique used in this project.

As the name suggests, this technique calculates the duty cycles of the switching variables ( $S_a$ ,  $S_b$ , and  $S_c$ ), such that a desired reference voltage space vector is obtained. SVM originates from the fact, that in a three-phase system there are only two independent variables. From this, any three phase signal can be represented in a two coordinate system. Here it is chosen that the real axis is aligned with the axis of phase  $a$  and the imaginary axis is leading with  $90^\circ$ . To find the voltage space vector, each phase voltage is projected

to the real axis of the two-coordinate system as

$$\begin{aligned}\mathbf{v}_{\alpha\beta} &= \frac{2}{3} \left( \mathbf{v}_a e^{j0^\circ} + \mathbf{v}_b e^{j120^\circ} + \mathbf{v}_c e^{-j120^\circ} \right) \\ &= \frac{2}{3} \left( \mathbf{v}_a - \frac{1}{2} \mathbf{v}_b - \frac{1}{2} \mathbf{v}_c \right) + j \left( \frac{\sqrt{3}}{2} \mathbf{v}_b - \frac{\sqrt{3}}{2} \mathbf{v}_c \right),\end{aligned}\quad (\text{A.1.2})$$

where the real part is the  $\alpha$  component and the imaginary part is the  $\beta$  component of the space vector. In matrix form this is

$$\begin{bmatrix} v_\alpha \\ v_\beta \end{bmatrix} = \frac{2}{3} \begin{bmatrix} 1 & -\frac{1}{2} & -\frac{1}{2} \\ 0 & \frac{\sqrt{3}}{2} & -\frac{\sqrt{3}}{2} \end{bmatrix} \begin{bmatrix} \mathbf{v}_a \\ \mathbf{v}_b \\ \mathbf{v}_c \end{bmatrix},$$

which is also known as the Clarke transformation, which transform the three phase voltage phasors into a two coordinate stationary frame reference system.

In figure A.5, the eight different space vectors can be seen. Here the six active vectors create the six sectors I-VI. In a given sector, the reference voltage space vector is obtained by switching between the two adjacent voltage vectors. As an example, the reference vector  $\mathbf{U}_c$  can be represented by switching between the vectors  $\mathbf{u}_4$ ,  $\mathbf{u}_6$  and  $\mathbf{u}_7$ . The voltage vector  $\mathbf{U}_c$  is therefore found as vector summation between the logical states of  $\mathbf{u}_4$  and  $\mathbf{u}_6$  in a given time. The voltage vector  $\mathbf{U}_c$  can at maximum have the length to the circle shown in figure A.5, which corresponds to operating in the linear region avoiding over modulation [51].

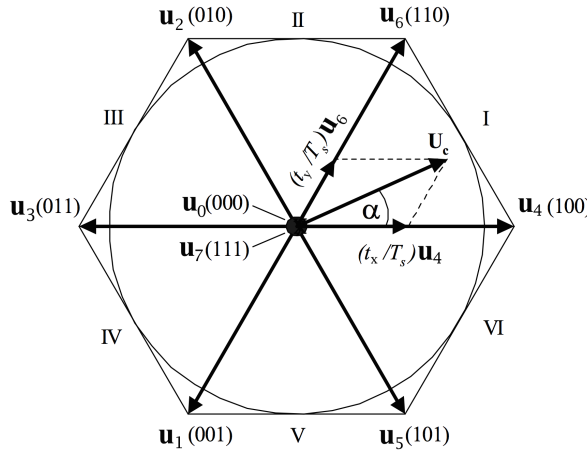


Figure A.5: Representation of space vector and active and zero switching states [52].

To keep the switching losses of the transistors as low as possible only, one bit at a time is changed in the logical states and every transistor pair in a leg is only switched once in a switching period. Hence, for sector I given that the last switching state was  $\mathbf{u}_0$ , the switching sequence will be

$$\mathbf{u}_0 \rightarrow \mathbf{u}_4 \rightarrow \mathbf{u}_6 \rightarrow \mathbf{u}_7$$

If the last switching state was  $\mathbf{u}_7$ ,  $\mathbf{u}_7$  and  $\mathbf{u}_0$  will be interchanged [53]. From figure A.5, the reference voltage can be written as

$$\begin{aligned} \mathbf{U}_c &= \frac{t_x}{T_s} u_4 + \frac{t_y}{T_s} u_6 e^{j\pi/3} \\ &= \frac{t_x}{T_s} \frac{2}{3} V_{DC} + \frac{t_y}{T_s} \frac{2}{3} V_{DC} \left( \frac{1}{2} + j \frac{\sqrt{3}}{2} \right). \end{aligned}$$

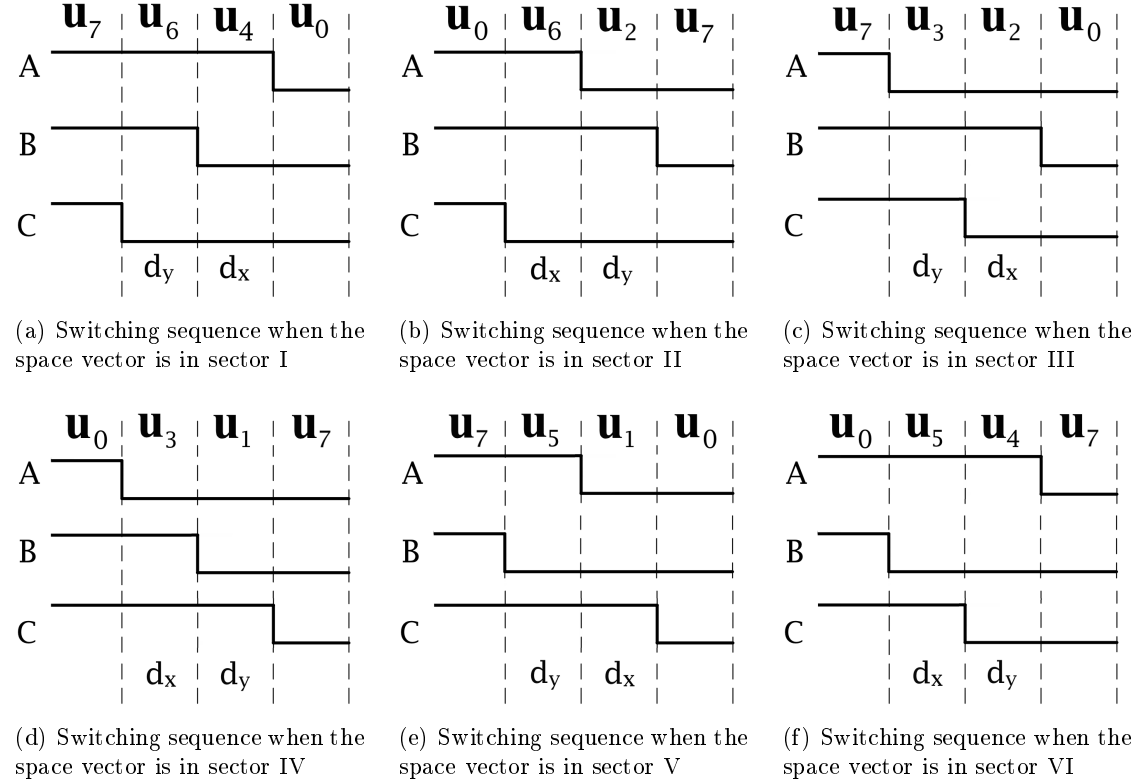


Figure A.6: Half of the symmetric switching sequence for the different sectors. These are used to formulate the expressions for the duty cycles for each leg.

Solving for the fractional time of the switching period for the different logical states one obtains that

$$d_x = \frac{t_x}{T_s} = \frac{\sqrt{3}U_c}{V_{DC}} \sin(\pi/3 - \alpha) \quad (\text{A.1.3})$$

$$d_y = \frac{t_y}{T_s} = \frac{\sqrt{3}U_c}{V_{DC}} \sin \alpha, \quad (\text{A.1.4})$$

where  $U_c \leq V_{DC}/\sqrt{3}$ .  $U_c$  is the length of the reference voltage vector and  $\alpha$  is the angle between the reference vector and the  $x$ -location in a given sector. By knowing the desired three phase voltages, these can be transformed into  $\alpha\beta$ -components where  $U_c$  and  $\alpha$  is calculated as

$$\begin{aligned} U_c &= \sqrt{v_\alpha^2 + v_\beta^2} \\ \alpha &= \tan^{-1} \left( \frac{v_\beta}{v_\alpha} \right) \end{aligned}$$

From this,  $d_x$  and  $d_y$  can be calculated as shown in equation A.1.3 and A.1.4. These are then used to determine the duty cycles for each inverter leg. The switching sequence is always symmetrical giving that the duty cycles can be obtained by inspecting only one half of the symmetric switching sequence for each sector. The switching sequence for the different sectors can be seen in figure A.6. In sector I,  $d_x$  is located at  $\mathbf{u}_4$  and  $d_y$  is located at  $\mathbf{u}_6$ . For sector II their locations are shifted  $60^\circ$ .

### Matrices for the different sectors

Sector	Matrix for switching times $d_x, d_y$	Matrix for duty cycles $D_a, D_b, D_c$
I	$\begin{bmatrix} 1 \\ d_x \\ d_y \end{bmatrix} = \begin{bmatrix} 1 & 0 & 1 \\ 1 & -1 & 0 \\ 0 & 1 & -1 \end{bmatrix} \begin{bmatrix} D_a \\ D_b \\ D_c \end{bmatrix}$	$\begin{bmatrix} D_a \\ D_b \\ D_c \end{bmatrix} = \frac{1}{2} \begin{bmatrix} 1 & 1 & 1 \\ 1 & -1 & 1 \\ 1 & -1 & -1 \end{bmatrix} \begin{bmatrix} 1 \\ d_x \\ d_y \end{bmatrix}$
II	$\begin{bmatrix} 1 \\ d_x \\ d_y \end{bmatrix} = \begin{bmatrix} 0 & 1 & 1 \\ 1 & 0 & -1 \\ -1 & 1 & 0 \end{bmatrix} \begin{bmatrix} D_a \\ D_b \\ D_c \end{bmatrix}$	$\begin{bmatrix} D_a \\ D_b \\ D_c \end{bmatrix} = \frac{1}{2} \begin{bmatrix} 1 & 1 & -1 \\ 1 & 1 & 1 \\ 1 & -1 & -1 \end{bmatrix} \begin{bmatrix} 1 \\ d_x \\ d_y \end{bmatrix}$
III	$\begin{bmatrix} 1 \\ d_x \\ d_y \end{bmatrix} = \begin{bmatrix} 1 & 1 & 0 \\ 0 & 1 & -1 \\ -1 & 0 & 1 \end{bmatrix} \begin{bmatrix} D_a \\ D_b \\ D_c \end{bmatrix}$	$\begin{bmatrix} D_a \\ D_b \\ D_c \end{bmatrix} = \frac{1}{2} \begin{bmatrix} 1 & -1 & -1 \\ 1 & 1 & 1 \\ 1 & -1 & 1 \end{bmatrix} \begin{bmatrix} 1 \\ d_x \\ d_y \end{bmatrix}$
IV	$\begin{bmatrix} 1 \\ d_x \\ d_y \end{bmatrix} = \begin{bmatrix} 1 & 0 & 1 \\ -1 & 1 & 0 \\ 0 & -1 & 1 \end{bmatrix} \begin{bmatrix} D_a \\ D_b \\ D_c \end{bmatrix}$	$\begin{bmatrix} D_a \\ D_b \\ D_c \end{bmatrix} = \frac{1}{2} \begin{bmatrix} 1 & -1 & -1 \\ 1 & 1 & -1 \\ 1 & 1 & 1 \end{bmatrix} \begin{bmatrix} 1 \\ d_x \\ d_y \end{bmatrix}$
V	$\begin{bmatrix} 1 \\ d_x \\ d_y \end{bmatrix} = \begin{bmatrix} 0 & 1 & 1 \\ -1 & 0 & 1 \\ 1 & -1 & 0 \end{bmatrix} \begin{bmatrix} D_a \\ D_b \\ D_c \end{bmatrix}$	$\begin{bmatrix} D_a \\ D_b \\ D_c \end{bmatrix} = \frac{1}{2} \begin{bmatrix} 1 & -1 & 1 \\ 1 & -1 & -1 \\ 1 & 1 & 1 \end{bmatrix} \begin{bmatrix} 1 \\ d_x \\ d_y \end{bmatrix}$
VI	$\begin{bmatrix} 1 \\ d_x \\ d_y \end{bmatrix} = \begin{bmatrix} 1 & 1 & 0 \\ 0 & -1 & 1 \\ 1 & 0 & -1 \end{bmatrix} \begin{bmatrix} D_a \\ D_b \\ D_c \end{bmatrix}$	$\begin{bmatrix} D_a \\ D_b \\ D_c \end{bmatrix} = \frac{1}{2} \begin{bmatrix} 1 & 1 & 1 \\ 1 & -1 & -1 \\ 1 & 1 & -1 \end{bmatrix} \begin{bmatrix} 1 \\ d_x \\ d_y \end{bmatrix}$

Table A.2: The matrix relating the duty cycles to the switching times  $d_x$  and  $d_y$ . The inverse matrix is shown to evaluate the duty cycles from the switching times calculated in equation A.1.3 and A.1.4 in each sector.

As an example of how to find the expression for the duty cycles of the three legs, sector I is used. The switching sequence for sector I is shown in figure A.6(a). If the duty cycles  $D_7$  and  $D_0$  are chosen to be equal, sector I is expressed as

$$1 = D_a + D_c$$

$$d_x = D_a - D_b$$

$$d_y = D_b - D_c$$

where  $D$  represent the duty cycle. This can be written in matrix form. Since the duty cycles are the unknown the inverse matrix is calculated. These matrices are calculated similarly for all the sectors and is shown in table A.2.

To implement SVM, the calculated duty cycles for each leg is compared with a triangular waveform switching at the switching frequency of the inverter to generate the switching pulses ( $S_a$ ,  $S_b$  and  $S_c$ ) to the transistors.

## A.2 dSPACE

In figure 2.1 presented in chapter 2, the dSPACE system was introduced as a block that interfaces Simulink on a PC with the motor setup. The purpose of this section, is to give a more detailed description of the operation and functionality of the dSPACE system. In figure A.7, a detailed view of the dSPACE system can be seen. Using MATLAB Simulink

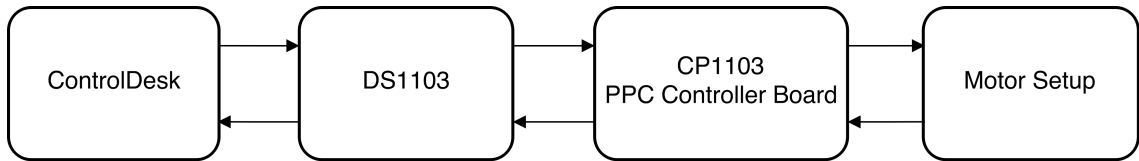


Figure A.7: Structure of dSPACE system.

and dSPACE Real-Time Interface library, the DS1103 is fully programmable from the block diagram environment in Simulink. The Simulink model is compiled into C-code, which is loaded into ControlDesk and implemented on the DSP DS1103.

*ControlDesk* is a user interface to the DSP platform, which enables real-time monitoring of measured signals and online change of model variables [54]. The DS1103 is the controller board mounted in a dSPACE expansion box. As seen in figure A.7 a connector panel, the CP1103, is connected between the DSP and the motor setup. To output switching signals for the VSI and to measure machine currents, DC link voltage and rotor position, the connector panel is used as an ADC and DAC between the inverter-motor setup and the DSP. Voltage and currents are measured using LEM sensors (LV 25-P and LA 55-P) connected to the ADC channels on the connector panel. The rotor position is measured using an digital incremental encoder, which is connected to an encoder input on the connector panel. The PWM output channels of the slave DSP is used for set, reset and PWM outputs for the inverter. Using an add-on board to the connector panel, the connection to the inverter is done through optical fibres. Some of the specifications of the dSPACE system is listed below.

- Motorola PowerPC 750GX running at 400 MHz [55].
- Slave DSP TI's TMS320F240 Subsystem running at 20 MHz .
- 16 channels ADC, 16 bit,  $\pm 10$  V.
- 4 channels ADC, 12 bit,  $\pm 10$  V.
- 8 channels DAC, 14 bit,  $\pm 10$  V.
- Incremental Encoder Interface with 7 channels.
- 10 PWM output channels
- Software tools

- Matlab/Simulink R2015b
- RTI1103 version 7.5
- ControlDesk version 5.5p2

Further information on how the measurement circuits are made and which considerations that have been done is regarding this is to be described in the following paragraph.

### Data Acquisition

To be able to successfully control the PMSM, measurements of the system are needed in the feedback control to be able to correct any steady state or transient errors. The measurements needed for this project includes the three phase currents, input DC link voltage applied to the inverter and the rotor position and velocity of the machine. In industrial applications, cost efficiency has high priority and it is preferable to have as few measurements as possible, the rotor position and velocity can be estimated and in some applications only two current measurements are sufficient, since the third can be found from these two. Since the focus of this project is not on position estimation and cost efficiency of the setup, all the mentioned quantities are measured directly in the setup.

The DC link voltage is measured using a LEM LV 25-P voltage transducer. The sensor has galvanic isolation between the primary and secondary circuit of the transducer. The voltage transducer can be seen in figure A.8. Since the transducer uses current to measure a voltage, the input voltage has to be converted into a current using the resistor  $R_1$ , seen in figure A.8. The nominal input current of the transducer is 10 mA RMS and the allowed maximum measurable input DC link voltage is selected to be 800 V. Hence a resistance of 80 k $\Omega$  will result in an input RMS current of 10 mA at that voltage. The transformer turns ratio is  $K_{N,DC} = 2.5$ . Hence when the input voltage is maximum, the current in the secondary circuit will be 25 mA RMS. The ADC on the PPC controller board has a maximum peak input voltage of  $\pm 10$  V. Since the dSPACE ADC is not capable of measuring current, the secondary current has to be converted to a voltage in the voltage range of the ADC. The resistance needed on the secondary side of the voltage transducer is

$$R_{M,DC} = \frac{10V}{25mA} = 400\Omega.$$

Since the input voltage is DC, the primary current is also DC and hence the maximum allowed RMS value of 25 mA is used in the calculation instead of  $\sqrt{2} \cdot 25\text{mA}$  which would be done if the measurements were AC. Among the resistors available, a resistance of 350 $\Omega$  was used for the secondary side of the voltage transducer. This also adds some margin in the measurements. This means, that when the input voltage is 800 V, the ADC input voltage is  $25mA \cdot 350\Omega = 8.75V$ . Using the 16-bit ADC channel of the dSPACE, the input voltage will have a resolution of

$$V_{DC,Res} = \frac{800V}{\frac{8.75V}{10V}(2^{16} - 1)} = 13.95mV,$$

which is acceptable for the input voltage measurement.

To measure the phase currents of the machine, LEM LA 55-P current transducers have been used. They have a nominal primary current of 50 A RMS, a conversion ratio of

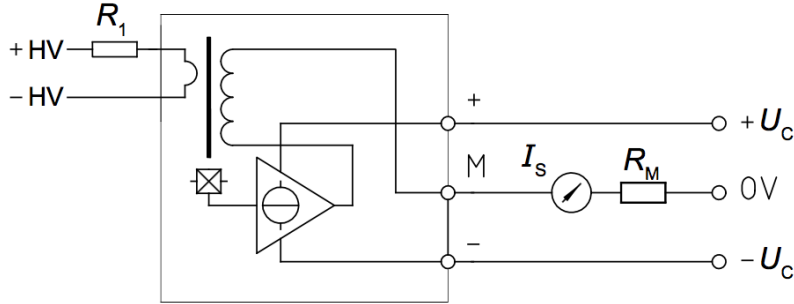


Figure A.8: Circuit diagram of LEM LV 25-P voltage transducer. Picture is from datasheet.

$K_N = 1/1000$  and hence a nominal secondary current of 50 mA RMS. Since the quantity to be measured is current, no input resistor is needed. This can also be seen in figure A.9. The maximum current of the Danfoss inverter is 25 A peak. Therefore, this value is used as the maximum current to be measured using the current transducers. To be able to utilize the full range of the transducer, the input current wire is put twice through the current transducer. This will double the generated flux in the transducer and hence an input current of 25 A appear as 50 A. Again due to limitations in resistor values and to add some margin to the measurements, a secondary measurement resistance of 150  $\Omega$  is used. This gives for a positive peak current of 25 A, an input voltage to the ADC of 7.5 V. Hence using this configuration, the resolution of the phase currents are

$$i_{ph,Res} = \frac{25A}{\frac{7.5V}{10V}(2^{16} - 1)} = 0.5mA,$$

which is acceptable for the given application.

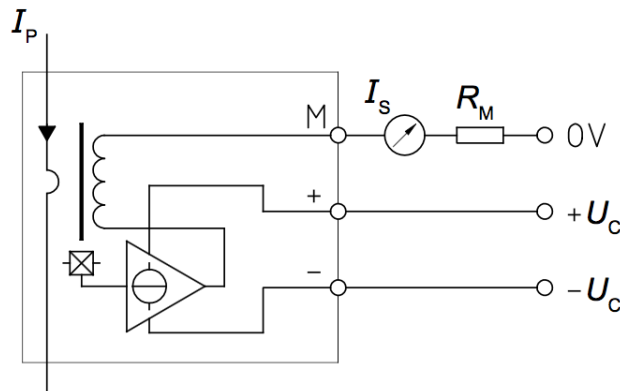


Figure A.9: Circuit diagram of LEM LA 55-P current transducer. Picture is from datasheet.

Three such configurations of current transducers are implemented on a PCB (see figure A.10) and the measurements are connected to the PPC controller board (see figure A.11). Since current is less susceptible to noise compared to voltage, the conversion of the secondary current to ADC input voltage, should be done as close as possible to the dSPACE ADC input. Hence, the secondary side resistors are soldered directly on the back of the

ADC input of the PPC controller board.

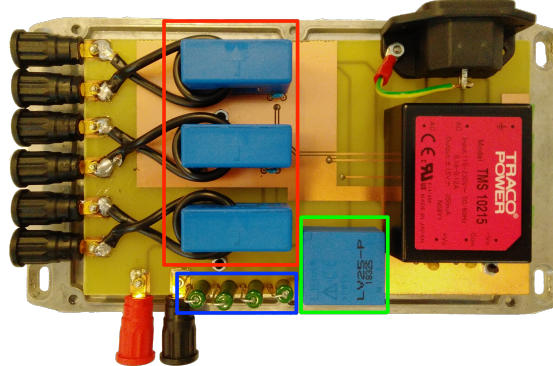


Figure A.10: PCB with the three current sensors and a voltage sensor. The red box shows the current transducers, the green box shows the voltage transducer and the blue box shows the primary side resistors used for the voltage measurement.

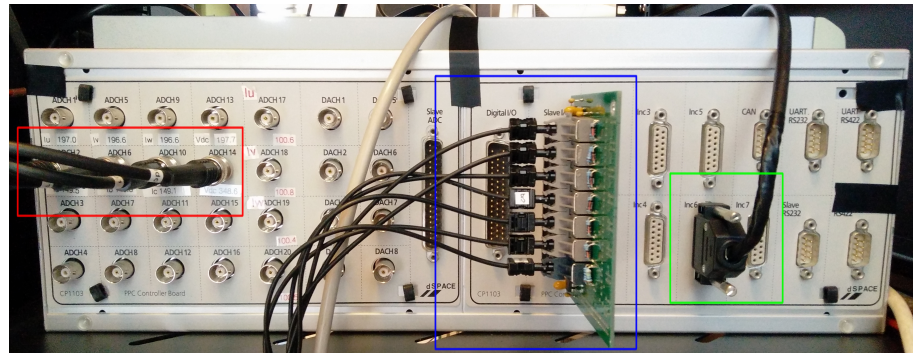


Figure A.11: PPC Controller board from dSPACE. The red box shows the 16-bit ADC inputs, where the current and voltage measurements are connected. The blue box shows the add-on PCB, where the digital outputs to the inverter are converted to light pulses transmitted in fibre optical cables. The green box shows the connection of the incremental encoder to dSPACE.

To measure the rotor position and velocity a Scancon SCA50 industrial encoder is used. This is a digital incremental encoder and it is mounted directly on the shaft of the machine. The encoder gives 4096 pulses per revolution and hence has a position resolution of  $2\pi/4096 = 1.5 \text{ mrad} = 0.088^\circ$ . In figure A.12, the data acquisition as implemented in dSPACE can be seen. Since the ADC measures a voltage in the range of  $\pm 10 \text{ V}$ , these measurements have to be converted back to its original value. This is done in the reverse order as described above and the conversion can be seen in figure A.12. All measurements from the ADC have to be multiplied with 10, since dSPACE inherently scales down the measurements with a factor of 10. To improve the accuracy of the current measurements, the common mode current is removed as shown in figure A.12. To get accurate measurements, all LEM sensors are calibrated against a measurement of either zero current or voltage, dependent on the quantity to be measured by the transducer. This offset is included in the model to make this calibration and correct the measurements.

When the encoder is connected to the incremental encoder interface of the dSPACE PPC controller board, the measured input in the model is the number of pulses counted in the last sampling period. This number is converted into rotor position and velocity as shown in figure A.12.

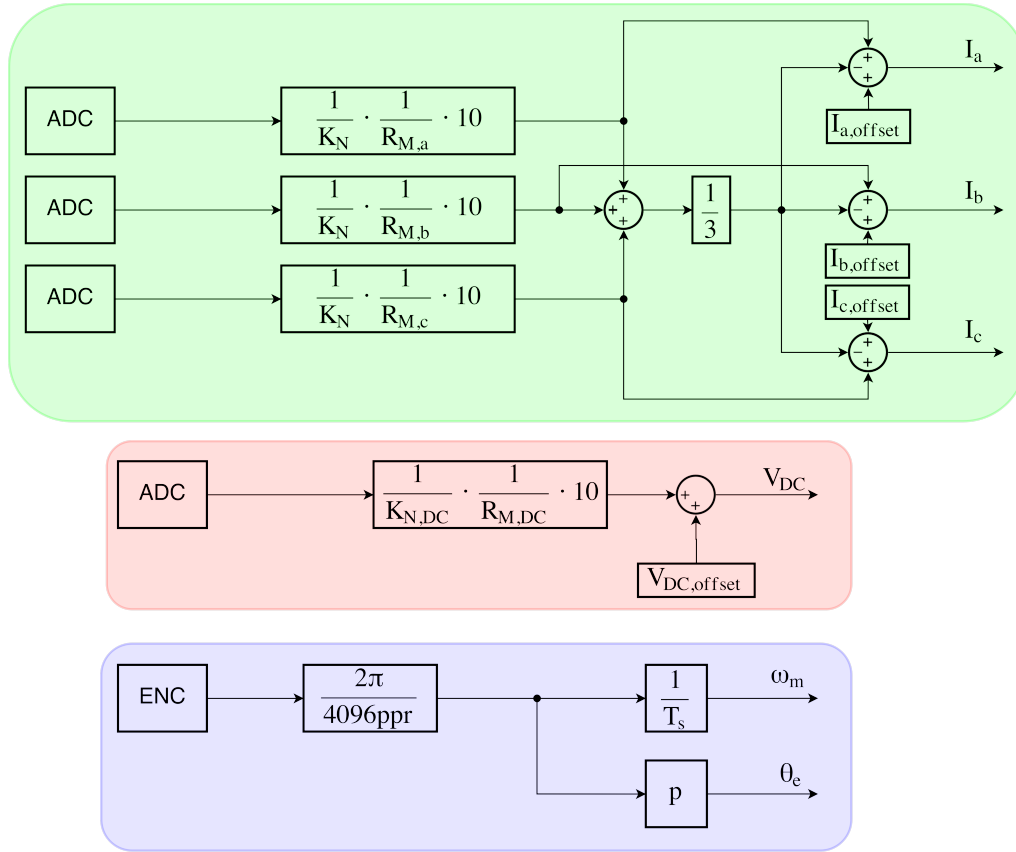


Figure A.12: Data acquisition for voltage, currents and rotor position as done in the experimental setup. The green box shows the data acquisition for the current, the red box for the voltage and the blue box is for the position measurement.

# B

# System Parameter Identification

## B.1 Permanent Magnet Flux Linkage

The machine used in this project is a permanent magnet machine, so the influence of the rotor magnets has to be known. The flux linkage of the permanent magnets located in the rotor links the stator phase windings when the machine is running. When the rotor is rotating, a time varying flux linkage is generated which induces a voltage in the stator phase windings. Since the flux linkage of the permanent magnets affects the  $q$ -axis voltage equation and is proportional to the produced torque, this quantity is important to know.

### Hypothesis

The PMSM voltage equations described in section 2.1, will be used to calculate the PM flux linkage. If the machine under test is kept open-circuited, the  $dq$ -currents will be zero and the  $dq$ -axis voltages will be

$$v_d = 0$$

$$v_q = \omega_e \lambda_{mpm}.$$

Since  $v_d = 0$ , the peak value of the stator phase-to-neutral voltage will be equal to the  $q$ -axis voltage. Hence

$$\lambda_{mpm} = \frac{v_q}{\omega_e} = \frac{V_{q,l-n}}{\omega_e}.$$

### Execution and Results

The drive machine is kept open circuited and rotated as a generator at different speeds by the Siemens load machine. Since the neutral point of the drive machine is not accessible, the measured open circuit three-phase line-to-line voltages is transformed into line-to-neutral voltages as

$$\begin{bmatrix} v_{an} \\ v_{bn} \\ v_{cn} \end{bmatrix} = \frac{1}{3} \begin{bmatrix} 1 & 0 & -1 \\ -1 & 1 & 0 \\ 0 & -1 & 1 \end{bmatrix} \begin{bmatrix} v_{ab} \\ v_{bc} \\ v_{ca} \end{bmatrix}.$$

Since the back-EMF voltage will contain harmonic components due to the physical structure of the machine, a FFT is performed on the measured data to find the peak value of the fundamental component of the back-EMF voltage. From the fundamental component of the line-to-neutral induced voltage and the measured angular velocity of the machine, the values for the PM flux linkage is calculated and can be seen in table B.1. A mean of the obtained values is used as the measured value for the PM flux linkage. This is calculated to be 0.1151 Wb.t.

<b>Permanent Magnet Flux Linkage at different machine speeds</b>		
Speed [RPM]	Line-to-neutral voltage [V]	PM flux linkage [Wb]
500	23.85	0.1139
1000	49.60	0.1184
1500	70.95	0.1129
2000	99.96	0.1193
2500	117.31	0.1120
3000	142.95	0.1138
Mean:		0.1151

Table B.1: Measured fundamental component of line-to-neutral voltage (EMF) at open circuit test performed at different rotor speeds. The PM flux linkage is calculated and the mean value is used as the constant machine parameter.

## B.2 Mechanical Parameters

To link the torque to the machine angular velocity, mechanical properties of the setup have to be known. These include inertia, viscous friction coefficient and the Coulomb friction of the full setup including drive machine, coupling, and load machine. Core losses of the machines will not be considered in this analysis and will therefore implicitly be accounted for in the mechanical model. It is assumed, that the increase in core losses due to increasing rotor speeds will not affect the measured torque in a significant way. This section has the purpose of describing how these mechanical parameters are found experimentally.

### Hypothesis

The equation linking the electromagnetic torque to the angular velocity of the machine is

$$T_e = J \frac{d}{dt} \omega_m + B_m \omega_m + T_L,$$

where  $T_L = T_l + J_0$  where  $T_l$  is the load torque and  $J_0$  is the Coulomb friction. When the machine operates in steady state at no load and at a given angular velocity, the equation reduces to a linear relationship between the torque and the velocity as

$$T_e = B_m \omega_m + J_0 = \frac{3}{2} p \lambda_{mpm} i_q.$$

Calculating the generated torque at different mechanical speeds using the  $q$ -axis current and the PM flux linkage, a linear fit can be made to find the values for  $B_m$  and  $J_0$ .

When the viscous friction coefficient and the Coulomb friction has been determined, the inertia of the setup can be calculated for a step change in the torque when the mechanical speed is measured. One way to do this is to run the machine at a fixed speed and then control the  $q$ -axis current to go to zero. Since the controlled current is much faster than the speed it is assumed that the current response will result in a change from a given value of  $T_e$  to zero in a way that has a good approximation to a step response. From this step, the inertia can be found by measuring the deceleration of the machine from a given steady

state speed to zero. Two ways will be used and compared for calculating the inertia of the system.

The first approach will be to assume zero Coulomb friction and an exponential behaviour of the deceleration for the speed response. Using this, the inertia of the setup can be calculated using the viscous friction coefficient and the time constant of the response from the equation

$$\omega_m(t) = \omega_{m,init} e^{-\frac{B_m}{J}t}, \quad (\text{B.2.1})$$

$\omega_{m,init}$  is the initial velocity when the torque is stepped to zero.

The second approach uses mechanical energy conservation. When running at constant speed, the setup has the following rotational energy

$$E_{rot} = \frac{1}{2} J(\omega_m)^2,$$

where  $J$  is the moment of inertia and  $\omega_m$  is the steady state speed before the torque step is applied. During the deceleration, assuming energy conservation, all the rotational energy will be converted to heat through the friction torque

$$T_{fr}(t) = B_m \omega_m(t) + J_0, \quad (\text{B.2.2})$$

where  $B_m$  and  $J_0$  was found as explained previously. The work done by the friction torque is

$$W_{fr} = T_{fr} \cdot \theta = \int_{t_0}^{t_1} T_{fr}(t) \cdot \omega_m(t) dt.$$

The work has to equal the change in rotational energy so

$$W_{fr} = \frac{1}{2} J(\Delta\omega_m)^2$$

which gives that the inertia of the setup is

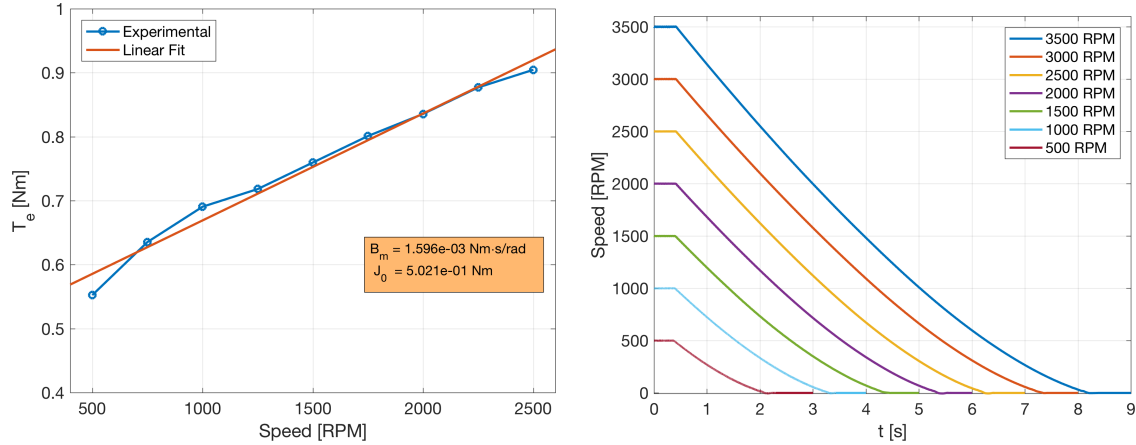
$$J = \frac{2}{(\Delta\omega_m)^2} \int_{t_0}^{t_1} (B_m \omega_m(t) + J_0) \omega_m(t) dt, \quad (\text{B.2.3})$$

where  $t_0$  is the time instant where the torque is stepped and  $t_1$  is the time instant where the mechanical speed reaches zero.

## Execution and Results

The drive machine is driven to a desired steady state speed while the load machine is kept open circuited. For determination of  $B_m$  and  $J_0$ , the torque was calculated at different speeds. This is plotted in figure B.1(a) with a best linear fit for the viscous friction coefficient and the Coulomb friction. As can be seen the core losses does not seem to have any influence on the torque at higher speeds.

To find the inertia of the setup, the torque can be forced to zero in two different ways. Either the inverter can be decoupled or the  $q$ -axis current can be controlled to zero in a step. Both methods were tested and showed similar result which indicates that circulating currents in the inverter diodes when the inverter was bypassed did not have a significant impact on the deceleration curve. When the torque is stepped to zero, the mechanical



(a) Electromagnetic torque versus mechanical speed together with a linear regression of the viscous friction coefficient and the Coulomb friction.

(b) The deceleration curve of the setup at different initial steady state speeds.

Figure B.1: Measurements used to determine  $B_m$ ,  $J_0$  and  $J$ .

speed is measured as a function of time using an encoder interfaced with ControlDesk. This was done for different initial speeds as can be seen in figure B.1(b). As can be seen, the curve does not resemble a perfect exponential decay and therefore using the time constant approach to calculate the inertia will introduce errors as will be discussed shortly.

The setup inertia is then calculated for each case using equation B.2.3 and the method using the mechanical time constant assuming exponential behaviour using equation B.2.1. The mean value of the inertias is then used as the constant value for the system inertia throughout the project. These are represented in table B.2.

#### Comparison of methods to calculate the inertia

Speed [RPM]	Energy Conservation [ $\text{kg}\cdot\text{m}^2$ ]	Exponential Approximation [ $\text{kg}\cdot\text{m}^2$ ]
500	$15.86 \cdot 10^{-3}$	$1.46 \cdot 10^{-3}$
1000	$14.38 \cdot 10^{-3}$	$2.42 \cdot 10^{-3}$
1500	$14.11 \cdot 10^{-3}$	$3.26 \cdot 10^{-3}$
2000	$14.20 \cdot 10^{-3}$	$4.01 \cdot 10^{-3}$
2500	$14.49 \cdot 10^{-3}$	$4.82 \cdot 10^{-3}$
3000	$15.23 \cdot 10^{-3}$	$5.69 \cdot 10^{-3}$
3500	$15.49 \cdot 10^{-3}$	$6.36 \cdot 10^{-3}$
Mean:	$14.82 \cdot 10^{-3}$	$4.00 \cdot 10^{-3}$

Table B.2: Inertia values calculated by the energy conservation method and the exponential decay approximation.

As seen from table B.2, the mean value of the inertia is quite different using the two methods, which is due to the inclusion of the Coulomb friction for the energy conservation method. To further validate which of the two methods to use, a simulation is performed and the deceleration curves are compared. In figure B.2(a), a schematic of the model used in the simulation is shown. The clutch and step is used to generate the time shift until

the load step is given. The inertia is given an initial velocity of 2500 RPM which is not decreasing in the beginning since no friction is present.

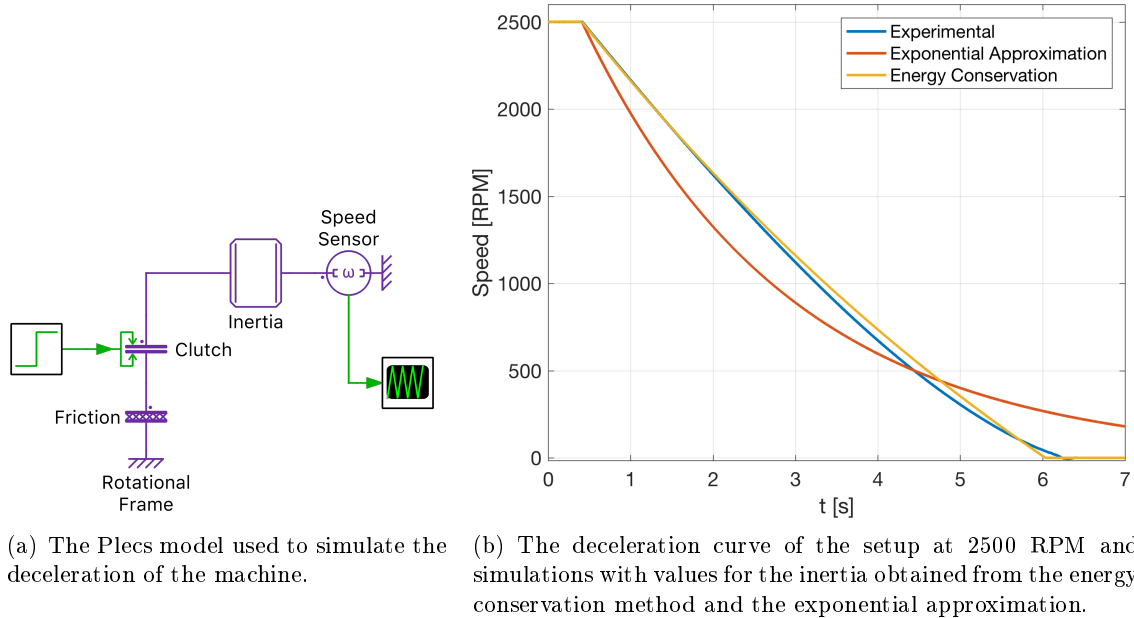


Figure B.2: Simulation of mechanical system used to verify the obtained inertia. The friction is modelled as equation B.2.2 with both  $B_m$  and  $J_0$  for the energy conservation method, whereas  $J_0$  is not included for the exponential approximation.

It can be seen from figure B.2(b) that the inertia calculated from the exponential approximation has similar behaviour as the speed decay seen from the laboratory but has a fundamentally different shape. As mentioned earlier, the deceleration curves do not resemble an exponentially decreasing trend. This together with the fact that the term  $J_0$  is totally left out of the approximation, results in large errors. This supports that the Coulomb friction has to be considered in order to precisely describe the behaviour of the machine. From the figure it is also clear that the energy conservation method gives results which closely resemble the one obtained experimentally. It is however noted that at lower speeds the experimentally obtained results have a slightly higher curvature which could be explained by the lack of Stribeck friction in the model together with other non-linearities.

### B.3 Experimental Determination of Time Delay

When analysing and designing controllers for a system performed on a DSP, the delay of the system has to be known. This delay is used in the plant of the physical system and the system response is sensitive to variations in the time delay. Therefore the determination of the time delay is important. This section has the purpose to experimentally determine the delay from the time the ADC samples the measurements to the time the physical system is able to respond to a change in inverter duty cycle based on that sampled measurements.

Since the dSPACE system only samples data once every switching period, a delay of  $1.5T_s$  will internally in ControlDesk always appear as a delay of two periods since no

information is available between sampling instants. This is the case if the real delay seen by the system is between one and two sampling periods (see figure 3.5(b)). Therefore, to measure the actual time delay from sampling to the time where the continuous system sees the change, an external measuring system is needed. A way to do this is that, while the speed reference is set to zero, a step in the  $d$ -axis current is given. The delay is then the time between the step and the rise of current in the physical setup. To know when the step has occurred a trigger signal is generated when the current reference is higher than 4 A, since the step in current is from 3 A to 5 A. This trigger signal is sent to an output pin, which can be used as a trigger line on an oscilloscope. Besides the trigger line, the  $d$ -axis current is measured using an oscilloscope. This is shown in figure B.3, where it is

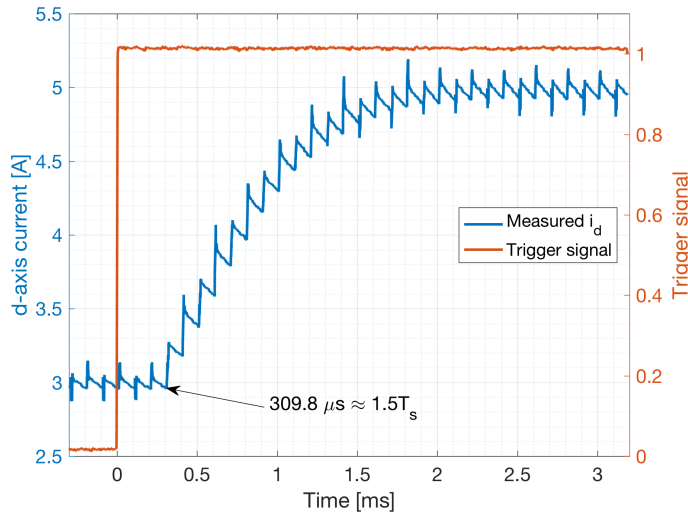
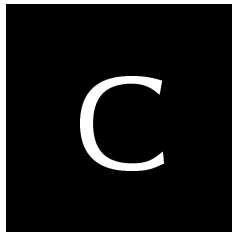


Figure B.3: Measurements of  $i_d$  current and triggering signal which is enabled when the current reference is higher than 4 A. The switching frequency is 5 kHz.

seen that the time delay between the sampling (trigger signal) and the physical response is measured to be 309.8  $\mu$ s, which corresponds to around  $1.5T_s$  since  $f_{sw} = 5$  kHz. As shown in figure 3.5(b), this is also the expected time for the combined sample delay, calculation delay, and PWM delay.

For this experiment it is assumed that the trigger signal is generated at the exact same time where the ADC samples the machine currents. However since the calculation time needed for the algorithm in the DSP is measured to be 8  $\mu$ s, it could generate the trigger signal at any time during this routine. Hence the uncertainty in the result given in figure B.3 is 8  $\mu$ s. So if the trigger signal is generated in the beginning of the calculation routine, the delay will be the measured 309.8  $\mu$ s, whereas for the worst case, if the trigger signal is generated in the end of the calculation routine, the actual delay will be 317.8  $\mu$ s which corresponds to a time delay of approximately  $1.6T_s$ . However approximating the time delay as  $1.5T_s$  is considered acceptable for this project.



# Stability Analysis

Methods for obtaining the roots of a polynomial without solving for the roots are very useful when the coefficients are symbolic. It is then possible to make certain statements about the stability of the system without solving the characteristic equation [43]. In the following sections, methods for determining the stability of both a continuous and discrete system is presented together with a derivation of the stability range in both types of systems.

## C.1 Routh-Hurwitz' Stability Criterion

A well known method to determine if all roots of a continuous polynomial are located in the LHP is the Routh-Hurwitz stability criterion. This is widely used in stability analysis of Linear Time-Invariant systems, for which the characteristic equation is a polynomial on the form

$$a(s) = s^n + a_1 s^{n-1} + a_2 s^{n-2} + \cdots + a_{n-1} s + a_n.$$

A necessary condition for stability, is that all coefficients of the characteristic polynomial are positive. If any coefficient is zero or negative, the system will have poles outside the LHP. This condition can be checked by inspection [21].

In 1874, Routh proposed a method, which gives both necessary and sufficient conditions for stability of a system. Independently Hurwitz did the same in 1895 (hence the name Routh-Hurwitz stability criterion). A system is stable if and only if all elements in the first column of the Routh array (table C.1) are positive.

The Routh Array						
Row	$n$	$s^n:$	1	$a_2$	$a_4$	$\dots$
Row	$n - 1$	$s^{n-1}:$	$a_1$	$a_3$	$a_5$	$\dots$
Row	$n - 2$	$s^{n-2}:$	$b_1$	$b_2$	$b_3$	$\dots$
Row	$n - 3$	$s^{n-3}:$	$c_1$	$c_2$	$c_3$	$\dots$
	:	:	:	:		
Row	2	$s^2:$	$k_1$	$k_2$		
Row	1	$s^1:$	$l_1$			
Row	0	$s^0:$	$m_1$			

Table C.1: A sufficient condition for stability, is that all elements in the first column are positive.

The two first rows of table C.1 are the coefficients of the characteristic polynomial, the first row being the even numbered coefficients and the second row being the odd numbered coefficients. The  $(n - 2)^{th}$  row is constructed as

$$b_1 = -\frac{\begin{vmatrix} 1 & a_2 \\ a_1 & a_3 \end{vmatrix}}{a_1} = \frac{a_1 a_2 - a_3}{a_1}, \quad b_2 = -\frac{\begin{vmatrix} 1 & a_4 \\ a_1 & a_5 \end{vmatrix}}{a_1} = \frac{a_1 a_4 - a_5}{a_1}, \quad b_3 = \frac{a_1 a_6 - a_7}{a_1}$$

and the  $(n - 3)^{th}$  row

$$c_1 = -\frac{\begin{vmatrix} a_1 & a_3 \\ b_1 & b_2 \end{vmatrix}}{b_1} = \frac{b_1 a_3 - a_1 b_2}{b_1}, \quad c_2 = -\frac{\begin{vmatrix} a_1 & a_5 \\ b_1 & b_3 \end{vmatrix}}{b_1} = \frac{b_1 a_5 - a_1 b_3}{b_1}, \quad c_3 = \frac{b_1 a_7 - a_1 b_4}{b_1}.$$

Note that the elements from the  $(n - 2)$ th row and beneath it are formed by taking the determinant of the first element in the two rows above and the elements from the successive column. If not all elements in the first column are positive, the number of Right Half Plane poles equals the number of sign changes [21, 43].

The Routh-Hurwitz stability criterion is tested on the continuous model of the physical system. The model consists of a PI controller, the first order electrical machine model and a second order Padé approximation for the time delay. The block diagram is identical to the block diagram marked with blue in figure 3.11. The characteristic equation is calculated as  $1 + T(s)$  where  $T(s)$  is the open loop gain. This gives

$$\begin{aligned} s^4 + \left( \frac{K_{p,c}}{L} + \frac{R_s}{L} + \frac{6}{T_d} \right) s^3 + \left( \frac{K_{p,c} R_s}{L^2} - \frac{6 K_{p,c}}{L T_d} + \frac{6 R_s}{L T_d} + \frac{12}{T_d^2} \right) s^2 \\ + \left( \frac{12 K_{p,c}}{L T_d^2} - \frac{6 K_{p,c} R_s}{L^2 T_d} + \frac{12 R_s}{L T_d^2} \right) s + \frac{12 K_{p,c} R_s}{L^2 T_d^2} = 0. \end{aligned} \quad (\text{C.1.1})$$

In order to get a simpler characteristic equation  $K_{i,c}/K_{p,c} = R_s/L$ . This is done in equation C.1.1, which places the controller zero to cancel the electrical plant pole. This eliminates  $K_{i,c}$  from the characteristic equation, hence reducing the number of variables by one. The Routh array corresponding to the characteristic equation is shown in table C.2. Here it is noted that the only way which the first column can change sign is if  $b_1$  or  $c_1$  becomes negative. Using the electrical machine parameters and PI parameters obtained for the current controller including time delay ( $K_{p,c} = 8.3$  and  $K_{i,c} = 1770$ ), the critical value for the time delay that will cause the system to be unstable can be calculated. It was found that in order to keep  $b_1$  and  $c_1$  greater than zero at the same time  $T_d < 1.05$  ms. This corresponds to a sampling frequency of approximately 1430 Hz, when  $T_d = 1.5 T_s$ . A simulation was carried out in order to verify the results from this analysis. For the simulation an exact representation of the time delay was used. In figure C.1(a) and C.1(b), the simulation is done when the sampling frequency is 1450 Hz and 1430 Hz respectively. It can clearly be seen that the analysis is able to predict very precisely for which value of the time delay the system will become unstable.

---

**The Routh Array for Equation C.1.1**

---

$$1$$

$$a_2 = \frac{K_{p,c}R_s}{L^2} - \frac{6K_{p,c}}{LT_d} + \frac{6R_s}{LT_d} + \frac{12}{T_d^2} \quad a_4 = \frac{12K_{p,c}R_s}{L^2T_d^2}$$

$$a_1 = \frac{K_{p,c}}{L} + \frac{R_s}{L} + \frac{6}{T_d}$$

$$a_3 = \frac{12K_{p,c}}{LT_d^2} - \frac{6K_{p,c}R_s}{L^2T_d} + \frac{12R_s}{LT_d^2} \quad a_5 = 0$$

$$b_1 = \frac{R_s K_{p,c} (R_s + K_{p,c}) T_d^3 + 6L(-K_{p,c}^2 + 2K_{p,c}R_s + R_s^2) T_d^2 + 36L^2(R_s - K_{p,c}) T_d + 72L^3}{L^2(R_s + K_{p,c}) T_d^3 + 6L^3 T_d^2}$$

$$b_2 = \frac{12K_{p,c}R_s}{L^2T_d^2} \quad b_3 = 0$$

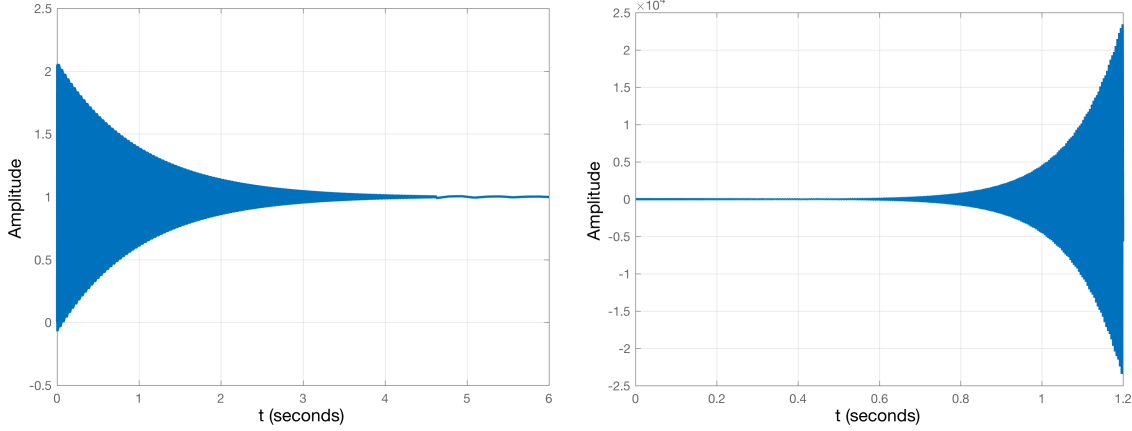
$$c_1 = \frac{12 \left( \frac{R_s^2}{12} (R_s + K_{p,c}) T_d^2 + \frac{LR_s}{2} (R_s - K_{p,c}) T_d + L^2 (R_s + K_{p,c}) \right) \left( \frac{-K_{p,c}T_d^2}{12} - \frac{K_{p,c}LT_d}{2} + L^2 \right)}{L^2 T_d^2 \left( \frac{R_s K_{p,c}}{72} (R_s + K_{p,c}) T_d^3 + \frac{L}{12} (-K_{p,c}^2 + 2K_{p,c}R_s + R_s^2) T_d^2 + \frac{L^2}{2} (R_s - K_{p,c}) T_d + L^3 \right)} \quad c_2 = 0 \quad c_3 = 0$$

$$d_1 = \frac{12K_{p,c}R_s}{L^2T_d^2}$$

$$d_2 = 0 \quad d_3 = 0$$


---

Table C.2: Routh array with electrical machine model, PI controller, and second order Padé approximation for the time delay.



(a) A stable step response when the sampling frequency is 1450 Hz.  
(b) An unstable step response when the sampling frequency is 1430 hz.

Figure C.1: Simulated unit step response of system to verify the analysis done using Routh-Hurwitz. The instability boundary for the sampling frequency was found to be 1430 Hz, which is consistent with simulation.

## C.2 Jury's Stability Criterion

To analyse the stability of a discrete system, Jury's stability criterion can be used, which is equivalent to Routh-Hurwitz' stability criterion used in the continuous domain [43]. Given that the characteristic equation of the closed loop transfer function is

$$F(z) = a_n z^n + a_{n-1} z^{n-1} + \cdots + a_1 z + a_0 = 0,$$

where  $a_n > 0$ , the necessary conditions for stability is that

$$F(1) > 0 \quad \text{and} \quad (-1)^n F(-1) > 0,$$

where  $n$  represent the order of the polynomial. If the necessary condition is met, the sufficient condition is found by forming the Jury array as

Jury's Array						
Row	$z^0$	$z^1$	$z^2$	$\dots$	$z^{n-1}$	$z^n$
1	$a_0$	$a_1$	$a_2$	$\cdots$	$a_{n-1}$	$a_n$
2	$a_n$	$a_{n-1}$	$a_{n-2}$	$\cdots$	$a_1$	$a_0$
3	$b_0$	$b_1$	$b_2$	$\cdots$	$b_{n-1}$	
4	$b_{n-1}$	$b_{n-2}$	$b_{n-3}$	$\cdots$	$b_0$	
5	$c_0$	$c_1$	$c_2$	$\cdots$		
6	$c_{n-2}$	$c_{n-3}$	$c_{n-4}$	$\cdots$		
$\vdots$	$\vdots$	$\vdots$	$\vdots$	$\vdots$		
$2n - 3$	$q_0$	$q_1$	$q_2$			

Table C.3: The Jury array used to analyse the stability of a discrete system.

Note that a total number of rows are  $2n-3$ , giving that for a second order characteristic equation only one row is needed and therefore no coefficients need to be calculated. The coefficients of the odd rows are calculated as determinants of the different indices as follows

$$b_k = \begin{vmatrix} a_0 & a_{n-k} \\ a_n & a_k \end{vmatrix} \quad c_k = \begin{vmatrix} b_0 & b_{n-1-k} \\ b_{n-1} & b_k \end{vmatrix} \quad d_k = \begin{vmatrix} c_0 & c_{n-2-k} \\ c_{n-2} & c_k \end{vmatrix}$$

Notice, that the even ordered rows are simply the reversed order of the odd order rows.

The sufficient conditions are

$$\begin{aligned} |a_0| &< a_n \\ |b_0| &> |b_{n-1}| \\ |c_0| &> |c_{n-2}| \\ &\vdots \quad \vdots \\ |q_0| &> |q_2|, \end{aligned}$$

which gives  $(n - 1)$  sufficient conditions to evaluate. When the coefficients are calculated, the sufficient conditions are checked and a stability conclusion is given [43].

The stability of the discrete system plant proceeded with a ZOH, a unit delay and a PI controller will now be given. In [43] using backwards Euler, it is shown that a PI controller in discrete time can be written as

$$G_c(z) = K_{p,c} + \frac{K_{i,c}zT_s}{z - 1}, \quad (\text{C.2.1})$$

and the characteristic equation using controller, a unit delay and the plant of the current loop, is found from the closed loop transfer function

$$\begin{aligned} G_{cl}(z) &= \frac{G_c(z)G_d(z)G_p(z)}{1 + G_c(z)G_d(z)G_p(z)} \\ &= \frac{K(e^{-aT_s} - 1)(K_{i,c}T_s z + K_{p,c}z - K_{p,c})}{z^3 - (1 + e^{-aT_s})z^2 + \left(\frac{K}{a}(K_{p,c} + K_{i,c}T_s)(1 - e^{-aT_s}) + e^{-aT_s}\right)z - \frac{KK_{p,c}}{a}(1 - e^{-aT_s})} \end{aligned}$$

to be

$$F(z) = z^3 - (1 + e^{-aT_s})z^2 + \left(\frac{K}{a}(K_{p,c} + K_{i,c}T_s)(1 - e^{-aT_s}) + e^{-aT_s}\right)z - \frac{KK_{p,c}}{a}(1 - e^{-aT_s}) = 0,$$

or as  $1 + T(z)$  where  $T(z)$  is the open loop gain. Since this is a third order system three rows are needed in Jury's array, so the  $b$ -coefficients need to be calculated.

$$b_0 = \begin{vmatrix} a_0 & a_3 \\ a_3 & a_0 \end{vmatrix} = \left(\frac{KK_{p,c}}{a}(1 - e^{-aT_s})\right)^2 - 1$$

$$b_1 = \begin{vmatrix} a_0 & a_2 \\ a_3 & a_1 \end{vmatrix} = -\frac{KK_{p,c}}{a}(1 - e^{-aT_s}) \left(\frac{K}{a}(K_{p,c} + K_{i,c}T_s)(1 - e^{-aT_s}) + e^{-aT_s}\right) + (1 + e^{-aT_s})$$

$$b_2 = \begin{vmatrix} a_0 & a_1 \\ a_3 & a_2 \end{vmatrix} = \frac{KK_{p,c}}{a} (1 - e^{-aT_s}) (1 + e^{-aT_s}) - \left( \frac{K}{a} (K_{p,c} + K_{i,c} T_s) (1 - e^{-aT_s}) + e^{-aT_s} \right)$$

The necessary conditions are that

$$\begin{aligned} F(1) &> 0 \\ \Rightarrow 1 - (1 + e^{-aT_s}) + \frac{K}{a} (K_{p,c} + K_{i,c} T_s) (1 - e^{-aT_s}) + e^{-aT_s} - \frac{KK_{p,c}}{a} (1 - e^{-aT_s}) &> 0 \end{aligned}$$

and

$$\begin{aligned} (-1)^3 F(-1) &> 0 \\ \Rightarrow 1 + (1 + e^{-aT_s}) + \frac{K}{a} (K_{p,c} + K_{i,c} T_s) (1 - e^{-aT_s}) + e^{-aT_s} - \frac{KK_{p,c}}{a} (1 - e^{-aT_s}) &> 0, \end{aligned}$$

and the sufficient conditions

$$\begin{aligned} |a_0| < a_n &\Rightarrow \left| -\frac{KK_{p,c}}{a} (1 - e^{-aT_s}) \right| < 1 \\ |b_0| > |b_2| &\Rightarrow \left| \left( \frac{KK_{p,c}}{a} (1 - e^{-aT_s}) \right)^2 - 1 \right| > |b_2|, \end{aligned}$$

where

$$|b_2| = \left| \frac{KK_{p,c}}{a} (1 - e^{-aT_s}) (1 + e^{-aT_s}) - \left( \frac{K}{a} (K_{p,c} + K_{i,c} T_s) (1 - e^{-aT_s}) + e^{-aT_s} \right) \right|$$

Using the physical values for  $K = 1/L$  and  $a = R_s/L$  the stability conditions are

$$\begin{aligned} F(1) > 0 &\Rightarrow 1.47 K_{i,c} T_s (1 - e^{-123.64T_s}) > 0 \\ (-1)^3 F(-1) > 0 &\Rightarrow (10.526 K_{p,c} + 1.47 K_{i,c} T_s) (1 - e^{-123.64T_s}) + 2 (1 + e^{-123.64T_s}) > 0 \end{aligned}$$

which is true for all values of  $T_s$  if the proportional and integral gains are positive. The sufficient condition is

$$|a_0| < a_3 \Rightarrow 1.47 K_{p,c} |1 - e^{-123.64T_s}| < 1.$$

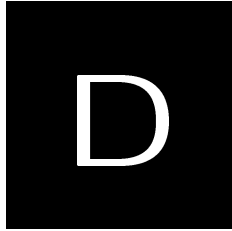
The last sufficient condition is

$$|b_0| > |b_2| \Rightarrow |2.163 K_{p,c}^2 q_1^2 - 1| > \left| 1.47 q_1 K_{p,c} (1 + \frac{K_{i,c} T_s}{K_{p,c}} - q_2) + q_2 - 1 \right|,$$

where

$$q_1 = 1 - e^{-123.64T_s} \quad \text{and} \quad q_2 = 1 + e^{-123.64T_s}.$$

The stability of the sampling time will be further analysed when the discrete time current controller is designed, since it is unpractical to analyse when three independent parameters exist in the equation. This is done in section 3.3.



# Modified Linear Predictor

To improve the LP described in subsection 4.5.2 information about the future voltage to be applied and the reference current will be included, forming the MLP. The block diagram of the control structure can be seen in figure D.1.

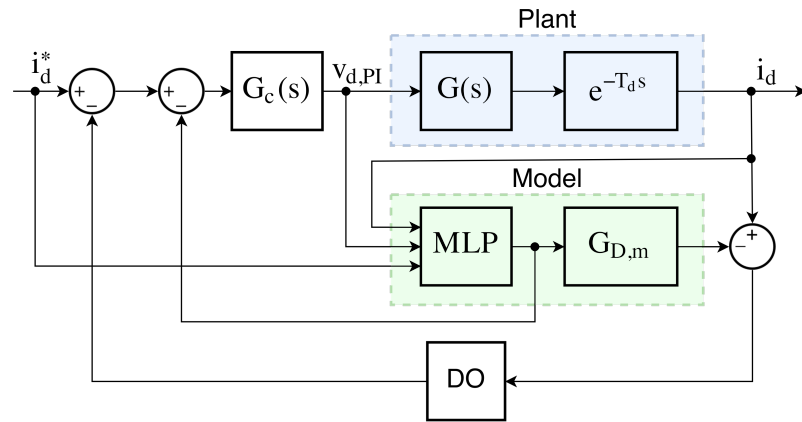


Figure D.1: Block diagram of modified linear predictor, which uses information of present current, reference current and future voltage.

Since the LP described in subsection 4.5.2, does not have any information regarding a sudden change in the reference current or about the future voltage to be applied in the next output state, the LP will inherently be slow, which was shown in figure 4.20(a). Thus, in the MLP, the measured current is scaled dependent on the change in reference current. Furthermore the slope of the predicted current is dependent on the change in the voltage to be applied to the machine in the next output state. This means that if the change in voltage is decreasing from one switching instant to the next, the slope of the predicted current should also decrease. The current is therefore still allowed to increase but the slope is forced to decrease. The implementation of this can be seen in the code shown in listing D.1.

The code has identical structure for the  $q$ -axis current. The constants  $k_1$  and  $k_2$  were found iteratively to get best performance.

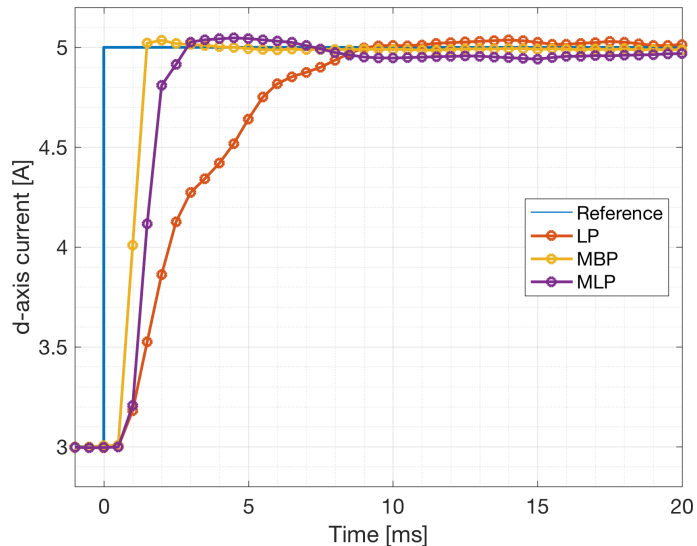
A step response in  $d$ -axis current was performed in the laboratory with this MLP. This is shown in figure D.2, where it can be seen that including information about the voltage to be applied and the reference current, the current response can be made much faster and is almost as fast as the MBP. However a stability test was performed using the MLP, and the controller was already unstable before 1000 RPM, hence the results are not included here. For the MLP including information about the reference current and the output voltage of the PI controller resulted in a faster response of the current. However the stability of the system was decreased compared to FOC. Therefore another control strategy improving the stability was attempted. This strategy is described in subsection 4.5.3.

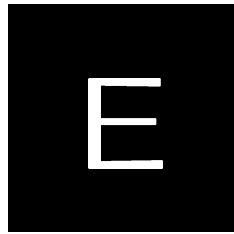
Listing D.1: MATLAB code for MLP shown for *d*-axis current.

```

1 %% Modified Linear Predictor
2
3 % Gains
4 k1 = 0.2; % Gain to adjust measured current
5 k2 = 0.5; % Gain to limit slope of current
6
7
8 % Adjust measured current depending on change in reference
9 if abs(Id_ref-Id_ref_old)>0.5
10 id_meas = id_meas*k1;
11 end
12
13 % Calculates present and old value for change in applied voltage
14 V_change_now = Vd-Vd_old; % Change in new voltage
15 V_change_old = Vd_old-Vd_old2; % Change in old voltage
16
17 % Limit slope of current depending on present voltage
18 if V_change_now<V_change_old
19 Slope_d = Slope_d_old*k2;
20 else
21 Slope_d = (id_meas-id_old)/Ts; % Calculates slope of d-axis current
22 end
23
24 % Calculate predicted current
25 id_new = id_meas + Slope_d*Ts; % New current prediction based on calculated slope.
26
27 % Store relevant parameters to next sampling instant
28 id_old = id_meas;
29 Id_ref_old = Id_ref;
30 Vd_old2 = Vd_old;
31 Vd_old = Vd;
32 Slope_d_old = Slope_d;

```

Figure D.2: Experimental response of step in *d*-axis current when using LP, MLP and MBP for predicting the currents in the SP.



# PI Parameters

<b>Figure</b>	<b>Controller</b>	<b>Line</b>	$K_p$	$K_i$
3.4(a)	Current	Blue	20.14	4121
		Red	20.14	4121
3.4(b)	Speed	Blue	0.846	7.859
		Red	0.846	7.859
3.10(a)	Current	Blue	6.026	650.81
3.10(b)	Current	Blue	8.3	1770
3.12	Speed	Blue	3.8	0.41
3.13	Current	Blue	7.967	1664
3.14	Speed	Blue	3.8	0.41
3.15	Current	Blue	7.967	1664
3.19(a)	Current	Red	7.967	1664
3.19(b)	Speed	Red	0.007	0.004
3.20(a)	Current	Yellow	7.1	1250
3.21	Speed	Yellow	0.07	0.05
3.23(a)	Current	All	7.1	1250
4.4	Current	Red	2	380
		Yellow	3.5	900
		Purple	7.8	1700
		Green	11	2500
4.14	Current	All	8	1700
4.20(a)	Current	Red	11	2500
		Yellow	2.2	590
		Purple	2	380
4.20(b)	Current	Yellow	2.2	590
C.1	Current	Blue	8.3	1770

Table E.1: PI parameters of controllers used in simulation.

<b>Figure</b>	<b>Controller</b>	<b>Line</b>	$K_p$	$K_i$
3.20(a)	Current	Red	7.1	1250
3.20(b)	Speed	Red	0.007	0.004
3.21	Speed	Red	0.07	0.05
3.23(b)	Current	All	7.1	1250
4.6	Current	Red	2	370
		Yellow	6.5	1200
		Purple	11	3400
4.10	Speed	All	0.07	0.8
	Current	All	2	370
4.11	Speed	All	0.07	0.8
	Current	All	2	370
4.12	Speed	All	0.07	0.8
	Current	All	11	3400
4.13	Speed	All	0.07	0.8
	Current	All	11	3400
4.17(a)	Current	Black	1	10
		Red	11	3400
4.17(b)	Current	All	11	3400
4.18	Current	All	11	3400
4.20(b)	Current	Red	2.3	550
4.21(a)	Current	Red	11	3400
4.23(a)	Current	Red	0.9	110
4.23(b)	Current	Red	7	1400
D.2	Current	Red	2	430
		Yellow	11	3400
		Purple	2.2	730

Table E.2: PI parameters of controllers used in the laboratory test.

# Bibliography

---

- [1] G. Lei, C. Liu, and B. Ma, "Robust Design Optimization of Electrical Machines and Drive Systems for High Quality Mass Production," *Electrical Drives Production Conference*, Nov 2016.
- [2] S. J. Chapman, *Electric Machinery Fundamentals*, 4th ed. Mc Graw Hill, 2005, ISBN: 0-07-246523-9.
- [3] M. B. B. Sharifian, T. Herizchi, and K. G. Firouzjh, "Field Oriented Control of Permanent Magnet Synchronous Motor Using Predictive Space Vector Modulation," *ISIEA*, Oct 2009.
- [4] C. Garcia, C. Silva, J. Rodriguez, and P. Zanchetta, "Cascaded Model Predictive Speed Control of a Permanent Magnet Synchronous Machine," *Industrial Electronics Society , IECON 2016 - 42nd Annual Conference of the IEEE*, Oct 2016.
- [5] E. Prasad, B. Suresh, and K. Raghubeer, "Field Oriented Contorl of PMSM Using SVPWM Technique," *Global Journal of Advanced Engineering Technologies*, vol. 1, no. 2, 2012.
- [6] M. Kim, J.-S. Yim, S.-K. Sul, and S.-I. Lim, "Implementation of Super High-speed Permanent Magnet Synchronous Machine Drive," *Energy Conversion Congress and Exposition*, Sep 2009.
- [7] E. Yesilbag and L. T. Ergene, "Field Oriented Control of Permanent Magnet Synchronous Motors used in Washers," *International Power Electronics and Motion Control Conference and Exposition*, Sep 2014.
- [8] X. Zhang, B. Hou, and Y. Mei, "Deadbeat Predictive Current Control of Permanent-Magnet Synchronous Motors with Stator Current and Disturbance Observer," *IEEE Transactions on Power Electronics*, vol. 32, no. 5, May 2017.
- [9] E. Prasad, B. Suresh, and K. Raghubeer, "Adaptive Self-Tuning Speed Control for Permanent-Magnet Synchronous Motor Drive with Dead Time," *IEEE Transactions on Energy Conversion*, vol. 21, no. 4, 2006.
- [10] B.-H. Bae and S.-K. Sul, "A Compensation Method for Time Delay of Full-Digital Synchronous Frame Current Regulator of PWM AC Drives," *IEEE Transactions on Industry Applications*, vol. 39, no. 3, 2003.
- [11] M. Benouarets and D. P. Athweton, "Autotuning Design Methods for a Smith Predictor Control Scheme," *International Conference on Control*, Mar 1994.
- [12] A. Maddi, A. Guessoum, and D. Berkani, "Design of Nonlinear PID-Smith Predictor Controllers with Large Time Delays," *Complex Systems*, Nov 2016.

- [13] I. Takahashi, T. Koganezawa, G. Su, and K. Ohyama, "A Super High Speed PM Motor Drive System by a Quasi-Current Source Inverter," *IEEE Transactions on Industry Applications*, vol. 30, no. 3, Jun 1994.
- [14] P. Niedermayr, S. Bolognani, L. Alberti, and R. Abl, "Sensorless control of a super-high speed synchronous motor drive based on a Kalman filter," *Industrial Electronics Society*, 2016.
- [15] G. Han, Y. Xia, and W. Min, "Study on the Three-phase PV Grid-connected Inverter Based on Deadbeat Control," *Power Engineering and Automation Conference (PEAM)*, Sep 2012.
- [16] Y. Abdel-Rady, I. Mohammed, and E. F. El-Saadany, "Adaptive Discrete-Time Grid-Voltage Sensorless Interfacing Scheme for Grid-Connected DG-Inverters Based on Neutral-Network Identification and Deadbeat Current Regulation," *IEEE Transaction on Power Electronics*, vol. 23, no. 1, pp. 308–321, Jan 2008.
- [17] X. Zhang, B. Hou, and Y. Mei, "Deadbeat Predictive Current Control of Permanent-Magnet Synchronous Motors with Stator Current and Disturbance Observer," *IEEE Transaction on Power Electronics*, vol. 32, no. 5, pp. 3818–3834, May 2017.
- [18] O. Abdel-Rahim and H. Funato, "A Novel Predictive Control for High Gain Switched Inductor Power Conditioning System for Photovoltaic Applications," *Innovative Smart Grid Technologies - Asia (ISGT Asia)*, May 2014.
- [19] T. John, Y. Wang, K. T. Tan, and P. L. So, "Model Predictive Control of Distributed Generation Inverter in a Microgrid," *Innovative Smart Grid Technologies - Asia (ISGT Asia)*, May 2014.
- [20] O. J. M. Smith, "Posicast Control of Damped Oscillatory Systems," *Proceedings of the IRE*, vol. 45, no. 9, pp. 1249–1255, Sep 1957.
- [21] G. F. Franklin, J. D. Powell, and A. E. Naeini, *Feedback Control of Dynamic Systems*, 7th ed. Pearson, 2015, ISBN: 978-1-29-206890-9.
- [22] A. Ingimundarson, "Robust tuning procedures of dead-time compensating controllers," Master's thesis, Lund Institute of Technology, Dec 2000.
- [23] Z. Chun, M. Qishuang, C. Tongkai, and Z. Poming, "Model-Predictive Current Control of DC/AC Inverter with Time Delay Compensation," *IEEE International Conference on Aircraft Utility Systems (AUS)*, Oct 2016.
- [24] G. Liu, J. Yuan, W. Zhao, and Y. Mi, "New Smith Internal Model Control of Two-Motor Drive System Based on Neural Network Generalized Inverse," *Journal of Control Science and Engineering*, Jan 2016.
- [25] I. Kaya, "IMC Based Automatic Tuning Method For PID Controllers in a Smith Predictor Configuration," *Computer and Chemical Engineering*, vol. 28, pp. 281–290, Jan 2003.

- [26] A. O'Dwyer, "A Reference Guide to Smith Predictor Based Methods for the Compensation of Dead-Time Precesses," *Proceedings of the IEE Irish Signals and Systems Conference*, pp. 231–238, Sep 2005.
- [27] A. O'Dwyer and J. Ringwood, "The Control of a Process with Time Delay by Using a Modified Smith Predictor Compensator," *Proceedings of the Irish Conference on DSP and Control*, pp. 37–44, Jun 1996.
- [28] V. Massimiliano, "Performance Improvement of Smith Predictor Through Automatic Computation of Dead Time," Industrial Automation Department Yokogawa Italia, Tech. Rep., Apr 2003.
- [29] S. Bibian and H. Jin, "Time Delay Compensation of Digital Control for DC Switchmode Power Supplies Using Predictive Techniques," *IEEE Transaction on Power Electronics*, vol. 15, no. 5, pp. 835–842, Sep 2000.
- [30] P. C. Krause, O. Wasynczuk, and S. D. Sudhoff, *Analysis of Electric Machinery and Drive Systems*, 2nd ed. Wiley Interscience, 2002, ISBN: 0-471-14326-X.
- [31] A. Apte, R. Walambe, V. Joshi, K. Rathod, and J. Kolhe, "Simulation of a Permanent Magnet Synchrounous Motor using Matlab-Simulink," *India Conference (INDICON)*, Dec 2014.
- [32] Microsemi, "Field Oriented Control of Permanent Magnet Synchronous Motors," 2012.
- [33] P. Vas, *Sensorless Vector and Direct Torque Control*, 1st ed. Oxford Science Publications, 1998, ISBN: 0-19-856465-1.
- [34] P. Brandstetter and T. Krecek, "Speed and Current Control fo Permanent Magnet Synchronous Motor Drive Using IMC Controllers," *Advances in Electrical and Computer Engineering*, vol. 12, no. 4, 2012.
- [35] R. Krishnan, *Permanent Magnet Synchronous and Brushless DC Motor Drives*, 1st ed. CRC Press, 2010, ISBN: 978-0-8247-5384-9.
- [36] A. B. Nielsen and M. T. Thomé, "Compensatio of Time Delays Caused by Digital Control of PWM Inverter with Predictive Control Techniques," *Conference for Energy Students at AAU*, Dec 2016.
- [37] B. Wu, *High-Power Converters and AC Drives*, 1st ed. Wiley Interscience, 2006, ISBN: 0-471-73171-4.
- [38] F. Lattarulo, *Electromagnetic Compatibility in Power Systems*. Elsevier Science, 2011.
- [39] M. Vajta, "Some Remarks on Padé-Approximations," *3rd TEMPUS-INTERCOM Symposium*, 2000.
- [40] G. F. Franklin, J. D. Powell, and M. Workman, *Digital Control of Dynamic Systems*, 3rd ed. Addison Wesley Longman Inc., 1998, ISBN: 0-201-82054-4.
- [41] T. P. Wang and T. D. Chiueh, "A Low-Complexity Fractional Delay All-Pass Filter Design for Time-Domain Interpolation," *VLSI Design, Automation and Test*, 2007.

- [42] V. Välimäki, "Simple Design of Fractional Delay Alpass Filters," *EUSIPCO*, 2000.
- [43] C. L. Phillips and J. M. Parr, *Feedback Control Systems*, 5th ed. Pearson, 2011, ISBN: 0-13-186614-1.
- [44] X. I. Li, J. G. Park, and H. B. Shin, "Comparison and Evaluation of Anti-Windup PI Controllers," *Journal of Power Electronics*, Jan 2011.
- [45] J. E. Marshall, *Control of Time-Delay Systems*, 1st ed., ser. IEE Control Engineering Series 10. Peter Peregrinus Ltd., 1979, ISBN: 0-906048-12-5.
- [46] Q. Liu and K. Hameyer, "A fast online full parameter estimation of a PMSM with sinusoidal signal injection," *Energy Conversion Congress and Exposition*, Sep 2015.
- [47] Z.-H. Liu, H.-L. Wei, Q.-C. Zhong, K. Liu, X.-S. Xiao, and L.-H. Wu, "Parameter Estimation for VSI-Fed PMSM Based on a Dynamic PSO with Learning Strategies," *IEEE Transactions on Power Electronics*, vol. 32, no. 4, Apr 2017.
- [48] J. Moos, "Predictive Deadbeat Control For PMSM Drive," Master's thesis, Faculties of Engineering and Science at Aalborg University, 2014.
- [49] W. F. Zhang and Y. H. Yu, "Comparison of Three SVPWM Strategies," *Journal of Electronic Science and Technology of China*, vol. 5, no. 3, Sep 2007.
- [50] T. Sutikno, A. Jidin, and M. F. Bassar, "Simple Realization of 5-Segment Discontinuous SVPWM Based on FPGA," *International Journal of Computer and Electrical Engineering*, vol. 2, no. 1, Feb 2010.
- [51] M. Zelechowski, "Space Vector Modulated - Direct Torque Controlled (DTC - SVM) Inverter - Fed Induction Motor Drive," Ph.D. dissertation, Faculty of Electrical Engineering - Institute of Control and Industrial Electronics, 2005.
- [52] A. Saadoun, A. Yousfi, and Y. Amirat, "Modeling and Simulation of DSP Controlled SV PWM Three Phase VSI," *Journal of Applied Science*, vol. 7, pp. 989–994, 2007.
- [53] N. P. Quang and J. A. Dittrich, *Vector Control of Three-Phase AC Machines*, 2nd ed. Springer, 2015, ISBN: 987-3-662-46915-6.
- [54] M. Bendjedia, Y. Ait-Amirat, B. Walther, and A. Berthon, "DSP Implementation of Field Oriented control of Hybrid Stepper Motor," *Second International Conference on Electrical Systems ICES*, May 2006.
- [55] dSPACE, "Ds1103 ppc controller board," Online datasheet, 2008.